The Pennsylvania State University

The Graduate School

College of Engineering

COMPREHENSIVE MODEL AND EXPERIMENTAL VALIDATION OF PASSIVE VIBRATION SUPPRESSION FOR SUPERCRITICAL ROTARY MACHINES

A Thesis in

Aerospace Engineering

by

Ahmad M. Haidar

Submitted in Partial Fulfillment

of the Requirements

for the Degree of

Master of Science

December 2015

The thesis of Ahmad M. Haidar was reviewed and approved* by the following:

Jose L. Palacios

Assistant Professor of Aerospace Engineering

Thesis Advisor

Edward C. Smith

Professor of Aerospace Engineering

George A. Lesieutre

Professor of Aerospace Engineering

Head of the Department of Aerospace Engineering

*Signatures are on file in the Graduate School.

Abstract

A comprehensive physics-based model of a rotary system was formulated and experimentally validated to predict the performance and dynamic behavior of passive balancing devices. The mathematical model incorporates three-dimensional effects such as non-planar rotor bending and places little restriction on the system configuration. Special attention was placed on balancing mass interaction with other balancing masses and with the balancer track. The effects of balancing mass collisions and friction were modeled and tested.

Passive balancing devices for rotary systems consist of masses that are free to move in concentric guides about the shaft axis. Under optimal conditions, notably at supercritical speeds, the balancing masses automatically assume new positions to counter any imbalance due to uneven mass distribution in the system. The balancing phenomenon occurs as a result of a 180 degree shift in the system response phase with respect to the imbalance phase when a natural frequency is traversed. Eccentric centrifugal loads on the balancing masses cause them to move in a manner that suppresses or diminishes rotor vibration. The problem is highly nonlinear and requires comprehensive modeling to achieve satisfactory prediction of the balancing behavior.

In this research, a test rig was fabricated to experimentally validate the presented mathematical model. A rotating shaft with an imbalanced hub and a passive balancing device was tested at 1600 RPM, a supercritical speed. The passive balancer performance in transient and steady states was investigated under various imbalanced configurations. In the experiment, the passive balancing device on average reduced shaft vibrations by 62% at steady state. In addition, the experiment demonstrated that the passive balancer exhibits suboptimal performance when the system had low imbalance. This is opposite to what is predicted by conventional models in which viscous damping is the sole interaction between the balancing masses and the balancer track.

Models available in the literature predicted the results within 68% of the experimental values. The comprehensive balancing model developed in this thesis more accurately predicts the performance of the passive balancer. The increased accuracy was accomplished through the inclusion of rolling resistance friction between the balancing masses and the balancer track, as well as the inelastic collisions between the balancing masses. By incorporating inelastic collisions, the accuracy of the predictions was improved by a factor of 6.7 (3.7% margin of error vs. 24.7%) in high imbalance scenarios. By including friction, the model prediction accuracy was increased by a factor of 3.3 (17.6% vs. 58.1%). Overall, the model presented in this thesis improved the accuracy by a factor of 3.9 when compared to published models (17.6% vs. 67.7%). Ignoring the effects of friction and mass collisions reduces accuracy of predictions significantly. The model which addresses friction and collisions was validated and predicted the performance of the passive balancer to within 17.6% of the experimental values in all tested cases.

Table of Contents

List of Figures

List of Tables

List of Symbols

$\mathbf{a}$	Rotating frame that follows shaft rigid-body rotation
$\mathbf{a_i}$	Blade-fixed frame located at root of each blade
$\mathbf{b}$	Rotating frame that follows shaft deformed rotating shape
$\mathbf{C}$	System damping matrix
$\mathbf{F}$	System load vector
$\mathbf{F}_g$	Gravitational body force, N
$\mathbf{K}$	System stiffness matrix
$\mathbf{M}$	System mass matrix
$\mathbf{Q}$	Generalized force vector, *varies*
$\mathbf{q}$	Generalized coordinate vector, *varies*
$\mathbf{q_{AB}}$	Balancer generalized coordinate vector, *rad*
$\mathbf{q_{blade}}$	Blade generalized coordinate vector, m
$\mathbf{q_{shaft}}$	Shaft generalized coordinate vector, *varies*
$\mathbf{R}_{OB_i}$	Position vector locating balancing mass, m
$\mathbf{R}_{OC}$	Position vector locating hub center, m
$\mathbf{R}_{OI_i}$	Position vector locating blade-fixed mass center of gravity, m

$\mathbf{R}_{OM}$	Position vector locating introduced imbalance mass, m
$\mathbf{R}_{OP_i}$	Position vector locating point P on i^{th} blade, m
$\mathbf{T_{ab}}$	Transformation matrix from frame **a** to **b**
$\mathbf{T_{nb}}$	Transformation matrix from frame **n** to **b**
$\mathbf{T_{ba_i}}$	Transformation matrix from frame **b** to $\mathbf{a_i}$
$\mathbf{T_{na}}$	Transformation matrix from frame **n** to **a**
$\mathbf{T_{xn}}$	Transformation matrix from frame $\mathbf{x}_g$ to **n**
$\mathbf{x}_g$	Earth fixed frame
b_i	ith blade chord length, m
c	Bearing damping coefficient, kg/s
c_{AB}	Balancer/shaft viscous damping coefficient, kg/s
C_d	Nondimensional blade drag coefficient
c_d	Blade drag coefficient per unit length, kg/m^2
C_n	Constant number
C_R	Coefficient of restitution
D	Total system Rayleigh damping energy, N-m
D_{AB}	Balacer Rayleigh dissipation function, N-m
$D_{bearing}$	Bearing Rayleigh dissipation function, N-m
D_{blade}	Blade Rayleigh dissipation function, N-m
D_{shaft}	Shaft Rayleigh dissipation function, N-m
E	Beam modulus of elasticity, N/m^2
E_{blade}	Blade modulus of elasticity, N/m^2
E_{shaft}	Shaft modulus of elasticity, N/m^2
F_f	Rolling friction force between balancing mass and track surfaces, N

F_N	Normal force with respect to balancing mass/track surface, N
G	Rod modulus of rigidity, N/m^2
g	Earth gravitation constant, N
G_{shaft}	Shaft modulus of rigidity, shear modulus, N/m^2
h	Rotation angle about $\mathbf{n}_1$ axis with respect to $\mathbf{x}$ frame, rad
I	Beam second area moment of inertia, m^4
i	Integer index
$I_{blade,1}$	Blade second area moment of inertia about $\mathbf{a}_{1i}$, m^4
$I_{blade,3}$	Blade second area moment of inertia about $\mathbf{a}_{3i}$, m^4
$I_{m_{hub}}$	Hub transverse moment of inertia, kg-m^2
$I_{m_{shaft}}$	Shaft transverse moment of inertia, kg-m^2
I_{shaft}	Shaft second area moment of inertia, m^4
J	Rod polar moment of area, m^4
$J_{m_{hub}}$	Hub polar moment of inertia, kg-m^2
$J_{m_{shaft}}$	Shaft polar moment of inertia, kg-m^2
J_{shaft}	Shaft polar moment of area, m^4
k	Bearing stiffness coefficient, N/m
L	Beam or rod length, m
L_i	Blade length, m
L_{bmass}	Location of balancer system along shaft length, m
$L_{bearing_i}$	Location(s) of ith bearing support along shaft length, m
L_{hub}	Location of hub along shaft length, m
L_{imb}	Location of imbalance mass along shaft, m
L_{shaft}	Shaft length, m

m_{bmass}	Mass of one balancing mass, kg
m_{blade_i}	Mass of ith blade per unit length, kg/m
m_{bm}	Mass of imbalance mass attached to blade, kg
m_{hub}	Mass of hub without blades, kg
m_{shaft}	Mass of shaft, kg
m_{imb}	Introduced imbalance mass, kg
N	Number of degrees of freedom
N_b	Number of blades on hub
N_m	Number of assumed modes for the shaft
$N_{m,b}$	Number of assumed modes for the blade
N_{AB}	Number of balancer systems
N_{bal}	Number of balancer masses per balancer
p	Rotation angle about $\mathbf{x}_g 3$ axis with respect to $\mathbf{x}$ frame, rad
R_b	Balancer track radius, m
R_{hub}	Hub radius, m
R_{imb}	Distance of imbalance mass from the shaft center, m
R_{shaft}	Shaft radius, m
r	Rotation angle about $\mathbf{n}_2$ axis with respect to $\mathbf{x}$ frame, rad
r_b	Balancing mass radius, m
T	Total system kinetic energy, N-m
t	Time, s
t_i	ith blade thickness, m
T_{AB}	Balancer kinetic energy, N-m
$T_{bearing}$	Damper kinetic energy, N-m

T_{bend} Beam bending kinetic energy, N-m

T_{blade} Blade kinetic energy, N-m

T_{bm} Blade-fixed mass kinetic energy, N-m

T_{hub} Hub kinetic energy, N-m

t_{hub} Hub thickness, m

T_{imb} Imbalance mass kinetic energy, N-m

T_{shaft} Shaft kinetic energy, N-m

$T_{torsion}$ Rod torsional kinetic energy, N-m

U Total system potential energy, N-m

U_{AB} Balancer potential energy, N-m

$U_{bearing}$ Bearing potential energy, N-m

U_{bend} Beam bending strain energy, N-m

u_{blade_i} Local blade displacement in the normal direction, m

U_{blade} Blade potential energy, N-m

U_{bm} Blade-fixed mass potential energy, N-m

U_{hub} Hub potential energy, N-m

U_{imb} Imbalance mass potential energy, N-m

U_{shaft} Shaft potential energy, N-m

$U_{torsion}$ Rod torsional strain energy, N-m

v Transverse deflection of shaft neutral axis in $\mathbf{a}_2$ direction, m

v_i Transverse deflection of i^{th} blade neutral axis in $\mathbf{a}_{1i}$ direction, m

v_{blade_i} Velocity component of local blade in the normal direction, m/s

W Total system work energy, N-m

w Transverse deflection of shaft neutral axis in $\mathbf{a}_3$ direction, m

w_i	Transverse deflection of i^{th} blade neutral axis in $\mathbf{a}_{3i}$ direction, m
W_{NC}	System non-conservative work, N-m
x	Shaft-fixed length coordinate, m
x_i	Blade-fixed length coordinate, m
Y	Beam bending assumed mode shape
y	Beam deflection due to bending, m
β	Rotation angle about $\mathbf{b}_2$ axis with respect to $\mathbf{a}$ frame, rad
δW_{AB}	Balancer virtual work, N-m
δW_{blade}	Blade virtual work, N-m
η_{ϕ_i}	Modal coordinate vector for $\hat{\phi}$ displacement, rad
η_{v_i}	Modal coordinate vector for v displacement, m
η_{v_ij}	Modal coordinate vector for v_i displacement, m
η_{w_i}	Modal coordinate vector for w displacement, m
η_{w_ij}	Modal coordinate vector for w_i displacement, m
γ	Rotation angle about $\mathbf{b}_3$ axis with respect to $\mathbf{a}$ frame, rad
κ	Rod torsion parameter
μ	Mass per unit length, kg/m
μ_r	Rolling friction coefficient
$\mu_{r,l}$	Rolling friction coefficient with dimension length, m
Ω	System rotation speed, rad/s
ω	Natural frequency, rad/s
ω_B	Rotation velocity of $\mathbf{b}$ frame with respect to $\mathbf{n}$ frame, rad/s
$\hat{\phi}$	Shaft rotation, rad
Φ	Rod torsional assumed mode shape

ϕ	Total shaft rotation about $\mathbf{n}_1$, rad
Φ_i	Torsional cantilever rod mode shapes
ϕ_{b_i}	Balancing mass location, rad
ϕ_m	Phase of the imbalance mass, rad
ψ_i	Blade azimuth angle, rad
Ψ_{ij}	Euler-Bernoulli cantilever beam bending mode shapes
ρ_{air}	Air density, kg/m^3
σ	Beam bending parameter
Θ_i	Euler-Bernoulli fixed-fixed beam bending mode shapes
ξ_{blade}	Blade material damping coefficient, s
ξ_{shaft}	Shaft structural damping, s
ζ	Critical damping ratio
$\mathcal{L}$	System Lagrangian, N-m

Acknowledgments

I would like to sincerely thank my advisor and mentor, Dr. Jose Palacios, for his time and commitment to my research. Without his guidance and expertise, my research would have not been possible. Dr. Palacios's advice was invaluable at every stage of my work and graduate career. I would also like to thank Dr. Edward Smith and Dr. George Lesieutre for taking the time to review my thesis and provide expert feedback.

I would like to show my gratitude to my fellow graduate students, Matt Drury, Miguel Alvarez, Edward Rocco, Jared Soltis, Yiqiang Han, Sihong Yan and Belen Veras-Alba. The time, recommendations and supportive environment they provide are deeply appreciated.

I owe a great deal of gratitude to my family for their endless support and encouragement throughout my educational career. I would especially like to thank my parents for their hard work that allowed me to pursue my dreams.

Chapter 1

Introduction

1.1 Background and Motivation

Rotary machinery is a foundational component of industrial and military technology used today. It is used in a wide array of applications ranging from products designed for the home, such as washing machines and optical media drives, to cutting edge technology, such as wind turbine generators. Numerous other uses are also notable such as rotary machinery used in electric motors, power tools, household appliances, internal combustion engines, turbine engines, steam turbines, electric generators, industrial compressors, power transmission systems, rotor and propeller hubs, centrifuges, and many more.

This form of machinery is clearly extremely relevant due to its extensive presence across industry. It is crucial that improvements in performance are thoroughly studied. This thesis focuses on improving the performance of supercritical rotary machines by providing an improved model of passive vibration suppression along with experimental validation for a flexible rotating system.

In general terminology, a rotating machine consists of a shaft, a rotor and a stator (Figure 1.1). The shaft is the component that translates rotary motion to the rotor. The rotor is usually fixed to the shaft and rotates at the same angular rate as the shaft. The stator is the stationary component of the machine. The terms may change across industry but the concept remains the same. In some domains, the rotor is referred to as the hub or disk.

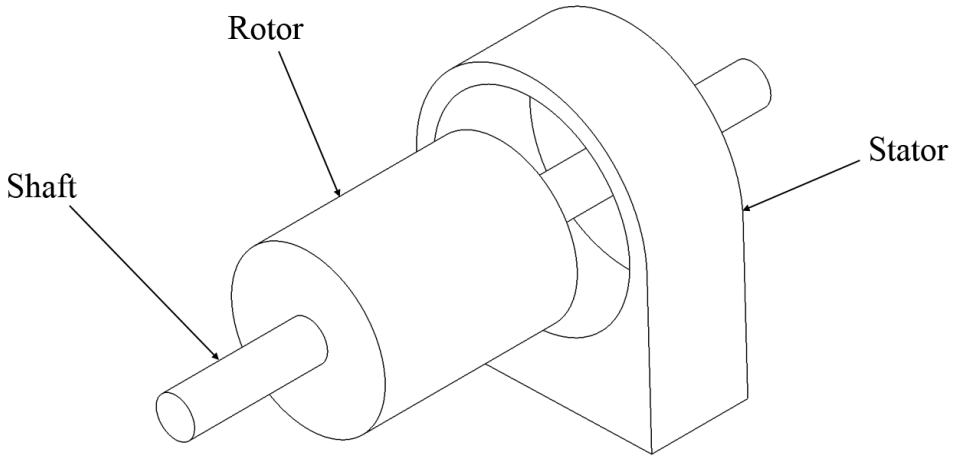

Figure 1.1: Schematic of a rotary system.

Rotating mechanical systems are oscillatory systems, and this introduces inherent problems. In particular, it makes them susceptible to unwanted vibrations. It is a key necessity to reduce or completely eliminate those vibrations because of their adverse effects. There are several factors that determine the extent of the effects, and they mainly vary by application.

In hand-held rotary power tools, for example, a major concern is health complications due to additional vibration produced by the tools. Workers may develop sensory and motor disorders due to the transmission of vibrations to the hand and arm [36]. In many cases, workers do not perceive the vibrations to be past safe

levels which poses additional risk according to a field survey carried by Vergara et al. [37] Hence, vibration suppression in this industry is health and safety oriented.

In computer systems, vibrations in hard disk drives degrade their reliability over time and can cause them to fail abruptly [38]. Similarly, in optical disk drives such as CD-ROM or DVD drives, vibration cause off-track and off-focusing errors and generate excess noise [39]. Here, unwanted vibration reduces reliability, generates noise, and may cause complete failure of the system, losing recorded data.

In aircraft engine and general turbine design, vibration has a significant effect on the fatigue, performance, and structural integrity of the system [40]. Having undesirable vibrations present in the system demands additional maintenance, reducing its operational time. Additionally, vibrations in wind turbines degrade efficiency and decrease the lifespan of the system [41].

Figure 1.2: AH-64 tail rotor [1].

In rotorcraft and propelled aircraft, reducing vibrations due to rotor imbalances has become an important part of vehicle design. There is ongoing research for the sole purpose of balancing specific aircraft rotor hubs [1, 42]. The AH-64 tail

rotor shown above in Figure 1.2 is one example of systems requiring complex balancing procedures due to the asymmetrical blade configuration. This introduces additional cost to the design, operation, and maintenance of the aircrafts. In addition to cost increases, vibration in helicopters affects the people inside and the on-board systems. Oscillatory motion of the fuselage causes crew and passenger fatigue. In medical evacuation helicopters, excessive vibrations cause some medical instruments to malfunction [43]. In military rotorcraft, excessive vibrations can degrade performance of on-board weapon systems due to difficulty in using sights [42].

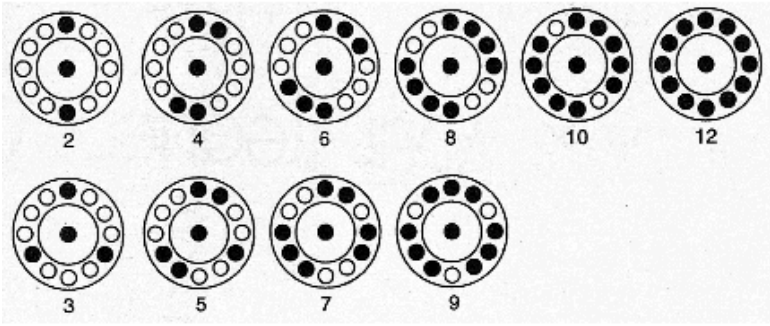

Figure 1.3: Balanced microcentrifuge configurations [2].

Centrifuges, which are used in many disciplines for a multitude of uses, are also susceptible to unwanted rotor vibration. In chemistry, biology, and biochemistry, centrifuges are used for isolating and separating compounds. Commercially, they are used in clothes dryers, oil refineries, and even wastewater treatment. They are essentially applying centrifugal loads on masses through rotary motion. Unwanted vibrations may cause centrifuge damage and sometimes destruction [44]. Micro-centrifuges, used in molecular biology, require balancing before operation. some

balanced configurations are shown in Figure 1.3.

Over the decades, many efforts have gone into the analysis of vibrations specific to rotary machines. It still remains an important topic of study given the widespread use of rotary machines. Vibrations must be studied for a variety of reasons depending on the applied domain. Suppressing unnecessary oscillations in rotary cycles can reduce fatigue, noise, energy losses, and wear and tear of the system. In some cases, reducing vibrations helps a system become more operable or more efficient, ultimately making it more cost effective.

1.2 Eccentric Rotor Vibration

When a rotating system is dislocated from its rotating axis, it is called eccentric. The system eccentricity causes off axis motion cyclically at the rate of rotation. This rotary vibration then translates to all components in the system. There are a few reasons why a system could become eccentric. First, an eccentric mass imbalance could be present in the system. This means the center of gravity of the system does not coincide with the axis of rotation. This type of eccentricity is caused from the system itself due to its configuration. The second type is external, and it can be due to any off-axis external loads that are asymmetrically distributed in the rotating plane.

1.2.1 Mass Imbalance

One source of rotary vibration is eccentric mass imbalance. A non-uniform distribution of mass in a rotating plane causes an imbalance in centrifugal loads about the

axis of rotation. Once the axis of rotation becomes eccentric, whirl vibrations are initiated. Mass imbalances are induced in many forms but they are essentially an additional mass that causes the system to be mass asymmetric (illustrated in Figure 1.4). One prominent and inevitable source of mass imbalance is manufacturing inaccuracies.

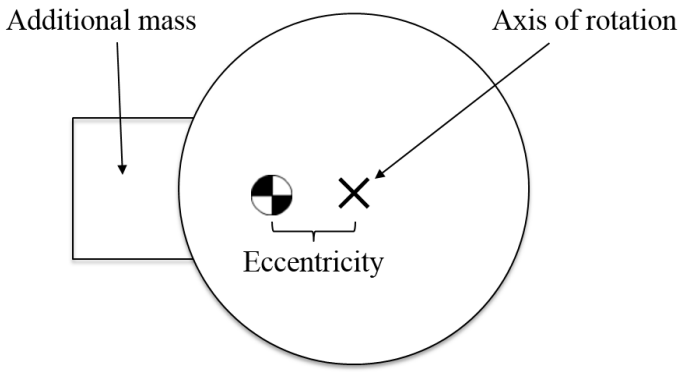

Figure 1.4: Eccentric mass imbalance.

While industrial tools for manufacturing and fabricating components continue to improve, machine tolerances continue to exist. Manufacturing process tolerances range from tens of millimeters to micrometers [3]. Manufacturing tolerances from various processes are shown in Figure 1.5 as a function of feature size. In non-rotary systems, these inaccuracies are usually tolerated. For example, to construct the Boeing 777, Boeing uses aluminum extrusion which has its own characteristic fabrication inaccuracies [45]. Straightness, flatness, concentricity, and others are tolerances that are taken into account in the aluminum extrusion process [46].

In rotary machines, small inaccuracies in manufacturing lead to unwanted vibrations. Any amount of fabrication error leads to an eccentric mass imbalance. Chao et al. [29] notes the presence of unavoidable manufacturing tolerance in

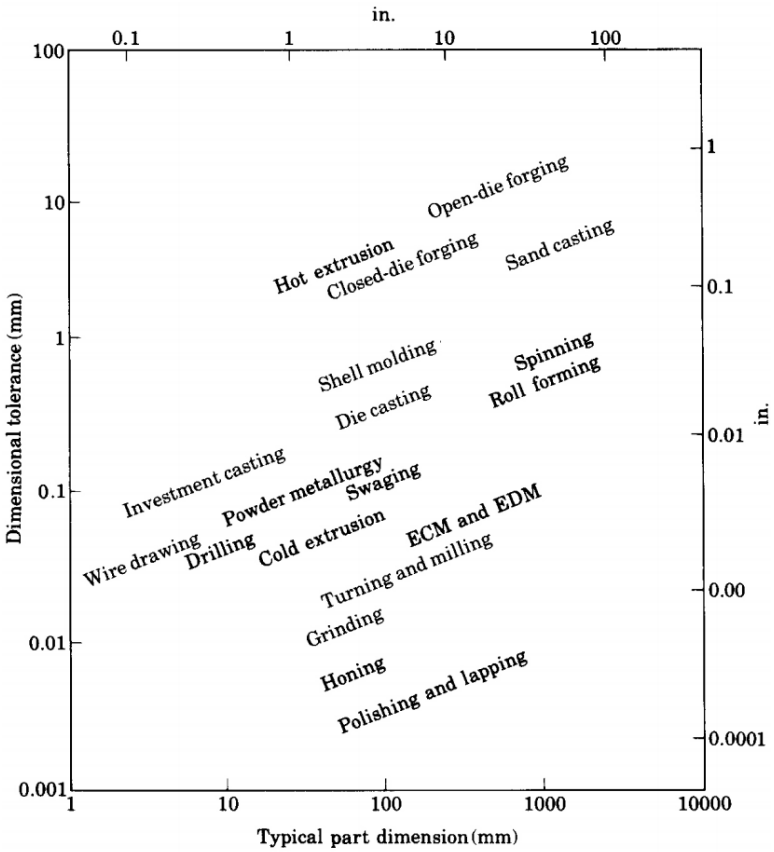

Figure 1.5: Manufacturing tolerances as a function of component size [3].

optical storage disks which are unique to each disk. There, it was shown that the imbalance results in detrimental vibrations of the system assembly when subject to high rotational velocities. Blanco-Ortega et al. [47] who studied balancing of rotor systems suggests that mass imbalance could be the result of machining errors and casting flaws.

Manufacturing defects also affect rotorcraft and turbo-machinery. Composite rotor blades highly depend on the skill of the workers making them which causes each blade to be unique in its properties. In helicopters, adjustments are needed to balance rotor-blades as soon as they are manufactured and periodically after that [42]. While the initial balancing is due to the fabrication process, the following

balancing procedures are done to correct imbalances from operation wear and damage.

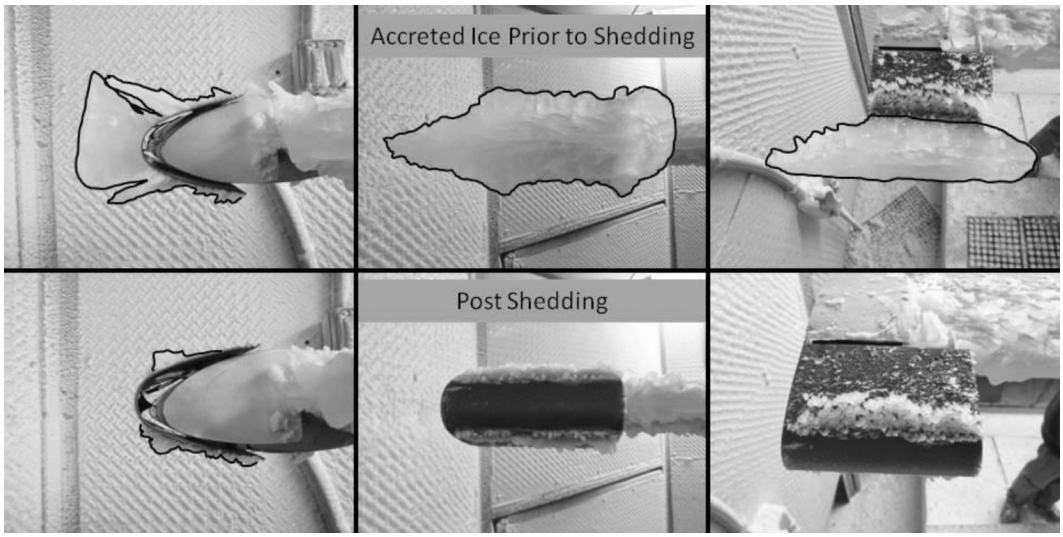

Figure 1.6: Ice shedding event on a helicopter blade [4].

One unique case of eccentric mass imbalance in helicopters occurs during an ice shedding event. Soltis et al. studied ice adhesion on helicopter blades [4]. In their experiments, natural ice shedding occurred due to centrifugal forces resulting from the accumulated ice mass. An example case of an ice shedding event is shown in Figure 1.6. Ice was allowed to accumulate on the blades in an icing chamber until the ice shed.

Strain was measured at the blade tip and the ice shedding event is captured in the sudden changes in strain (see Figure 1.7). As shown, the ice shedding events occurred at each blade independently from the other. During that time there is a severe mass imbalance in the rotor plane which induces severe vibrations in the test stand.

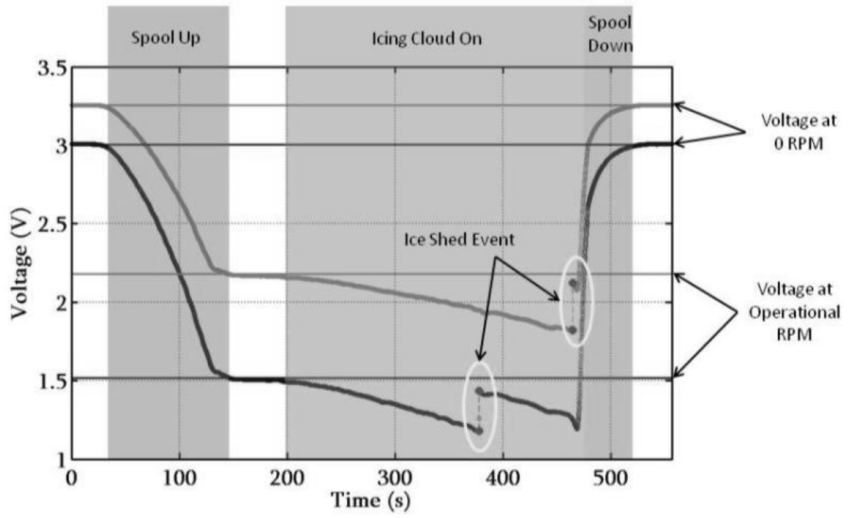

Figure 1.7: Ice shedding event recorded using strain at blade tip [4].

1.2.2 External Loads

Ice conditions in rotorcraft operating in cold climates cause aerodynamic load imbalance in addition to a mass imbalance. Ice accretion on rotor blades is known to deteriorate aerodynamic performance [48]. The shape of the accumulated ice varies between the blades which creates a variation of off-axis aerodynamic load on the drive shaft. In addition, it was discussed earlier that ice can shed asymmetrically (blade independent ice shedding). When ice is shed, the blade aerodynamic performance is restored while other blades may still have ice adhered to them. This causes an imbalanced aerodynamic load in the rotor plane which causes eccentric shaft vibration.

Dynamic loads are another cause of vibration that is not due to mass imbalance. In this case, the dynamics of the components fixed to the rotating system behave differently and asymmetrically during operation. Given a mass balanced rotating structure, if one component (i.e. blade) is stiffer than other components in the

same plane, it will result in different dynamic response between the components. This is an off-axis load which can induce eccentric vibrations.

In addition to in-plane off-axis loads, loads that act on the systems boundary conditions may contribute to asymmetrical excitation. Power tools which are designed to be operated by hand by a person are a notable example. Extensive studies have been completed to model the biodynamic behavior of the hand-arm and vibration excitation of tools [49, 50]. Such excitations cannot be ignored when investigating rotor vibrations due to eccentric loads.

1.3 Current Vibration Control Methods

To develop a an improved passive balancing method, it is essential to review current methods of controlling undesirable in rotary systems. Many methods have been developed to reduce imbalance-induced vibration. Those methods can be categorized as active, semi-active, and passive systems. Each class of vibration control has its advantages and disadvantages. This section is a comprehensive overview of the capability of each system to mitigate vibrations.

1.3.1 Active Vibration Control

Active vibration control (AVC) adjust the system by using actuators or active devices in response to instantaneous operating conditions measured by the corresponding sensors. AVC systems consist of a dedicated controller, sensors, and a means of actuation to actively attenuate vibrations. The advantage of active control systems is their ability to adapt to different load conditions and scenarios. In addition, one

system design could handle multiple system configurations. Active vibration control systems are generally burdened by their significant power needed to operate.

The active balancing schemes rely on information about the eccentricity of the rotating system. There is vast literature covering the topic of controller models. Goodman first described a conventional least squares method for balancing rotor systems in 1964. In the procedure he proposed, plain least squares are used to minimize rms residual vibration, and then weighted least squares are used to reduce maximum residual vibration [51]. In 1972, Lund et al. experimentally quantified the accuracy of the method provided by Goodman and showed that it is valid when calibrated instruments are used [52]. Lee et al. also demonstrated experimentally that the least squares method is effective in modal balancing of flexible rotors during operation [53]. Recently, Dyer et al. suggested an improvement to the least squares method, where they introduce weighted terms penalizing control effort and control speed of response to the weighted least squares vibration objective functions [54].

In certain cases, the least squares controller is not viable. For instance, in a study on vibration control in jet engines, Manchala et al. demonstrated that least squares predictions in a control system were not necessarily adequate when there was a system limitation, such as actuation force [55]. Instead, they employed a constrained quadratic programming method which addressed the limitations of actuators and power amplifiers, and proved effective at suppressing sudden imbalance vibration. The mathematical theory on quadratic programming with bounded constraints was detailed by Gill et al. in 1984 [56, 57].

Another active controller approach was used by Blanco et al. which promises

robustness and speed over the conventional least squares method [58]. The algebraic parameter identification approach was first described by Fliess and Sira in 2003 [59]. Numerical simulations and experimental results done by Beltran et al. attest the speed and high robustness of the method against parameter uncertainty, frequency variations, and measurement errors and noise [60, 61]. In 2008, Blanco et al. tested multiple nonlinear controllers that incorporate the algebraic identification for eccentricity estimation in numerical simulations and they proved effective [12, 47].

Similar to the existence of multiple approaches to active system controllers, there are multiple approaches to actuation in active control systems. The first type of actuation involves direct shaft influence by means of exerting external forces to correct shaft eccentricity. This type of actuation has been studied extensively, and has been achieved by many novel mechanisms.

In 1993, Palazzolo et al. designed and tested a piezoelectric actuator based AVC [5]. The experiment included several piezoelectric pushers – each consisting of a stack of piezoelectric ceramic disks connected in parallel electrically. The piezoelectric actuators were represented by a series of dampers and springs in their model (see Figure 1.8). While the result the Palazzolo et al. study showed significant reductions in vibration levels along the rotor shaft, the control system used had to be carefully calibrated for each rotational velocity of the system [5].

Another study on piezoelectric actuation in active control systems was completed by Carmignani et al. in 2001 [6]. In their report, tests demonstrated that vibration reduction in a slender shaft is possible through controlled movements of a suitably placed bearing using piezoelectric actuators. The implementation of piezoelectric actuator based AVCs is limited for small size rotors based on the characteristics

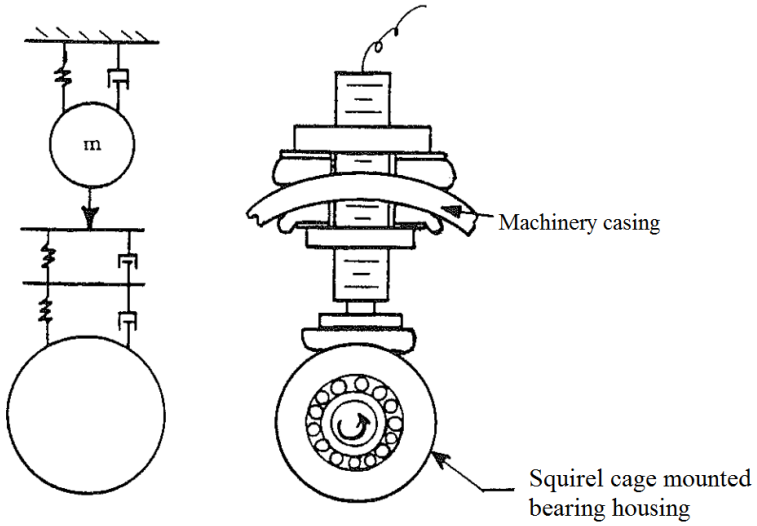

Figure 1.8: Model representation of a piezoelectric pusher [5].

of current piezoelectric actuators [6]. A possible active vibration control system configuration with piezoelectric actuators is shown in Figure 1.9.

Active magnetic bearings (AMB) offer several advantages over conventional mechanical roller bearings and actuation methods. They do not come in contact with a bearing requiring no lubrication, reducing frictional wear and eliminating support bearings as a source of vibration. In addition, given the nature of electromagnetic actuation, vibration control can operate at temperature extremes [62]. The combination of advances in computing and advantages of active magnetic bearings has attracted a great deal of interest since AMBs can be controlled digitally and quickly. Magnetic bearings can be used to apply external forces on a drive shaft without coming into contact unlike piezoelectric actuators.

In 1995, Knospe et al. conducted a study on control systems for active magnetic bearings [7]. A theoretical model was establish along with a control system. Numerical simulations were completed and showed vibration reduction can be

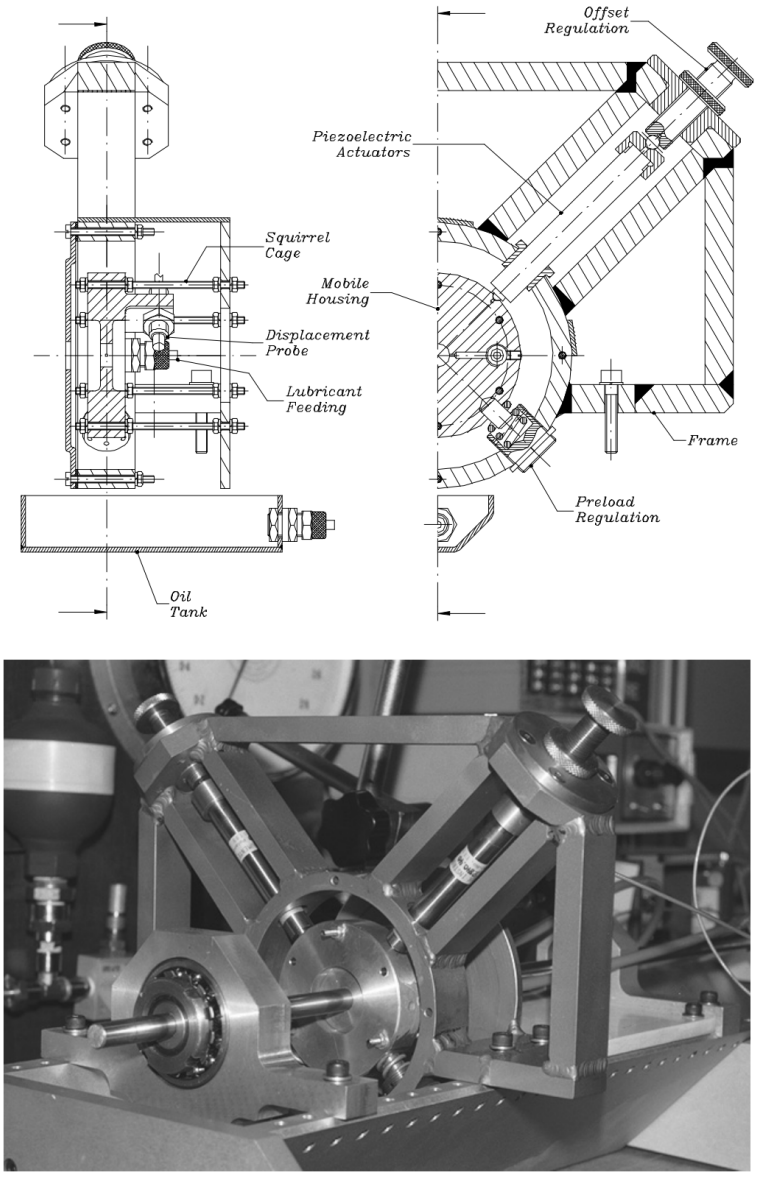

Figure 1.9: Active control system with piezoelectric actuators [6].

obtained over the entire operating speed range of a rotary system. The concept of an active magnetic bearing with open loop control that was used by Knospe et al. is shown in Figure 1.10. Knospe et al. later confirmed their predictions along with new algorithms experimentally [62]. DeSmidt et al. lead an effort on improving active magnetic bearing control in 2004 [63], and later demonstrated

effective helicopter tail-rotor balancing under various loading conditions [64]. Active magnetic bearings are promising but their use is limited by their low stiffness and the need for additional conventional bearings as emergency backups [6].

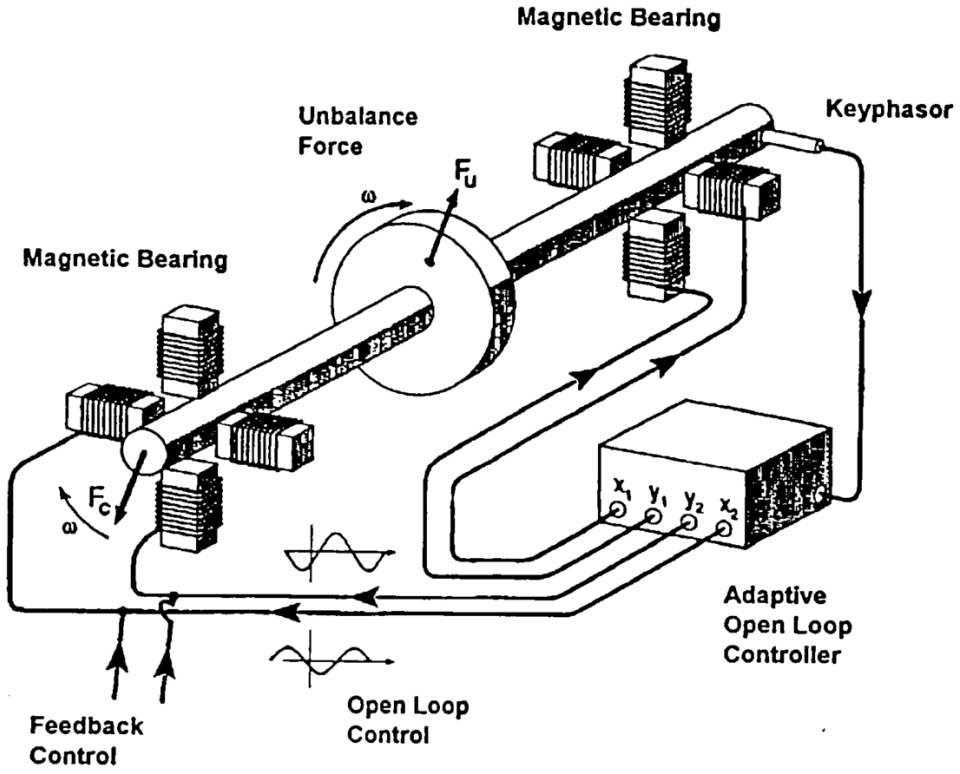

Figure 1.10: Concept of an active magnetic bearing [7].

Another type of actuation that has been studied is hydraulic in nature. Santos and Russo developed an actuated bearing system using hydraulic pumps and valves that are radially distributed [8]. A conceptual system is shown in Figure 1.11. Deckler et al. suggested hydraulic bearing are impractical as means of actuation and recommended piezoelectric actuators for their simplicity and speed in his numerical study on the control of active tilting-pad journal bearings [65].

A similar approach is used in pressure controlled journal bearings. Here, however, the goal is not actuation of the eccentric system, but, rather, actively controlling

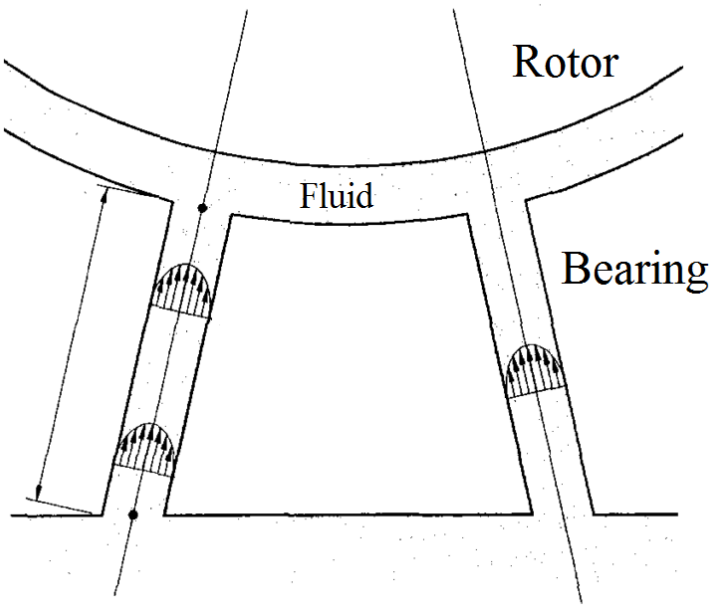

Figure 1.11: Concept of hydraulic bearing [8].

the damping in the bearing through the use of pressurized thin film lubricants. A squeeze film damper (SFD) consists of a nonrotating journal mounted on the external race of a rotating bearing. The gap between the journal and the external housing is filled with lubricant. Lunricant is provided as a splash from the rolling bearing lubrication system or by a dedicated presure delivery system [9]. SFDs have been largely used in most aircraft turbines designs since 1970 [66].

A hybrid squeeze film damper for active control of rotors was patented by El-Shafei in 1992 [67]. The advantage of HSFDs is their ability to be tight sealed in addition to behaving like an SFD where an open ended lubrication system is deployed [68]. Burrows experimentally demonstrated that an SFD capable of providing two levels of damping (HSFD) mitigates rotor vibrations more effectively [69]. Hathout et al. worked on a control system model for HSFDs that is senesitive to sudden imbalances [70]. In a 2010 study by Chang et al. [71], it was shown that

HSFDs are also capable of reducing subsynchronous vibrations where SFDs could not.

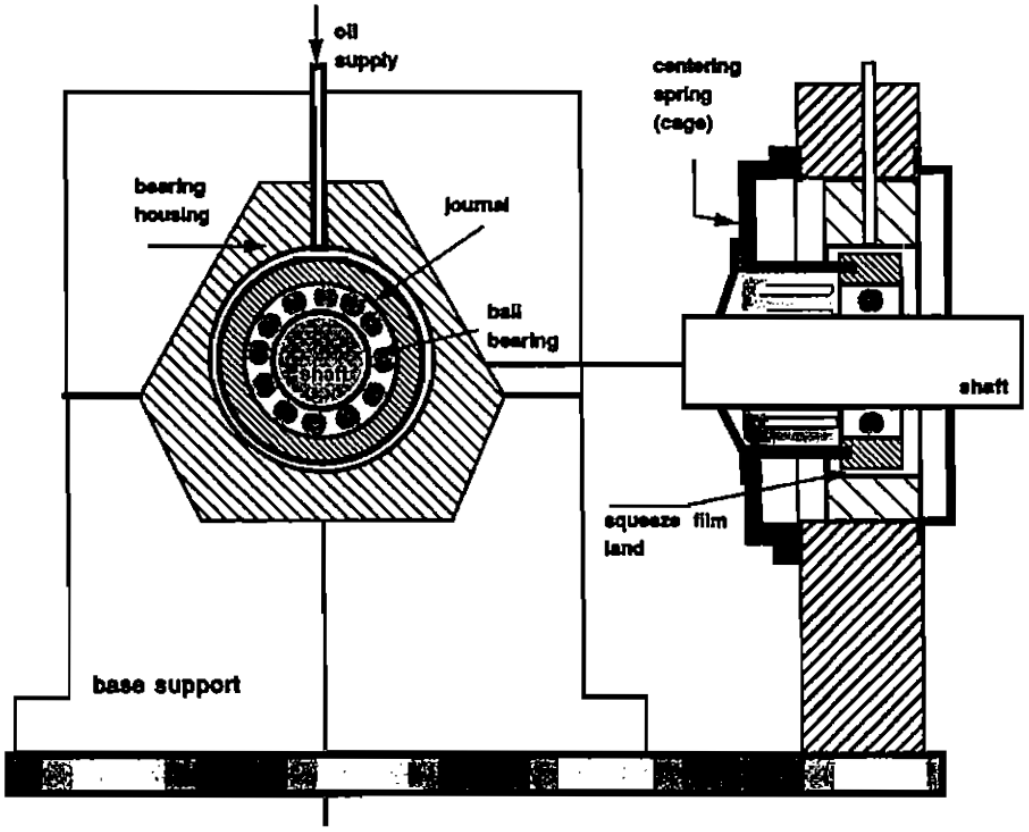

Figure 1.12: Schematic of a squeeze film damper [9].

The lubricating material in squeeze film dampers has also been studied. While it has been shown that oil lubrication is successful at reducing vibrations and improving system stability [72], possible SFD enhancements through the use of other fluids were sought after. In 2000, Guozhi et al. designed and tested an electro-rheological (ER) fluid based SFD [73]. In that experiment, the ER based SFD was effective in attenuating vibrations using existing control systems. In addition, the transient response was shortened and steady state vibration amplitudes decreased. In 2006, Wang et al. studied the use of magnetorheological (MR) fluids in SFDs [10].

Their results showed similar outcomes to ER fluid based SFDs with no improvements specifically due to the use of MR fluids over ER fluids. An MR fluid based squeeze film damper is illustrated in Figure 1.13.

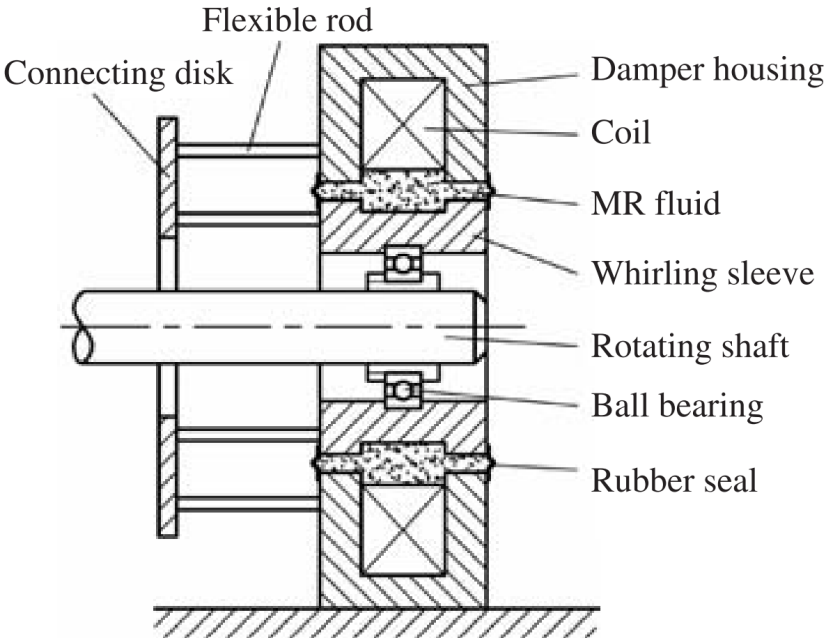

Figure 1.13: Schematic of a magnetorheological fluid based squeeze film damper [10].

A third approach to active vibration control is active balancing. Essentially, a control system is used along with an actuation strategy to displace rotating masses. This can negate shaft eccentricities since all imbalanced can be eliminated. In 1981, Van de Vegte proposed a motorized gear bearing where controlled redistribution of mass can be achieved [11]. An illustration of the system is shown in Figure 1.14. The gears shown rotate to place masses in ideal locations calculated to negate eccentric vibrations. The results were promising and balancing was shown to be possible. However, the system, in certain scenarios, required many adjustments to the masses to be done which caused suboptimal performance. In 1982, Bishop

provided a simpler method of controlling the Van de Vegte balancer [74].

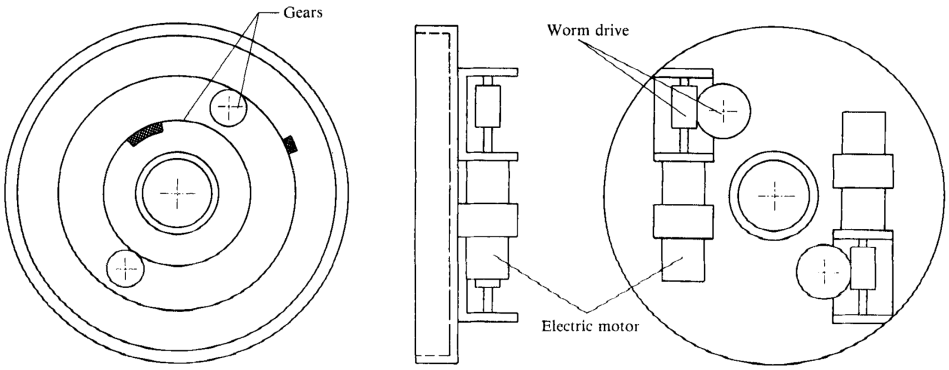

Figure 1.14: Active vibration reduction using motorized gears [11].

In 2008, Blanco et al. developed a control system for an active disk bearing where ball masses are placed on a micromotor controlled screw [12]. The masses could be translated radially to balance an unbalanced system. Through numerical simulation, the active balancing disk was shown to completely eliminate residual vibrations from an unbalanced rotor configuration. The system used in the study is shown in Figure 1.15.

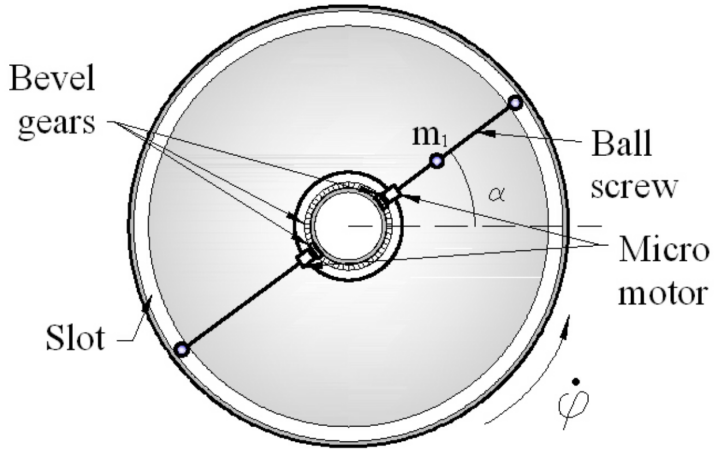

Figure 1.15: Possible active balancing configuration [12].

Hredzak and Guo attempted to solve the active eccentric rotor balancing using an electromagnetic release mechanism to manipulate the position of balancing masses [13]. Their attempt was aimed at removing vibrations in servo track writing used in the hard disk drive industry. Their system consisted of permanent magnets that held ball masses in an initial position. Electromagnets are then selectively activated using a control system which moved the ball masses to a different position. The configuration is illustrated in Figure 1.16. Experimental results from the study demonstrated the system is effective at eliminating vibrations.

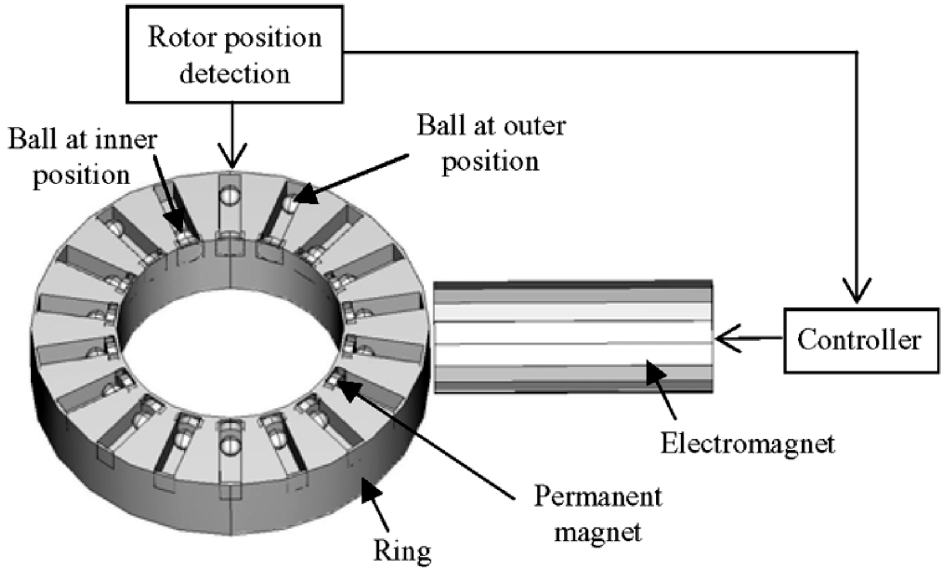

Figure 1.16: Active balancing using electromagnetic releases [13].

Active balancers have recently been used in industry. Hildebrand and Miller of LORD corporation were granted a patent for an active dynamic balancer [75]. Its composed of weights that can be adjusted to account for imbalances. Its key advancement, however, is its ability to attenuate torsional vibrations in addition to eccentric vibrations using resonating springs. LORD's Real Time^{TM} Balancing

System is commercially available for rotary systems. Generally, active balancer performance is satisfactory. However, they add weight, complexity, power consumption, and they require additional maintenance.

There are other non-conventional ways of actively suppressing vibrations in rotary machinery. Some research has proposed modifying a system configuration during operation. In 1984, Goodwin et al. was able to significantly shift rotor critical speeds by varying pressure in pressurizing bearings [76]. This is different from squeeze film dampers because, additionally, the stiffness of the system was modified.

Another "on-line" system reconfiguration was studied by Blanco et al. in 2003 and, more recently, in 2010 [14, 77]. In both studies stiffness was modified by means of a automatic traversing bearing that changed the effective length of the rotating shaft. While the results are promising, it is often impractical to perform system reconfigurations during system operation. In addition, it is complex, bulky, and requires additional maintenance. The system modeled by Blanco et al. is shown in Figure 1.17.

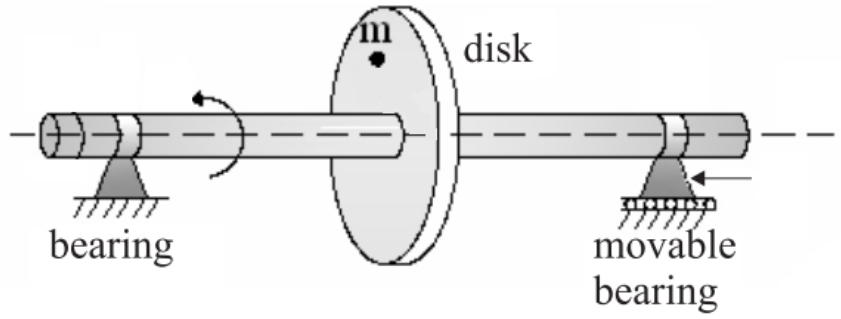

Figure 1.17: Active balancing by means of system reconfiguration [14].

So far, all active vibration control systems discussed targeted general rotary

system vibrations including those due to rotor imbalances. One type of AVC system targets vibrations due to bearing and seal instabilities. If any fluids, including lubricants, are present in a rotary system's bearings, the bearings can be a source of instability because of the induced motion of the fluids by the rotation of the shaft. Muszynska et al. proposed a bearing system with active control that injects fluid in a backward circumferential flow to counter the swirl generated by the shaft rotation [15]. The study concluded that the anti-swirl active control system helps in transient conditions such as start-up, shutdown, and resonant speed passage. An idealized anti-swirl control system is shown in Figure 1.18.

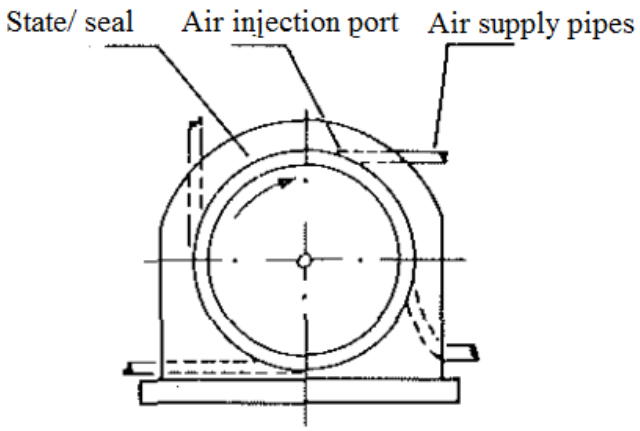

Figure 1.18: Anti-swirl bearing [15].

1.3.2 Semi-active Vibration Control

Semi-active vibration control (SAVC) systems have garnered interest especially in applications where weight and power are limited, and safety is critical. The primary difference between active and semi-active vibration control systems is the means of influencing the vibrating system. In active systems, power is transformed to exerted forces that act on a system to counter vibration. In semi-active systems,

power is used to modify system properties which results in forces that mitigate vibration. Semi-active vibration control systems offer some of the adaptability present in active control systems, but require much less power to operate.

Typically, semi-active systems integrate a variable parameter scheme into passive devices like springs and dampers. SAVCs can be considered adapting tuned vibration absorbers. Tuned vibration absorbers are a method of vibration reduction. They are essentially coupled springs and dampers. Semi-active vibration control systems incorporate controllable spring stiffness, controllable damper damping or both. An illustration of all three types of vibration control is shown in Figure 1.19. The semi-active system notably has controllable spring and damper coefficients.

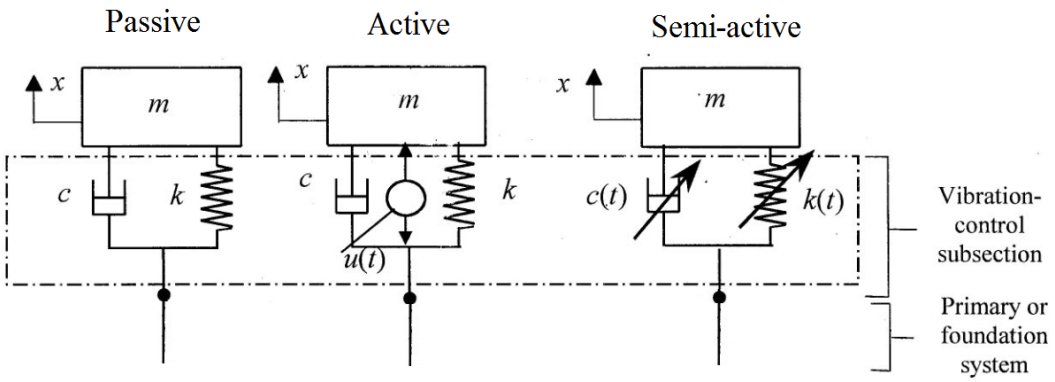

Figure 1.19: Typical structure of vibration control systems [16].

Many studies have been conducted for the design and analysis of semi-active vibration control systems. In 1974, Karnopp et al. first provided a sophisticated control model of a semi-active vibration control system with a controllable damper (see Figure 1.20) [17]. In the study, computer simulations showed that it was possible to design a semi-active device that effectively damped vibrations.

Several methods have been proposed to achieve controllable damping. In 1979,

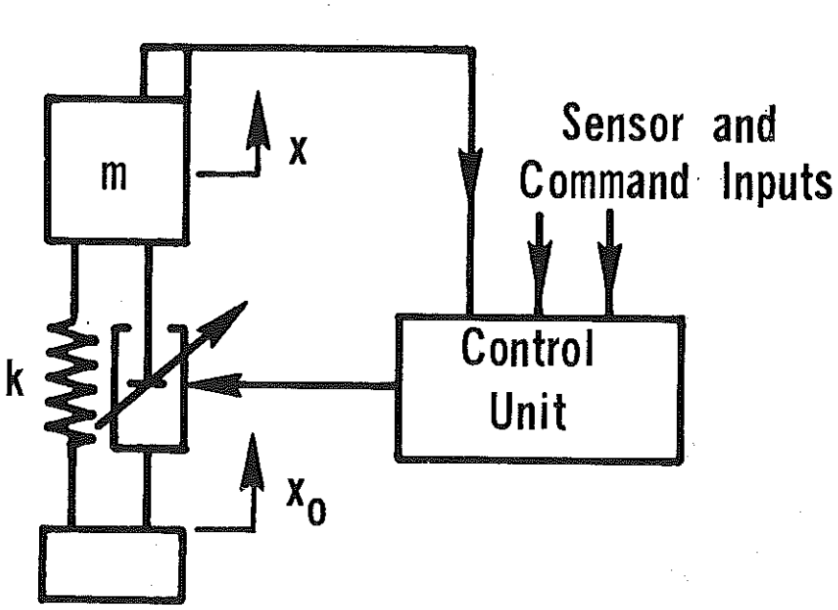

Figure 1.20: Vibration control system with semi-active damper [17].

Nikolajsen et al. used an electromagnetic damper for vibration suppression on a transmission shaft [78]. The experiment confirmed that contactless, controlled damping of a supercritical shaft is possible with electromagnetic dampers. Electromagnetic dampers are able to change the damping properties in accordance with the current flowing in the winding coils.

A dry friction damping control method was proposed by Stammers and Sireteanu in 1998 [79]. In the advent of controllable fluids, new techniques were brought into semi-active damping control. Mainly better understand of electro-rheological (ER) and magneto-rheological (MR) fluids emerged. The fluids viscosity can be modified by applying an electric field or magnetic field respectively. In 1990, Nikolajsen and Hoque performed an experiment on a flexible rotor using an ER fluid based electroviscous damper [80]. It was experimentally demonstrated that the ERF based damper is effective at circumventing imbalance induced vibrations at supercritical

speeds.

Zhu analyzed the effectiveness of an MR fluid damper in controlling the vibration of a rotor system analytically and experimentally [18]. A schematic of the controllable damper is shown in Figure 1.21. The effectiveness of the MR fluid based damper was similar to the ER fluid based damper. However, Zhu concluded that voltage used to adjust the dynamic characteristics of the rotor system was much less than those used by an ER fluid based system [18] performing the same task.

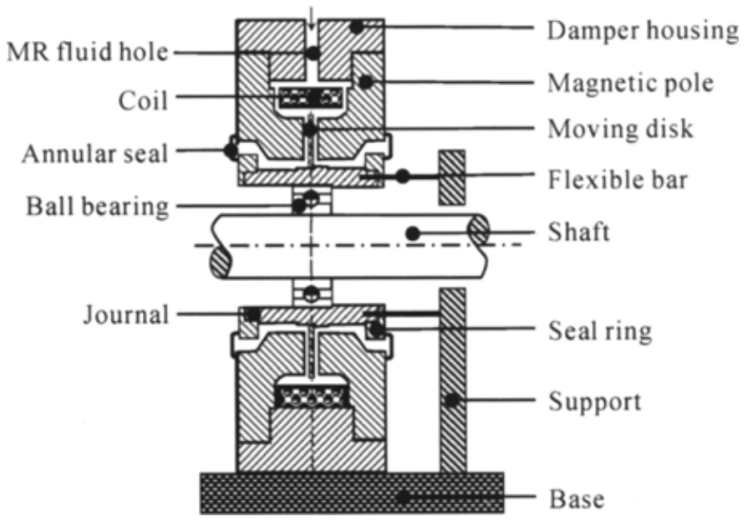

Figure 1.21: Cross-section of a magneto-rheological fluid damper [18].

Stiffness variation is another approach to semi-active vibration control systems. Stiffness of the system is modified instead of the damping. In 1992, Onoda et al. derived a control system for a single degree of freedom system with vibration suppression using variable-stiffness [19]. In the same study, an experiment was conducted to suppress vibration in a string and demonstrated the effectiveness of the semi-active system. An idealized illustration of the system proposed by Onoda

et al. is shown in Figure 1.22.

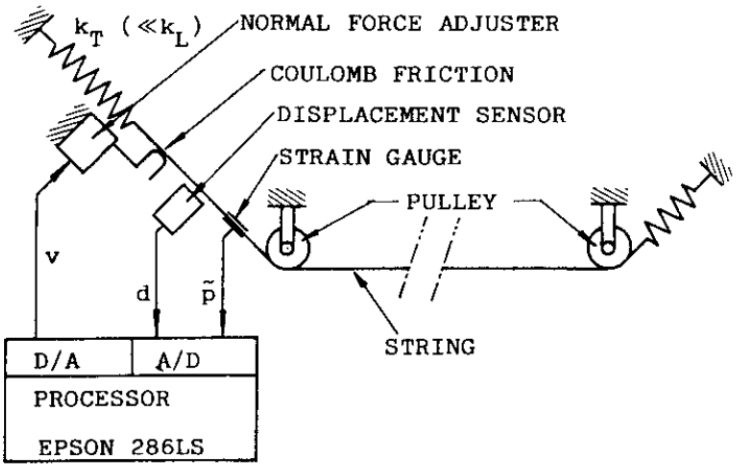

Figure 1.22: Variable stiffness vibration control system [19].

In the same year in 1992, Walsh and Lamancusa studied a variable stiffness vibration absorber for rotary systems with imbalanced rotors [81]. A model was formulated and the system response was studied numerically. It was shown that a variable stiffness spring could provide sufficient stiffness variation to significantly reduce peak displacements. Physical implementations of the system were also proposed.

Liu et al. modeled a combined variable stiffness and MR fluid based damper system as a semi-active device for vibration isolation in 2008 [20]. The study proposed a simpler approach to variable stiffness using a combination of dampers and springs in series. An illustration of the concept is shown in Figure 1.23 and a schematic of the experiment done is shown in Figure1.24.

The advantage of the damping controlled variable stiffness is its simplicity and practicality in application. The semi-active system was shown to isolate vibration [20]. Semi-active devices have had a history of application outside of

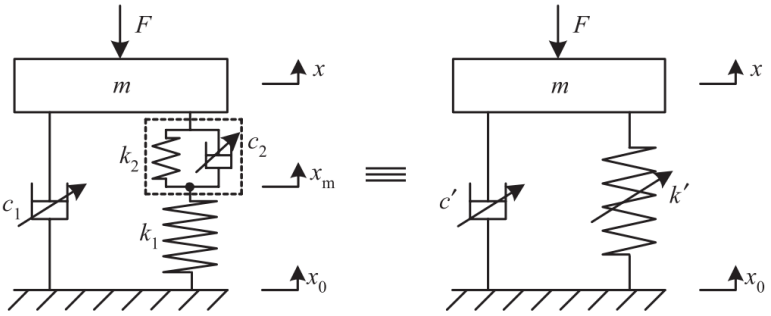

Figure 1.23: Variable stiffness through controllable damping [20].

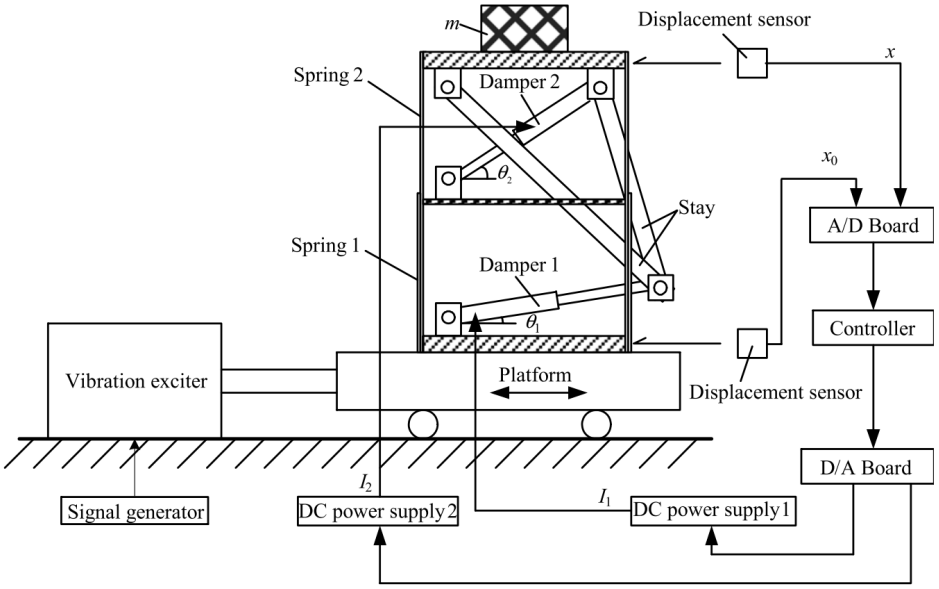

Figure 1.24: Physical realization of the Liu et al. semi-active system [20].

rotary machinery for their excellent vibration isolation. Those systems have become popular in the transportation industry - especially, in motor vehicle suspension systems. The semi-active approach does not require large amounts of power and, generally, provides better vibration control than passive systems.

In 1992, Yi et al. performed a study and experiment on semi-active suspensions to reduce tire forces in vehicles [82]. The approach was strictly reliant on controllable dampers similar to the earlier designs (See Figure 1.20). The study confirmed that

semi-active suspensions can dramatically reduce tire forces. Redfield completed a similar study which demonstrated increased suspension performance when using semi-active vibration control systems [83].

SAVC systems are heavily used in structural vibration isolation. Kawashima et al. performed a study that showed reduction in structural displacement and acceleration of bridges in earthquakes when variable damper systems are employed [84]. Symans and Constantinou studied the use of semi-active fluid damping devices in seismic isolation to protect structures [85, 86].

The variable stiffness approach was also applied to structural vibration isolation. In 1996, Yang et al. were able to show that a variable stiffness system is effective in controlling the structural response associated with earthquake excitation [87]. In 1999, Gavin and Doke studied the effectiveness of variable stiffness and damping systems in suppressing structural resonance in buildings [88]. Recently, Yang et al. conducted a study on large scale MR fluid based dampers for structural vibration reduction [89].

There has been interest in semi-active vibration control systems for use in helicopters. Anusonti-Inthra studied the viability of using such devices to reduce vibrations from helicopter blades [90]. He applied both the variable stiffness and variable damping approaches.

1.3.3 Passive Vibration Control

Passive vibration control is an alternative to active and semi-active systems. The main advantage of active systems is the fact that they require no external power to operate. The drawback of such devices, however, is their inability to adapt to

changing operating conditions or unforeseen events.

A passive vibration control system consists of a constant stiffness element and constant supplemental damping as shown in Figure 1.19. In a review of passive damping systems, Johnson categorized passive damping into four categories; viscoelastic, viscous, magnetic and passive piezoelectrics [35]. He also defined each systems properties which are shown in Table 1.1.

Table 1.1: Properties of various damping mechanisms [35].

	Viscoelastic Materials	Viscous Devices	Magnetic Devices	Passive Piezoelectrics
Temperature Sensitivity	High	Moderate	Low	Low
Temperature Range	Moderate	Moderate	Wide	Wide
Loss Factor	Moderate	High	Low	Low
Frequency Range	Wide	Moderate	Moderate	Moderate
Weight	Low	Moderate	High	Moderate

Viscoelastic material dissipate heat when deformed due to their molecular arrangement. This property of energy loss has been exploited as viscoelastic damping. In 1959, Kerwin investigated the damping provided by a viscoelastic layer bonded to a surface and was first to propose a predictive model [21]. His model of the viscoelastic damper (See Figure 1.25) was shown experimentally to accurately predict damping over small frequency and temperature ranges.

In 1980 Torvik proposed several structure designs incorporating viscoelastic dampers [91]. In 1990, Grandhi investigated the used of viscoelastic coatings as passive damping in large space structures [92]. Ader et al. studied the application of viscoelastic passive damping for magnetic virbation [93]. Recently, Park derived an advanced model that better represents viscoelastic dampers [94].

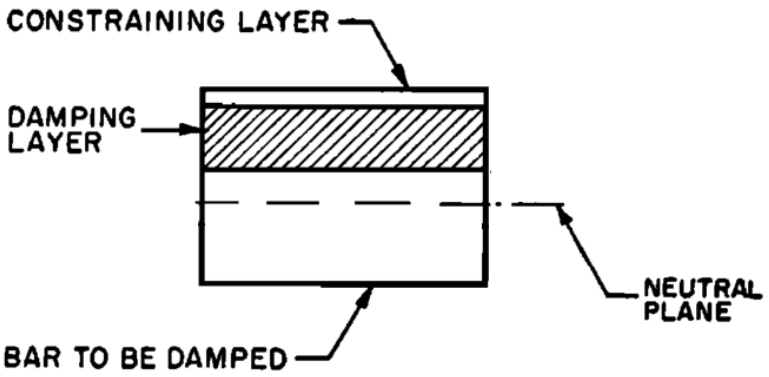

Figure 1.25: Viscoelastic damper as modeled by Kerwin [21].

Viscous devices, classically represented as dashpot dampers, operate on the principle of energy loss due to drag induced friction of a fluid. The rate at which energy is lost is dependent upon velocity. Viscous dampers provide higher energy dissipation than viscoelastic materials, however, viscous dampers are effective at a narrow frequency range or "bandwidth" unlike viscoelastic dampers [35]. Viscous dampers are vastly used in many applications as supplemental damping provided in passive vibration control systems. For instance, Symans and Constantinou considered passive viscous damping systems as opposed to semi-active systems for seismic energy dissipation in 1998 [95].

Magnetic dampers with permanent magnets are another passive supplemental damping that is used for reducing vibrations. Reaction currents, known as eddy currents, are generated when a piece of metal is placed in a time-varying magnetic field. A simple motion that generates eddy currents is illustrated in Figure 1.26. A rotating disk passes by multiple equally spaced stationary permanent magnets. The variance in magnetic field due to the rotation generates current flow as shown.

There is great interest in magnetic dampers since they lack any fluid and any contact between the damped structure and the damping system. In 1977, Weinberger

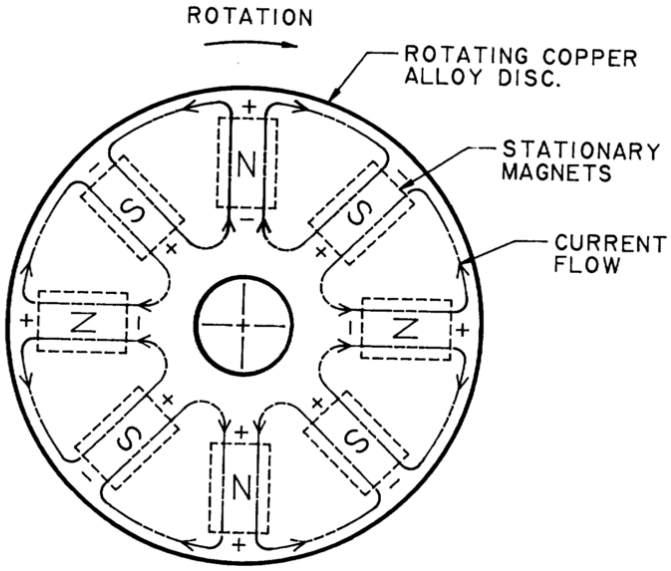

Figure 1.26: Concept of magnetic damping system [22].

studied the drag force generated by magnetic dampers in spacecraft [96]. In 1984, Nagaya and Kojima derived methods of calculating the damping coefficients of a magnetic damper with an arbitrarily shaped conductor [97]. Ellis et al. developed a high torque capacity magnetic damper for use in a large solar array deployment mechanism in a NASA report [22].

In 1994, Delprete et al. proposed a new radial magnetic damper design that could work alongside conventional rolling element bearings in rotary systems [23]. Their design is shown in Figure 1.27.

In 1998, Kligerman and Gottlieb investigated the nonlinear dynamics of a magnetic damper and provided a sophisticated model to predict its behavior [98]. One critical conclusion of the study was that while the magnetic damper reduced vibrations in the system, it was not effective in dissipating energy of synchronous forced vibrations. Synchronous vibrations include vibrations due to imbalanced rotors.

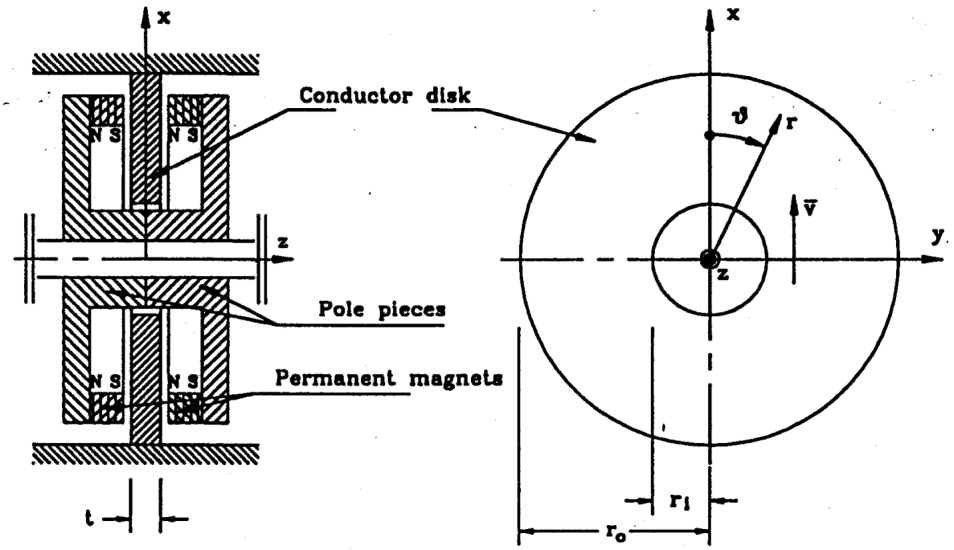

Figure 1.27: Radial magnetic damper design [23].

In 1997, Teshima et al. studied the effectiveness of magnetic damping in a superconducting levitation device which proved effective only the vertical direction [99]. Magnetic dampers were also extensively investigated for magnetic braking. Many studies have been performed to quantify the effectiveness of the passive devices [100–103].

Recently, Sodano et al. conducted a study were magnetic dampers were used for virbation suppression of transverse vibrations in a cantilever beam [104]. They provided a model which they validated experimentally. Their aim was to characterize a damping system that did not influence the structural response of the system.

Piezoelectric material has been investigated for use as a passive damper for many years. Piezoelectric material strain when an electric field is applied to them and generate voltage when subjected to strain. They have the ability to convert mechanical energy to electrical energy and vice versa. Forward first proposed the use of piezoelectric material as electronic based passive damping of vibrations in

1979 [24]. The proposed piezoelectric damper is depicted in Figure 1.28.

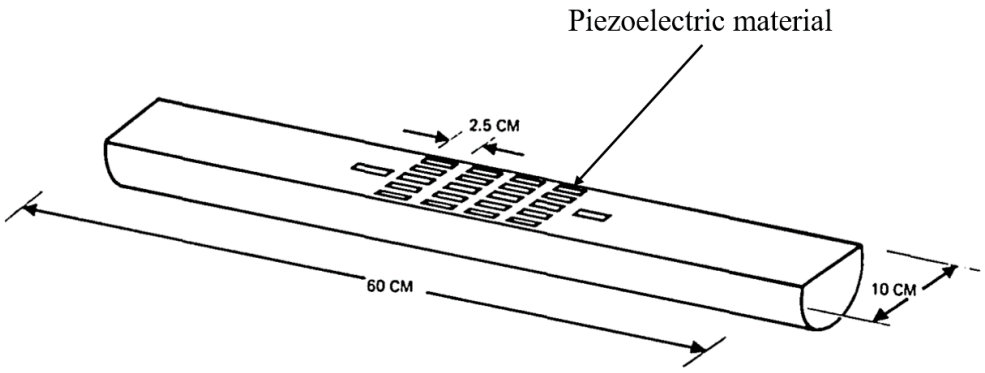

Figure 1.28: Schematic of a piezoelectric based structural damper [24].

Piezoelectric material was bonded to a structure, and then mechanical energy was converted to electrical energy. The piezoelectric material was then shunted with electrical impedance. The electrical impedance is designed to dissipate the electrical energy generated from the mechanical energy. The piezoelectric material shunted by passive electrical circuits are known as shunted piezoelectrics.

In 1991, Hagood and von Flotow developed a model of shunted piezoelectrics subject to arbitrary elastic boundary conditions to predict their compliance [105]. Their study optimized the shunting resistance for maximum piezoelectric loss factor at given frequencies. Their model was validated in an experiment on a cantilevered beam. In 1996, Law et al. characterized both the damping and stiffness effects of shunted piezoelectric material [106]. They showed in their model and experimentally that both stiffness and damping of the piezoelectric damper could be tuned to a required value per the structures needs.

Dell'Isola et al. took piezoelectric damping further in a mode and experiment using a distributed network of piezoelectric dampers [25]. In the study, they also

compared the use of two types of passive circuit networks – resistive (R) and resistive-inductive (RL). The RL network was superior in narrow-band applications while the R network proved more efficient at multimodal damping. It was shown that the technique of having multiple piezoelectric dampers reduces the required inductance (L in Figure 1.29) in the shunted circuits. The RL system modeled by Dell'Isola et al. is shown in Figure 1.29.

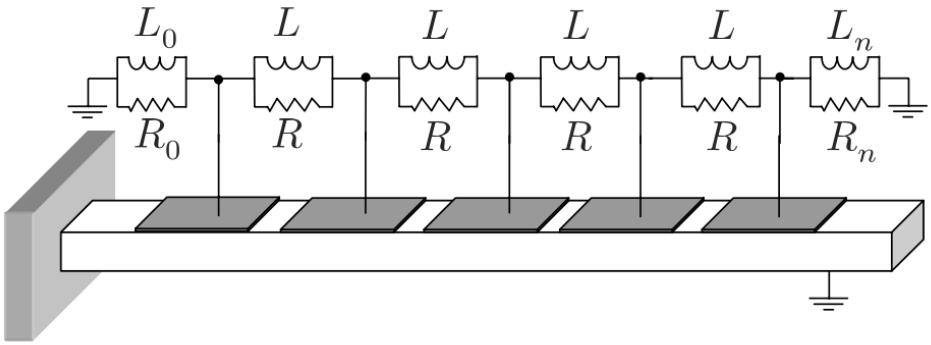

Figure 1.29: Model of a distributed piezoelectric damper system [25].

Recently, new models have been proposed with the increase in computer processing speeds. In 2006, Becker et al. modeled shunted piezoelectric structures and used finite elements to study their behavior [26]. The finite element approach allowed for understanding the effects of the piezoelectric dampers in 3 dimensions. It was found that the attached dampers had little effect on the structure mode shapes while providing effective structural damping. The insertion of piezoelectric damping into the structure is illustrated in Figure 1.30.

Shunted piezoelectric dampers have many technical applications. Kitagawa et al. proposed using such passive devices in tall buildings [107]. It was concluded from the results that piezoelectric dampers could be incorporated into large structures to reduce vibration amplitude. In a 2012 review of piezoelectric dampers, Neubauer

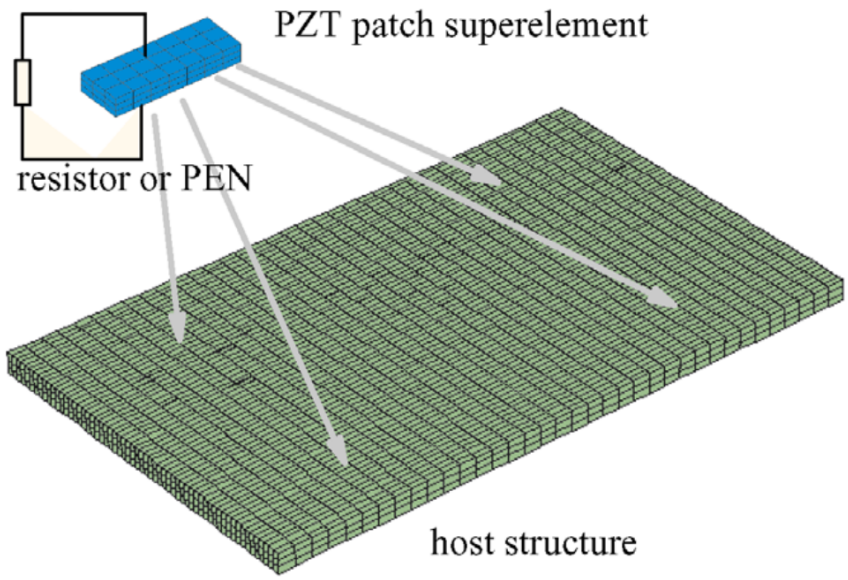

Figure 1.30: Finite element representation of a piezoelectric damper [26].

et al. analytically and experimentally analyzed two practical applications of such devices – in a disk brake and in a bladed disk [108].

Other approaches to passive vibration control have been proposed over the years. In 2004, Louroza et al. proposed a passive vibration absorption system using Coulomb damping [109]. However, vibration suppression systems based on friction require maintenance due to the expected wear of components.

Tuned vibration absorbers (TVA) are often used as passive vibration suppression devices. The essential component of TVAs is a reaction mass attached to a system through a spring with an inherent source of damping [110]. An example application of TVAs is shown in Figure 1.31. Duh and Miao designed and tested a TVA for use in rotating hubs to absorb hub vibrations [27]. The TVA was tuned for optimal performance at the hub rotational frequency. Since TVAs perform at a narrow band, they are tuned for specific harmonic vibrations. At the same time, Hamouda

studied the effectiveness of such absorbers for helicopter vibration suppression [111].

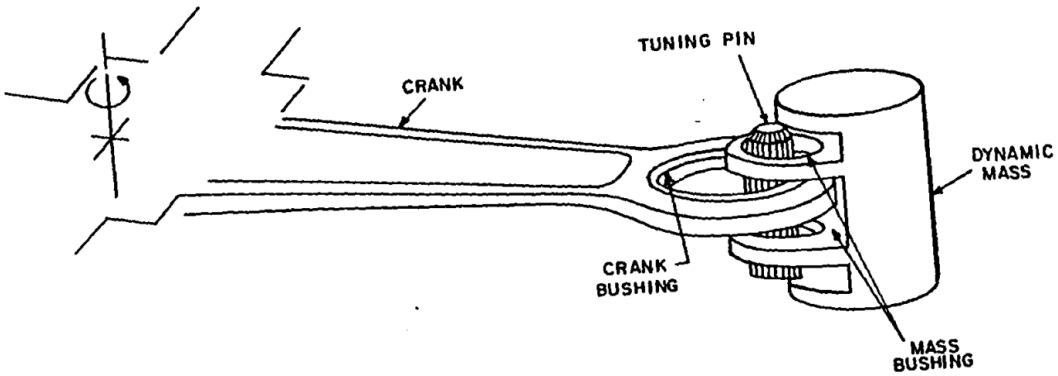

Figure 1.31: Schematic of a monofilar vibration absorber [27].

In 1986, Özgüven and Çandir analytically examined the effects of have multiple TVAs tuned to two resonance frequencies of one system operating at the same time [112]. It was shown that the performance of the TVA tuned to a lower frequency is significantly degraded by the TVA tuned to a higher frequency while the reverse was not true. Jolly and Sun analyzed the use of TVAs on acoustic radiation suppression of simply supported panels in a preliminary study [113]. They found the reduction of vibration using TVAs is possible below the frequencies at which the TVAs were tuned. In 2000, Kundra incorporated TVAs as a structural design element along with beams and masses and suggested techniques for optimization [114].

The fact remains that the tuned vibration absorbers are heavily designed for specific foreseen system vibrations. They are not effective for vibration control of changing and unforeseen dynamic responses. The last passive vibration control method discussed in this section is unique to rotary systems that are subject to mass imbalance induced vibrations. In 1919, Jeffcott described the phenomena of vibrating rotors that are "out of balance" and suggested balancing of rotor

imbalances to remedy the associated vibrations [115].

Since then, many efforts have undergone in balancing rotating machinery. In 1959, Bishop and Gladwell demonstrated that rigid rotors or rotors operating well bellow the first critical speed can be balanced by ensuring the sum of centrifugal loads is zero [116]. For flexible rotors, balancing requires much more analysis of the system. The main approaches to flexible rotor balancing are the modal balancing technique, influence coefficient technique and the unified method which combines both.

Bishop and Gladwell first suggested the modal balancing method for flexible rotors and provided an idealized model [116]. Here, it was suggested that unbalanced flexible shafts exhibit a modal eccentricity curve based on the shaft speed - hence the need for balancing mode by mode (modal balancing). They later improved the model by relaxing restrictions on shaft supporting bearings [117]. In 1963, Bishop et al. performed additional studies and experiments based on the modal balancing technique [118–120]. Their experiments showed the need for modeling shaft initial bend for accurate balancing. In 1976, Nicholas et al. provided theoretical and experimental results for balancing a single mass rotor with initial bend [121].

The influence coefficient method for balancing rotors was first suggested by Matsukura et al. in 1979 [122]. In systems where modes do not appear clearly due to large damping or complex geometry, the modal balancing method becomes impractical. Here, multi-plane influence coefficients are derived to balance the system.

In 1981, Darlow et al. proposed the unified approach to passive rotor balancing [28]. This method incorporates both the modal balancing method with the influence

Table 1 Advantages and Disadvantages of Modal Balancing

Advantages	Disadvantages
• Minimizes number of runs at highest balancing speed	• Is not valid for systems with substantial damping
• Retains good sensitivity at highest balancing speed	• Requires a high degree of operator insight
• Leaves lower modes unaffected	• Usually considers vibration at only one or two sensors
• Can be entirely empirical	• Is not easily automated

Table 2 Advantages and Disadvantages of Influence Coefficient Balancing

Advantages	Disadvantages
• Is entirely empirical	• May require a large number of runs at highest balancing speed
• Balances two or more modes simultaneously	• May not provide good sensitivity at higher modes
• Is readily computerized and automated	• Requires data for previously balanced modes
• Provides least-squares minimization of data from multiple sensors	• Use of non-independent balance planes may result in impractical correction masses
• Provides compensation for measurement errors	
• Requires minimal operator insight	

Figure 1.32: Advantages and disadvantages of the modal balancing approach and the influence coefficients approach [28].

coefficients method to eliminate the disadvantages of both. The unified approach uses the modal masses along with calculated influence coefficients. The advantages and disadvantages of the modal balancing approach and the influence coefficients approach is displayed in Figure 1.32. Experiments were conducted by Darlow et al. in 1981 and Darlow in 1987 that validated the unified approach as the superior technique [123].

In 1993, Tan and Wang used the unified balancing approach in a study and showed that under certain conditions for flexible shafts, only the balancing in low speed is necessary [124].

In 1989, Qu et al. introduced "holospectrum", a fast Fourier transform based method for fault detection and diagnosis of rotor systems [125]. In 2000, Xu et al. proposed and tested a new technique in flexible rotor balancing that required no test runs [126]. The new technique combines analysis using holospectrum and the influence coefficient method. Liu proposed a similar approach which required only low speed test runs to be performed [127, 128].

Improvements to the mentioned methods continues to improve as researchers aim to better the balancing performance and reduce the manual input needed to use the methods successfully. In 2007, Han studied the effectiveness of the available passive balancing tools for non-isotropic rotor systems and formulated a modified method [129]. Kang et al., in 2008, described an optimal approach to maximizing the accuracy of the influence coefficients used in the influence coefficient method based on sensor placement [130]. In 2010, Pennacci et al. proposed an automated method of determining the influence coefficients of a rotating system where previously it required an expert to inspect test run data. [131].

Almost all rotary systems designed and fabricated today employ one or some of the passive balancing methods mentioned in this section. Many examples in literature describe the use of those methods in ensuring minimum vibrations due to mass imbalance. Sève used the influence coefficient method to reduce vibration in refrigerant rotary compressors [132]. Liu et al. applied the holospectric and influential coefficient method to turbo-generators [128]. Passive balancing is

prevalent in the rotorcraft complex. Almost all vehicles have technical procedures to balance on-board rotors [1, 42, 133–135].

1.4 The Passive Balancing Method

Passive balancing devices or passive automatic balancing devices have been extensively studied over the years. They generally consist of two or more masses that are free to move along a circular track or channel that is concentric with the geometric center of a shaft. At supercritical rotor speeds, they exhibit the unique autonomous behavior of repositioning themselves in a way that can significantly reduce or eliminate vibrations due to rotor mass imbalances.

Let us take, for example, the response of a typical rotary system shown in Figure 1.33. The system goes through its first resonance at 1000 rpm which is when the phase of the system response shifts by 180 degrees. Three system responses are illustrated in Figures 1.34, 1.35, and 1.36 at a phase of 0, 90, and 180 degrees respectively. As shown in each illustrated system, an eccentric imbalance mass exists on a rotor disk which induces centrifugal (CF) loads on the rotating shaft. The system response is dictated by the phase at a given rotational speed. The regions are defined in an example in Figure 1.33.

For the system diagrams shown in Figures 1.34–1.36, the forces acting on a free balancing mass due to the imbalance are shown. C is the geometric center of the shaft and disk. O is the axis about which the system rotates about. Imb represents an imbalance mass and the effect it has on the center of gravity of the system is shown. When the phase of the response is 0 degrees, the shaft eccentricity grows in the same direction as the CF load. The eccentric shaft now rotates about an

axis which is not its geometric axis (see Figure 1.34). The centrifugal load on the balancing mass with respect to the new axis of rotation (O) is shown and causes the balancing mass to move towards the imbalance mass exaggerating the existing problem. This occurs when the rotation speed is sub critical where the phase is 0 degrees (see Figure 1.33).

At resonance, the phase of the system is 90 degrees with respect to the loading. This scenario is shown in Figure 1.35. Here, the centrifugal load vector from the O axis also does not cause the balancing mass to move accordingly to negate the effects of the imbalance mass. The last scenario is the supercritical one where the system has passed its resonance and is in a frequency range where the phase is 180 degrees away from the loading. Here, the eccentricity grows in a direction 180 degrees away from the imbalance mass centrifugal load. The centrifugal load on the balancing mass due to the new rotating axis now causes the mass to move away from the imbalance mass eliminating its negative effects on the system. This is, in essence, the principle concept behind the automatic balancing quality of freely rotating masses at supercritical speeds.

1.4.1 Conception

In 1916, Leblanc invented a passive balancing device composed of a liquid filled channel (mercury) to counter imbalances [136]. He claimed at certain speeds, the fluid redistributed itself automatically to reduce vibrations on the shaft. In 1932, Thearle invented the ball balancer and recognized that such device is only operable at shaft supercritical speeds [137]. He suggested the balancer to be used as a device to detect positions where masses can be added subsequently to permanently balance

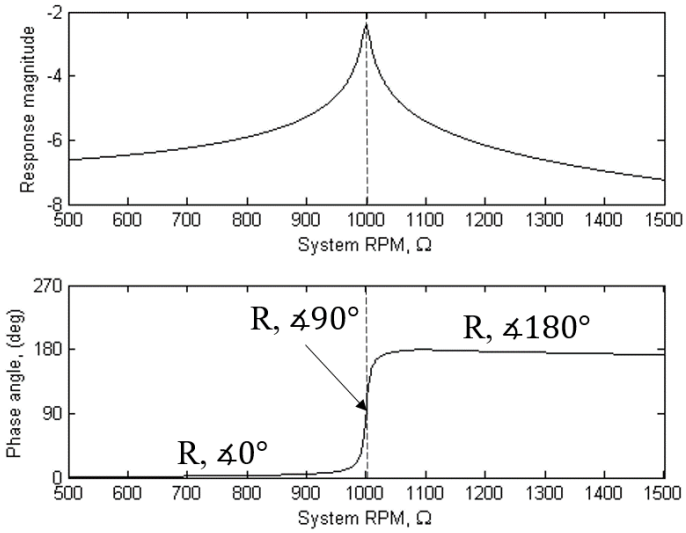

Figure 1.33: Typical rotary system response entering supercritical speed.

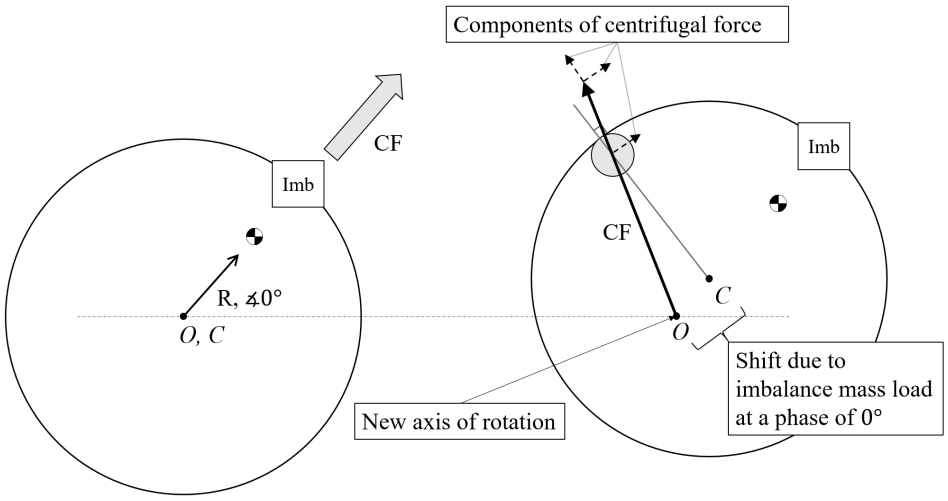

Figure 1.34: Balancing system response with 0 degree phase.

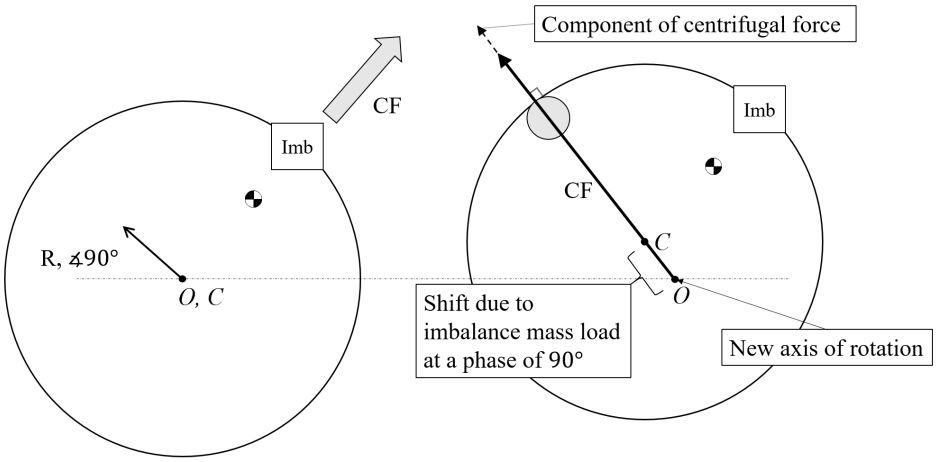

Figure 1.35: Balancing system response with 90 degree phase.

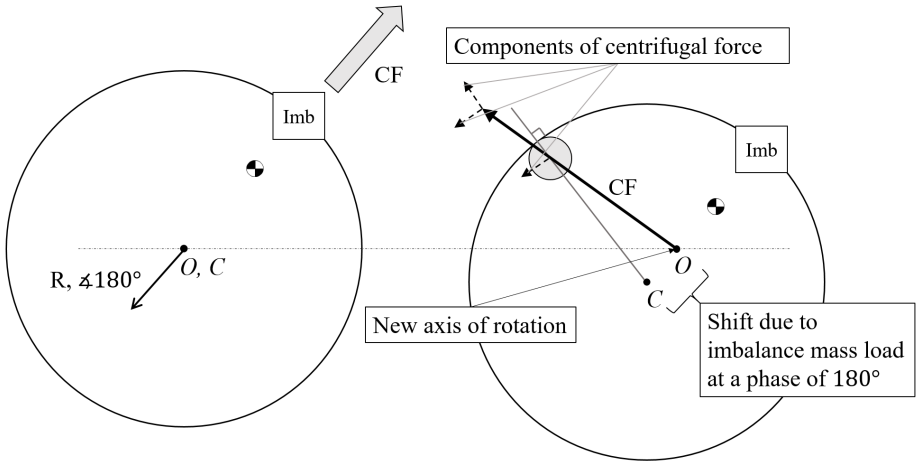

Figure 1.36: Balancing system response with 180 degree phase.

the shaft in its current configuration. Later on in 1950, Thearle experimentally studied the use of a Leblanc balancer, ball balancer and a new pendulum balancer in automatic washing machines [138, 139].

Illustrations of each balancing system are shown in Figure 1.37. Note that all the invented passive balancing systems are comprised of a concentric track with a freely moving mass such as fluid in a Leblanc balancer (Figure 1.37a) or the balls and pendulums that Thearle studied (Figures 1.37b, 1.37c). Both Leblanc and Thearle studied passive balancers without providing theoretical analysis or equations of motion for their devices.

1.4.2 Modeling Efforts

Since their invention, the need to fully understand and characterize passive balancers was a crucial step to determining their potential in practical applications. In 1967, Inoue et al. studied the dynamics of the balancer suggested by Thearle and generated equations of motion for an ideal system consisting of a balancer on spring/dashpot supports [141]. They then analytically studied the stability of a linearized system. In 1986, Kubo et al. formulated equations of motion for a simplified system consisting of multiple pendulums on a rotating disk [140]. It was found that pendulums are not as effective at reducing vibrations – at best capable of achieving 70% reduction in a very narrow range of supercritical frequencies. Otherwise, they provided less than 10% vibration reduction and introduced instability in a large range of supercritical frequencies.

In 1999, Chung and Ro generated nonlinear equations of a rotating rigid track with two balancing balls embedded [142]. They then used the perturbation method

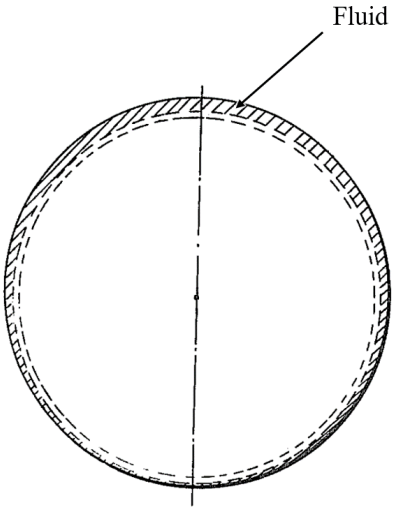

(a) Leblanc balancer [136].

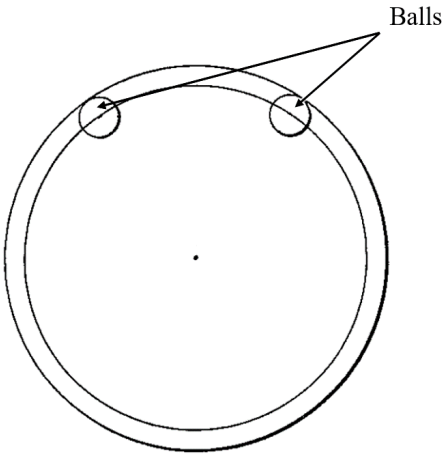

(b) Thearle balancer [137].

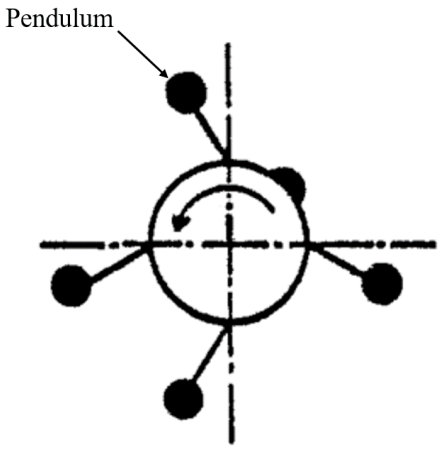

(c) Pendulum balancer [140].

Figure 1.37: Early passive balancer designs.

to derive linear variational equations. These equations were used along with the Routh-Hurwitz criteria to analyze the stability of the system with respect to the assumed viscous damping due to the ball/track interaction. Numerical simulations were conducted to test the predicted system stability profile. A very similar case study was conducted by Rajalingham et al. in 1998 [143].

In 2001, Kang et al. and Huang et al. were able to derive equations of motion using Newtonian mechanics rather than using Lagrangian mechanics [144, 145]. Lu and Lu et al. studied the stability of a single ball balancer [146] and dual ball balancer [147] accompanied with experiments. It was found there is at most one stable equilibrium position for the single ball solution and two stable equilibrium positions for a dual ball solution. Green et al. performed bifurcation analysis on a dual ball passive balancing system [148]. The nonlinear stability analysis revealed many states unique to nonlinear systems. Green et al. later analyzed a linear system and related the sensitivity of eigenvalue perturbation to the transient response of the balancing device [149].

While much of the focus has been on the modeling of the ball balancer as proposed by Thearle in 1932, several recent studies have considered the other balancing solutions. In 2007, it was shown by Sohn et al. that balancing at sub critical speeds was possible using pendulums [150]. Sohn et al. also confirmed the suboptimal performance of pendulum balancers at supercritical speeds. In 2011, Urbiola-Soto et al. investigated the stability of a Leblanc balancer theoretically and experimentally using particle image velocimetry [151].

1.4.2.1 Flexible Rotor Analysis

All described modeling efforts thus far have focused on planar balancer disks on rigid rotor shafts. Effects of out of plane vibrations or component teetering cannot be studied in a rigid planar model. Attempts have been made previously to model non-planar balancer dynamics such as work done by Bövik and Högfors in 1986 [152]. Though, here the model represented rigid components while the balancing device

was tilted with respect to the rotor. In 2003, Chung and Jang provided theoretical modeling of a passive balancing system on a flexible shaft but only considered the effects of shaft flexibility at the location of the balancer along the shaft [153]. Their model was simplified to only include the effects of the rigid body rotation of the balancer disk and the effective stiffness of a flexible shaft at the location of the balancer.

In 2007, Chao et al. modeled a rigid system with flexible support that allowed teetering [29]. The system they modeled is shown in Figure 1.38. They performed an experiment where it was demonstrated that balancing is still possible in teetering conditions. The modeling efforts on flexible shafts greatly benefited from the analytical work done by DeSmidt [30]. He provided a comprehensive theoretical model that can predict and simulate vibrations across the length of a flexible shaft with a mounted passive balancing system.

At the same time DeSmidt formulated a model to predict vibrations across a flexible shaft, Ehyaei and Moghaddam analytically studied the dynamic response of a flexible shaft with multiple passive balancers [154]. However, their approach was similar to the one used by Chung and Jang where only the response at the balancing devices is considered versus modeling the entire shaft. Ehyaei and Moghaddam found through their model that balancers demonstrated superior performance when the imbalance mass was close to the location of the balancing device along the shaft. In 2015, Majewski et al. studied the dynamics of 2 passive balancers on a flexible shaft [155]. However, their model was not a complete representation of the system. Instead, the effective loads of the balancers were imposed on the plane of interest along the shaft and the response at said plane was numerically simulated.

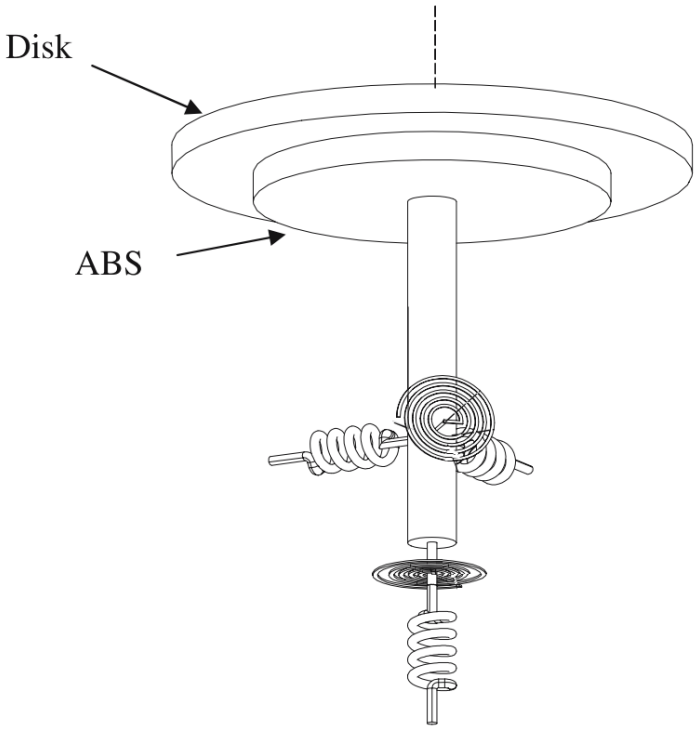

Figure 1.38: Proposed system to model flexible shafts in literature [29].

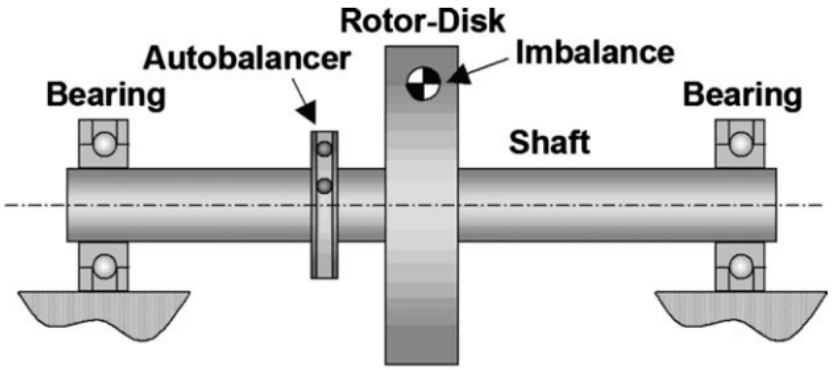

Figure 1.39: Flexible shaft system with passive balancing device [30].

1.4.2.2 Multiple Balancer Analysis

Single passive balancers on rotors have been investigated thoroughly since their inception in 1916. With the advancement of computer performance, once necessary

simplifications are no longer necessary. Thus many researchers have taken interest in studying the dynamics of multi balancer mass and multi balancer systems. In 2008, Lu and Hung examined the stability of a three-ball balancer [156]. They demonstrated that a three-ball configuration resulted in a larger stable region of operation. At the same time, Green et al. performed a similar study and confirmed the increased robustness of the system with additional balancing balls [157]. However, they noted that additional balancing masses reduced the range of permissible values for some parameters at which balancing was possible. Thus, having additional balancing masses further restrict system design. Rodrigues, in 2008, studied multiple balancing devices mounted on a rigid rotor as opposed to increasing the balancing masses within one balancing device (see Figure 1.40) [31]. Ehyaei and Moghaddam further advanced this concept by considering a flexible shaft instead [154].

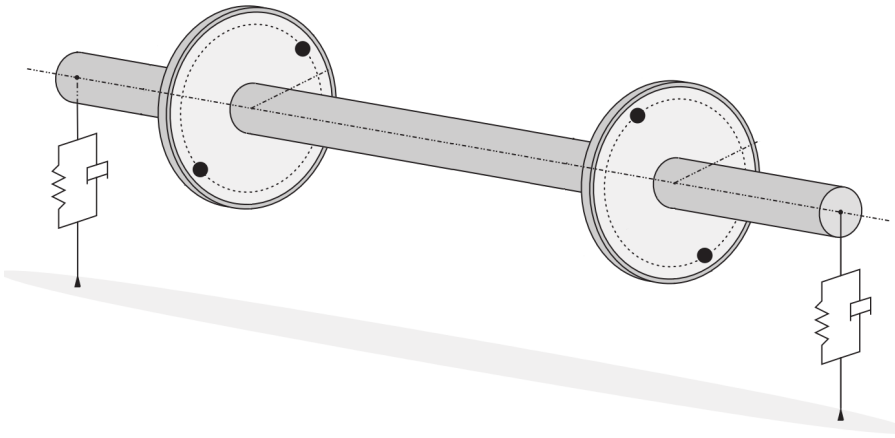

Figure 1.40: Multiple passive balancer configuration [31].

1.4.3 Performance Considerations

Passive balancing devices have been analytically and experimentally demonstrated to provide excellent vibration suppression due to imbalance mass under ideal conditions. However, there exists several considerations that require attention in the modeling, application, and design of passive balancing devices. This section outlines the possible adverse behaviors of passive balancers and their cause. It should be however noted that with careful design, most of these undesired behaviors can be minimized or completely eliminated.

1.4.3.1 Track Eccentricity

In 1988, Tadeusz studied possible sources of position errors of balancing masses [158]. He found one source of residual imbalance is the eccentricity of the passive balancing device. When the balancing device is not concentric with the shaft, the balancing masses assume positions that differ from the ideal balancing positions. Tadeusz thus concluded that pendulums attached to a rotor eccentrically cannot suppress vibrations completely. In 2002, Huang et al. performed a similar theoretical analysis and reached the same conclusion [145]. He suggested that track eccentricity ought to be minimized in balancer design for optimal performance.

1.4.3.2 Initial Conditions

Recent analysis of passive balancers have given rise to another consideration in passive balancer design. In an analytical stability study of passive balancers, Green et al. discovered that the stability and performance of a passive balancing device is sensitive to the initial positions of balancing masses [148, 149]. It was found that

for a dual mass balancer, masses initially located 180 degrees apart typically result in stable equilibrium (both masses assume fixed locations at steady state speed). Lu and Hung demonstrated numerically that varying initial positions of balancing masses can vary the length of the transient response [156].

Rodrigues et al. also performed numerical analysis of passive balancing systems and found that stable equilibrium is dependent on the initial mass positions more so than the initial mass velocities [31]. They showed through a simulated scenario that one initial condition resulted in the desired balancing while another initial condition resulted in the masses engaging in periodic motion severely increasing vibration levels. In 2010, DeSmidt also investigated the phenomenon using numerical simulation and confirmed the sensitivity to initial balancer mass positions [159]. Thus far, no experiments have been conducted specifically to test the effect that initial conditions has on achieving balanced states.

1.4.3.3 Limit Cycles

Due to the nonlinear behavior of passive balancing devices, there exists several unstable states the system could enter that cannot occur in linear or linearized systems. In 1960 and in a study involving the motion of a Hula-Hoop, Caughey first recognized that a pendulum excited by oscillatory motion at its base could enter a limit cycle state where the pendulum mass rotates periodically [160]. In a limit cycle state, the free mass rotates at subsynchronous speeds. In 1967, Inoue at al. described similar behavior in a two dimensional analytical model of a passive balancer [141].

Recently, Green et al. performed bifurcation analysis to study the dynamic

response of passive balancer masses [148]. They found stable limit cycle states can coexist with stable equilibrium states. In addition, it was shown that there exists a frequency band immediately following the first natural frequency where a limit cycle state is always reached. In 2010, DeSmidt predicted limit cycle frequency ranges and demonstrated limit cycle behavior in numerical simulations [159].

In 2012, Lu and Tien conducted an extensive analytical study on the limit cycle motion exhibited in a dual ball passive balancer [156]. They found that the resulting state of the system depends on the rotation speed history if both stable and limit cycle states coexist. They also found that if rotation speed was gradually increased, the system will enter a limit cycle state above the natural frequency and below the critical speed. After passing the critical speed, however, balancing resumes again and limit cycle state vanishes. Finally, the analysis showed that the critical speed can be reduced by increasing support damping hence narrowing the range where limit cycle states occur.

1.4.3.4 Friction

Given the physical contact between the free masses with the track or pin that define their motion, frictional forces play an important role in balancer design and performance as realized by several studies. In 1988, Tadeusz recognized that balancer mass resistive forces including friction could result in residual imbalance and therefore residual vibrations in the system as opposed to perfect balancing [158]. In 2001, Kang et al. studied the steady-state ball locations with introduced rolling friction [144]. In the year following, Huang et al. used the same approach for friction as Kang et al. to study the steady-state effect of friction on achieving

complete vibration suppression [145]. Both studies confirmed residual vibrations at steady state due to the inclusion of friction.

In 2005, Yang et al. formulated a two dimensional model of a rigid rotor and ball balancing device [161]. They performed simulations for multiple shaft speeds and did experiments with low imbalance. It was shown experimentally that friction compromises the balancing potential at low imbalance since the frictional loads are greater than the inertial loads driving the balancing masses. In the model used in this study, however, the resisting friction load was not limited. The friction could induce motion of the masses when the friction force was larger than the balancing force which is not true physically.

In 2005, Van de Wouw et al. analytically and experimentally found steady-state ball positions for a two dimensional rigid rotor system which included Coulomb friction similar to the approach used by Kang et al. and Huanh et al [162]. The results here also confirmed the deteriorating performance of the ball-type balancer at low imbalances and the existence of residual vibrations at any rotor speed. In 2012, a large effort by Ishida et al. was carried out to provide a solid understanding of the effects that friction has on balancing performance [163, 164]. Here, the focus again was on steady-state balancing mass locations in a rigid system.

1.4.4 Recent Improvements to the Balancer Design

The design of the passive balancer has remained static for decades after the work done by Leblanc and Thearle. Until recently, analysis was performed on the ideal Leblanc or Thearle balancers with little modifications. The advancement in modeling capability has allowed for new designs to be considered to remedy

some undesired behaviors present in passive balancers. Several design proposal are discussed in this section.

The first modification to the conventional balancer came in 1993. Jinnouchi et al. proposed a passive balancer with a partitioned track [165]. It was shown to reduce self-excited vibrations. In 2008, Green et al. suggested that a partitioned track avoided the need to fix balancing masses during rotor spin up to ensure the optimal initial conditions for balancing as the partitions kept them separated [157]. However, this is not be necessarily true for vibrations at sub critical speeds. Since balancers designed to eliminate a certain amount of imbalance are effective at speeds, they will be equally ineffective at sub critical speeds.

In 2011, Urbiola-Soto proposed and analyzed the use of partitions, or baffles, in a Leblanc balancer [166]. The baffles provided more robustness to the balancer due to the fluid dynamics interacting with the baffles. Ishida and Ishida et al. experimentally demonstrated that partitions do not negatively impact the balancing effectiveness of a ball-type passive balancer [163, 164]. In fact, they demonstrated that partitions narrowed the range at which the balancing balls were subject to self-excited oscillations – or limit cycle behavior. An illustration of a partitioned ball-type balancer is shown in Figure 1.41.

A unique design was proposed by Lu and Wang in 2011 incorporating a spring, ball and rod [32]. An illustration of their design is shown in Figure 1.42. In this design, the ball, or balancing mass, is able to move radially as well as circumferentially. Equations of motions were presented and system stability was examined. Through the analysis, it was found that this type of balancer possesses a larger stable region than conventional ball-type balancers. This design was analytically demonstrated

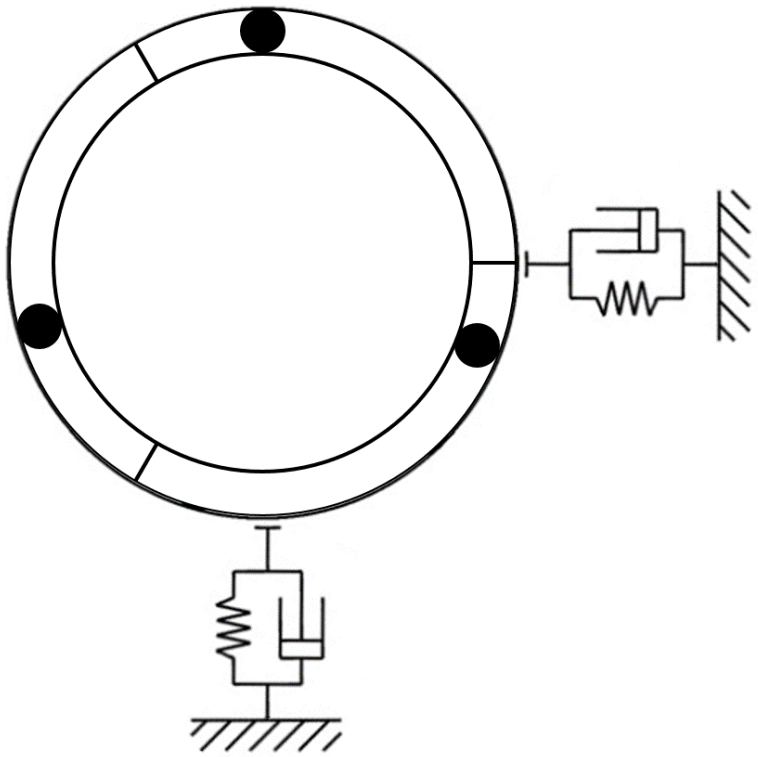

Figure 1.41: Partitioned ball-type passive balancing device.

to have a similar stability range to pendulum based balancers. However, the same analysis demonstrated that the ball-rod-spring balancer performs as effectively as ball-type balancers in speeds exceeding the supercritical speed whereas conventional pendulum balancers performed worse.

In 2012, Ishida et al. put forth a new design for ball-type passive balancers based on their work on contact friction between the balancing balls and the track walls [163, 164]. An illustration of the multi-track balancer design is presented in Figure 1.43. Ishida et al. experimentally confirmed previously predicted detrimental balancing performance when ball/track friction is accounted for. They also found experimentally that a ball-type passive balancer with multiple channels where

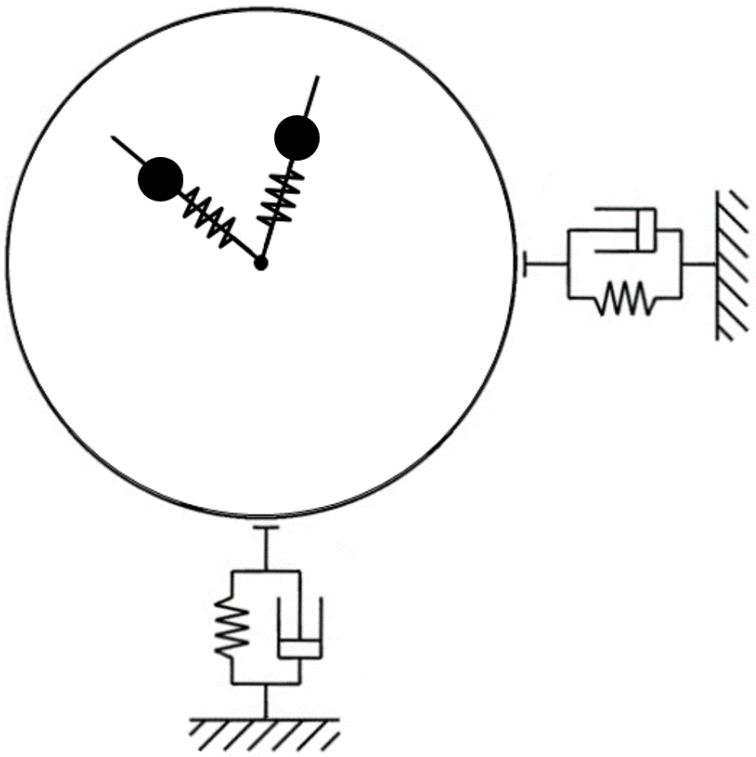

Figure 1.42: Ball-rod-spring balancer design proposed by Lu and Wang [32].

balancing balls can rotate freely reduced the negative influence of friction to ideal levels. The performance of a balancer with multiple tracks in a single plane or multiple tracks on multiple planes fixed to one another performed close to theoretical frictionless balancers.

Lastly, Kim and Na provided a novel ball-type passive balancer design that aimed to prevent the usual increase of vibration in the transient state of the response [33]. The design (shown in Figure 1.44) is comprised of a single-track, multi-ball passive balancer where springs are used to separate the balancing balls. This design guaranteed that the springs held the balancing balls at ideal initial positions for stable equilibrium. The same mechanism of fixing initial positions allowed for a

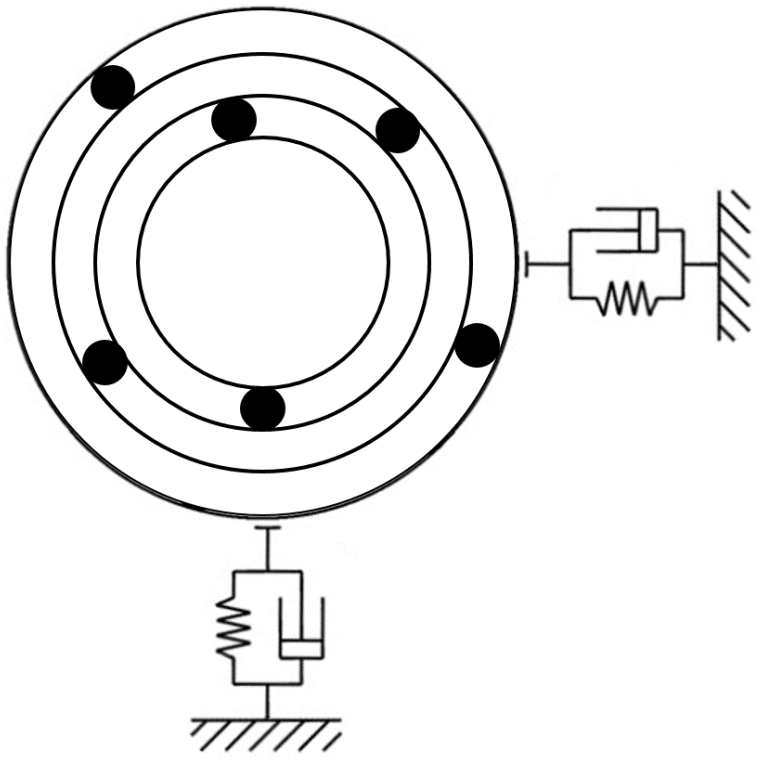

Figure 1.43: A ball-type passive balancing device with multiple tracks.

controlled transient response; the vibrations do not exceed the vibrations that would occur if the balancer was not present. It should be noted, however, that the balancing performance was slightly degraded with the introduction of springs and with the increased stiffness of the springs. Overall, this design ensured the passive balancer does not result in a transient response worse than the response without a passive balancer present.

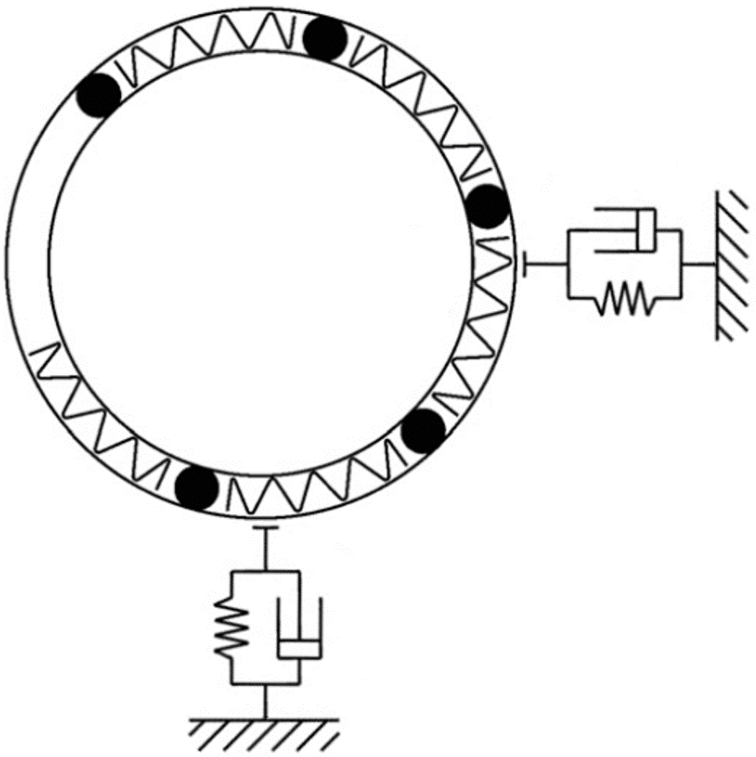

Figure 1.44: Ball-type passive balancer with spatial springs [33]

1.4.5 Studied Applications

There has been many studies dedicated to examining the effectiveness of passive balancing devices for various applications. In 1994, Conrad studied the use of passive balancing devices in washing machines [167]. Rajalungham and Rakheja first proposed using passive balancers in hand-held power tools for whirl suppression [168]. In 2001, several studies were conducted to characterize ball-type passive balancing devices in high-speed optic disk drivers [144, 145].

In 2010, DeSmidt investigated the effectiveness of passive balancers when a bladed-disk on a rotor was subject to a blade loss event [159]. In 2011, Urbiolo-Soto

et al. revisited the dynamics of Leblanc balancers in washing machines. In the same year, Majewski et al. studied the application of passive balancers in centrifuges [44]. Recently in 2014, Haidar and Palacios suggested the use of a passive balancing device to suppress vibration due to ice shedding events on bladed-disks [169].

1.5 Thesis Objectives

The goal of the study outlined in this thesis is to advance the knowledge of passive balancing devices by providing adequate means to predict their dynamic behavior and effectiveness. Providing the necessary tools is essential to the design and application of such systems.

The thesis first presents a comprehensive model that closely represents realistic systems where passive balancing could be applied. The equations of motions for a three dimensional system are derived using Lagrange's equation. The passive balancing device is assumed to be mounted on a flexible shaft. A flexible shaft has bending and twisting motions which allow for the non-planar teetering of shaft elements including the passive balancing device. Several boundary conditions for the shaft are allowed in the model. No assumption is made about the rotational velocity of the shaft. This allows for the study of the balancer dynamics when shaft speed is varying. Gravity is also considered and no restriction is placed on the shaft orientation with respect to the ground. Rotational inertia is included in this model.

The model is capable of including multiple unique balancers at different locations along the shaft with any number of balancing masses and tracks per balancer. An accurate method of modeling and numerically simulating rolling friction due to the ball/track interaction is provided. Balancing masses are also subject to viscous

damping and inelastic collisions. The model also allows for the placement of one or multiple dashpot/spring bearings anywhere along the shaft. Finally, a model of an n bladed or bladeless hub is included – blades are subject to steady aerodynamic drag and are allowed to bend elastically. Shaft mass imbalances are allowed to vary along the shaft and equations for two types of imbalance are provided. First, a point mass imbalance that remains in-plane, normal to the shaft, is possible. Second, partial or complete blade loss can be simulated as well as additional mass fixed to an elastic blade.

The model could be used to study any configuration consisting of a combination of a rotating shaft and mentioned shaft elements. There is no restriction or assumption made on the number or placement of elements along the flexible shaft. For example, the model could be used to predict the performance of a passive balancer in a multi-bladed-disk configuration such as a turbine engine compressor. The same tools provided here could be used to model and predict the performance of a passive balancing device on a helicopter hub.

In addition to providing the comprehensive model, experiments were conducted to validate it. A test rig was fabricated using a steel drive shaft rotated by an 2.1 horsepower electric motor. A detailed discussion of the experimental setup is provided in Chapter 3. Experimental data was collected using the test rig and a test matrix. Computer simulations were performed using the presented model to obtain predicted balancer performance. The experimental data was then analyzed and compared to predicted values. This was followed by a discussion, concluding remarks and recommendations for future work.

1.6 Thesis Overview

The thesis is distributed in the following chapters:

1.6.1 Chapter 2

A comprehensive, physics-based mathematical model of a passive balancing system is described. The equations of motion for a multi-mass-balancing system, including gravitational effects, coulomb friction, and viscous damping is presented.

1.6.2 Chapter 3

To validate the mathematical model, an experimental test rig is built. Detailed description of the design and fabrication of the experimental setup is given in this chapter. The test matrix and test procedures are also specified.

1.6.3 Chapter 4

The accuracy of the model predictions is examined in this chapter. Experiments were completed and the resulting experimental data is provided. The mathematical model was used to numerically predict the system response for each testing scenario. The experimental results and model predictions are compared and discussed.

1.6.4 Chapter 5

The final chapter outlines the conclusions that can be made in accordance with the findings of this research. Recommendations for future work are also suggested for increasing the effectiveness of the passive balancing device.

Chapter 2

Mathematical Model

To analyze the passive balancing system analytically, equations of motion are derived using multiple rectangular coordinate frames. This chapter describes the process of deriving the equations of motion for each element in the modeled system. The components in the model are the shaft, hub with blades, imbalance masses, damper and passive balancer (see Figure 2.1).

2.1 Kinematics

A set of Cartesian coordinate frames in this section. First, $\mathbf{x}_g$ is the Earth fixed inertial coordinate frame where gravity is in the $-\mathbf{x}_{g3}$ direction. The second reference frame is the $\mathbf{n}$ inertial frame which describes the tilt and orientation of the system with respect to the $\mathbf{x}_g$ frame. $\mathbf{a}$ is the shaft-fixed frame which rotates with the shaft. $\mathbf{n}_1$ and $\mathbf{a}_1$ always point in the longitudinal direction of the shaft. The $\mathbf{b}$ frame is a rotating frame fixed on the shaft. The $\mathbf{x}_i$ frame is a local frame to each blade. These coordinate frames are illustrated in Figure 2.1.

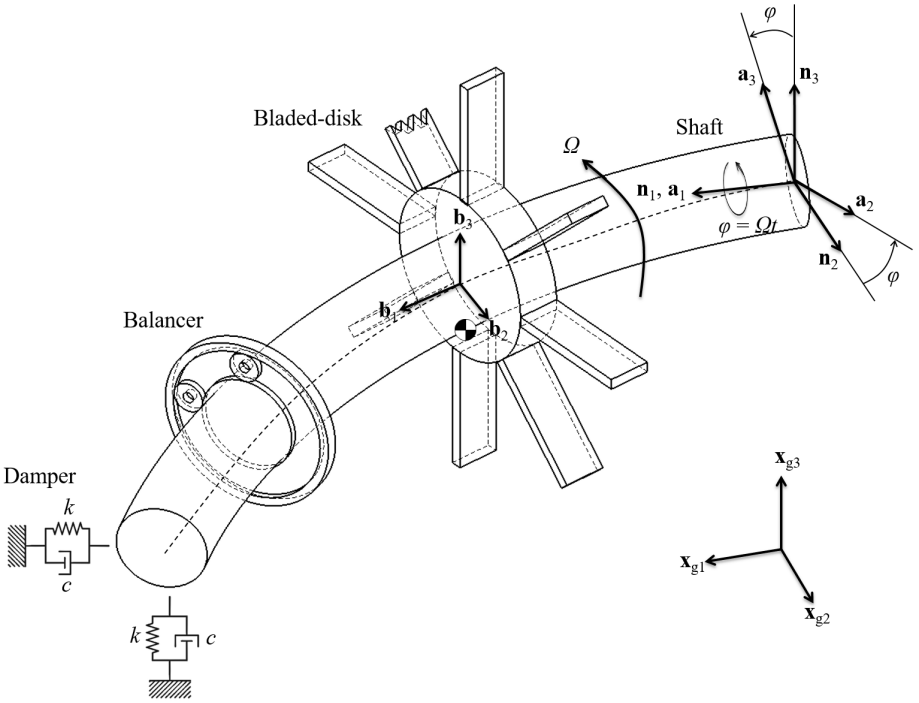

Figure 2.1: Overview of system model.

2.1.1 Transformation Matrices

This section will define a set of transformation matrices to facilitate the use of local coordinate frames for energy calculations. Equation (2.1) defines the relationship between the $\mathbf{x}_g$ and $\mathbf{n}$ coordinate frames through the transformation matrix, $[\mathbf{T_{xn}}]$.

$$\begin{Bmatrix} \mathbf{n}_1 \\ \mathbf{n}_2 \\ \mathbf{n}_3 \end{Bmatrix} = [\mathbf{T_{xn}}] \begin{Bmatrix} \mathbf{x}_{g1} \\ \mathbf{x}_{g2} \\ \mathbf{x}_{g3} \end{Bmatrix} \tag{2.1}$$

$[\mathbf{T_{xn}}]$ is expanded in equation (2.2) below:

$$[\mathbf{T_{xn}}] = \begin{bmatrix} \cos(p) & \sin(p) & 0 \\ -\sin(p) & \cos(p) & 0 \\ 0 & 0 & 1 \end{bmatrix} \begin{bmatrix} \cos(r) & 0 & -\sin(r) \\ 0 & 1 & 0 \\ \sin(r) & 0 & \cos(r) \end{bmatrix} \begin{bmatrix} 1 & 0 & 0 \\ 0 & \cos(h) & \sin(h) \\ 0 & -\sin(h) & \cos(h) \end{bmatrix} \quad (2.2)$$

Where p is the angle in radians that is rotated about $\mathbf{x}_{g3}$, r is the angle in radians that is rotated about $\mathbf{x}_{g2}$ and h is the angle in radians that is rotated about $\mathbf{x}_{g1}$ (see Figure 2.2). All frames used are compliant with the right-hand rule.

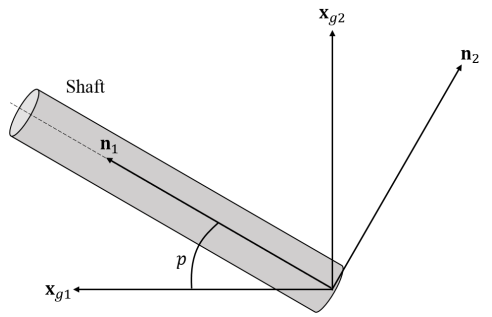

(a) Shaft rotation about $\mathbf{x}_{g3}$

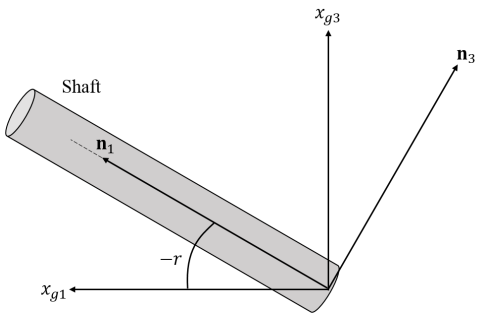

(b) Shaft rotation about $\mathbf{x}_{g2}$

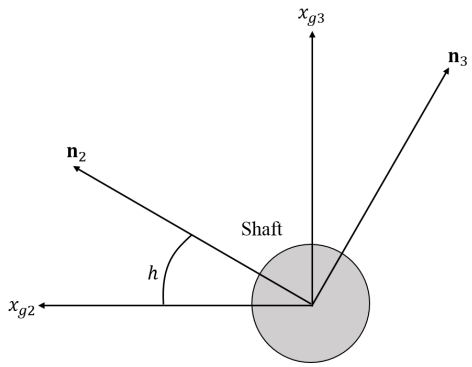

(c) Shaft rotation about $\mathbf{x}_{g1}$

Figure 2.2: Rotation angles to **n** coordinate frame.

Equation (2.3) defines the relationship between the **n** and **a** coordinate frames through the transformation matrix, $[\mathbf{T_{na}}]$.

$$\begin{Bmatrix} \mathbf{a}_1 \\ \mathbf{a}_2 \\ \mathbf{a}_3 \end{Bmatrix} = [\mathbf{T_{na}}] \begin{Bmatrix} \mathbf{n}_1 \\ \mathbf{n}_2 \\ \mathbf{n}_3 \end{Bmatrix} \tag{2.3}$$

Where $[\mathbf{T_{na}}]$ is in terms of ϕ as shown in equation (2.4).

$$[\mathbf{T_{na}}] = \begin{bmatrix} 1 & 0 & 0 \\ 0 & \cos(\phi) & \sin(\phi) \\ 0 & -\sin(\phi) & \cos(\phi) \end{bmatrix} \tag{2.4}$$

ϕ is the total shaft rotation. It is defined as the addition of the angular displacement of the angular velocity, Ω, and shaft twist, $\hat{\phi}$.

$$\phi = \int_0^t \Omega(t)\mathrm{d}t + \hat{\phi}(x,t) \tag{2.5}$$

Here, x is the distance along the shaft and t is time. Equation (2.6) defines the relationship between the **a** and **b** coordinate frames through the transformation matrix, $[\mathbf{T_{ab}}]$.

$$\begin{Bmatrix} \mathbf{b}_1 \\ \mathbf{b}_2 \\ \mathbf{b}_3 \end{Bmatrix} = [\mathbf{T_{ab}}] \begin{Bmatrix} \mathbf{a}_1 \\ \mathbf{a}_2 \\ \mathbf{a}_3 \end{Bmatrix} \tag{2.6}$$

$[\mathbf{T_{ab}}]$ is expanded in equation (2.7) below:

$$[\mathbf{T_{ab}}] = \begin{bmatrix} \cos(\gamma) & \sin(\gamma) & 0 \\ -\sin(\gamma) & \cos(\gamma) & 0 \\ 0 & 0 & 1 \end{bmatrix} \begin{bmatrix} \cos(\beta) & 0 & -\sin(\beta) \\ 0 & 1 & 0 \\ \sin(\beta) & 0 & \cos(\beta) \end{bmatrix} \tag{2.7}$$

Where γ is the angle in radians that is rotated about $\mathbf{a}_3$ and β is the angle in radians that is rotated about $\mathbf{a}_2$. γ and β are illustrated in Figure 2.3.

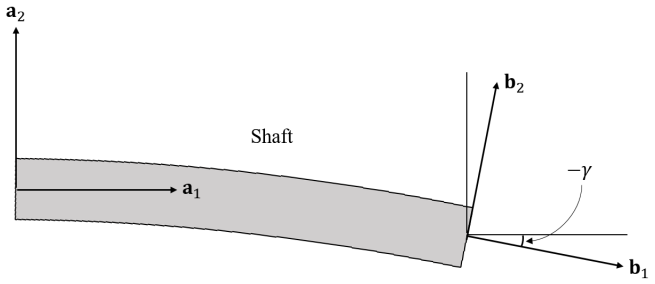

(a) **b** frame rotation about $\mathbf{a}_3$

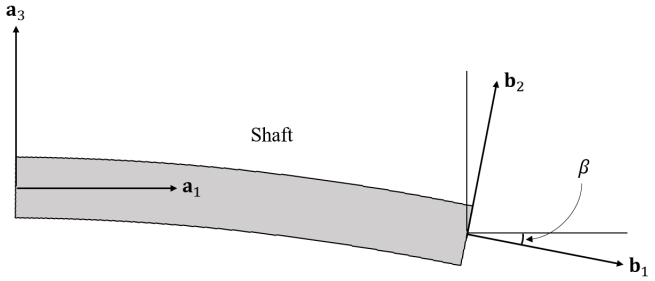

(b) **b** frame rotation about $\mathbf{a}_2$

Figure 2.3: Rotation angles from **a** to **b** coordinate frame.

In this model, only small deflections are considered which simplifies γ and β to:

$$\begin{aligned} \gamma &\approx v'(x,t) \\ \beta &\approx -w'(x,t) \end{aligned} \tag{2.8}$$

In addition, using the following small angle approximations,

$$\begin{aligned} \sin(\gamma) &\approx v'(x,t) \quad & \cos(\gamma) &\approx 1 - \tfrac{v'(x,t)^2}{2} \\ \sin(\beta) &\approx -w'(x,t) \quad & \cos(\beta) &\approx 1 - \tfrac{w'(x,t)^2}{2} \end{aligned} \tag{2.9}$$

Here, v is the shaft displacement along the $\mathbf{a}_2$ axis and w is the shaft displacement along the $\mathbf{a}_3$ axis. $[\mathbf{T_{ab}}]$ is rewritten in terms of v and w.

$$[\mathbf{T_{ab}}] = \begin{bmatrix} 1 - \frac{v'(x,t)^2}{2} & v'(x,t) & 0 \\ -v'(x,t) & 1 - \frac{v'(x,t)^2}{2} & 0 \\ 0 & 0 & 1 \end{bmatrix} \begin{bmatrix} 1 - \frac{w'(x,t)^2}{2} & 0 & w'(x,t) \\ 0 & 1 & 0 \\ -w'(x,t) & 0 & 1 - \frac{w'(x,t)^2}{2} \end{bmatrix} \tag{2.10}$$

Equation (2.11) defines the relationship between the $\mathbf{n}$ and $\mathbf{b}$ coordinate frames through the transformation matrix, $[\mathbf{T_{nb}}]$.

$$\begin{Bmatrix} \mathbf{b}_1 \\ \mathbf{b}_2 \\ \mathbf{b}_3 \end{Bmatrix} = \begin{bmatrix} \cos(\gamma) & \sin(\gamma) & 0 \\ -\sin(\gamma) & \cos(\gamma) & 0 \\ 0 & 0 & 1 \end{bmatrix} \begin{bmatrix} \cos(\beta) & 0 & -\sin(\beta) \\ 0 & 1 & 0 \\ \sin(\beta) & 0 & \cos(\beta) \end{bmatrix} [\mathbf{T_{na}}] \begin{Bmatrix} \mathbf{n}_1 \\ \mathbf{n}_2 \\ \mathbf{n}_3 \end{Bmatrix} \tag{2.11}$$

$$\begin{Bmatrix} \mathbf{b}_1 \\ \mathbf{b}_2 \\ \mathbf{b}_3 \end{Bmatrix} = [\mathbf{T_{nb}}] \begin{Bmatrix} \mathbf{n}_1 \\ \mathbf{n}_2 \\ \mathbf{n}_3 \end{Bmatrix} \tag{2.12}$$

Equation (2.13) shows that the transformation matrix, $[\mathbf{T_{nb}}]$, can be obtained from the combination of the transformation matrices $[\mathbf{T_{ab}}]$ and $[\mathbf{T_{na}}]$.

$$[\mathbf{T_{nb}}] = [\mathbf{T_{ab}}][\mathbf{T_{na}}] \tag{2.13}$$

The last transformation matrix is defined in Equation (2.14). It relates the $\mathbf{a}_i$ coordinate frame to the rotating **b** frame through the transformation matrix, $[\mathbf{T_{ba_i}}]$. $\mathbf{a}_i$ is the blade fixed frame at the root which rotates about the shaft.

$$\begin{Bmatrix} \mathbf{a}_{1i} \\ \mathbf{a}_{2i} \\ \mathbf{a}_{3i} \end{Bmatrix} = [\mathbf{T_{ba_i}}] \begin{Bmatrix} \mathbf{b}_1 \\ \mathbf{b}_2 \\ \mathbf{b}_3 \end{Bmatrix} \tag{2.14}$$

$$[\mathbf{T_{ba_i}}] = \begin{bmatrix} 1 & 0 & 0 \\ 0 & \cos(\psi_i) & \sin(\psi_i) \\ 0 & -\sin(\psi_i) & \cos(\psi_i) \end{bmatrix} \tag{2.15}$$

In equation (2.15), ψ_i is the individual blade azimuth angle in radians.

2.1.2 Rotating Frame Angular Velocity Vector

To factor in the rotational inertia, the angular velocity of the **b** frame is calculated. Starting with the **b** frame unit vectors and using the chain rule to differentiate with respect to time, the time rate of change of the **b** frame is obtained as shown in equation (2.17).

$$\begin{Bmatrix} \mathbf{b}_1 \\ \mathbf{b}_2 \\ \mathbf{b}_3 \end{Bmatrix} = [\mathbf{T_{nb}}] \begin{Bmatrix} \mathbf{n}_1 \\ \mathbf{n}_2 \\ \mathbf{n}_3 \end{Bmatrix} \tag{2.16}$$

$$\dot{\hat{\mathbf{b}}} = \frac{\partial}{\partial t}\begin{Bmatrix}\mathbf{b}_1\\ \mathbf{b}_2\\ \mathbf{b}_3\end{Bmatrix} = \frac{\partial}{\partial t}\left([\mathbf{T_{nb}}]\right)\begin{Bmatrix}\mathbf{n}_1\\ \mathbf{n}_2\\ \mathbf{n}_3\end{Bmatrix} + [\mathbf{T_{nb}}]\frac{\partial}{\partial t}\left(\begin{Bmatrix}\mathbf{n}_1\\ \mathbf{n}_2\\ \mathbf{n}_3\end{Bmatrix}\right) = \frac{\partial}{\partial t}\left([\mathbf{T_{nb}}]\right)\begin{Bmatrix}\mathbf{n}_1\\ \mathbf{n}_2\\ \mathbf{n}_3\end{Bmatrix} \quad (2.17)$$

$\dot{\hat{\mathbf{b}}}$ can be written in terms of $[\mathbf{T_{na}}]$ and $\mathbf{b}$.

$$\dot{\hat{\mathbf{b}}} = \frac{\partial}{\partial t}\left([\mathbf{T_{nb}}]\right)\left([\mathbf{T_{nb}}]\right)^{-1}\begin{Bmatrix}\mathbf{b}_1\\ \mathbf{b}_2\\ \mathbf{b}_3\end{Bmatrix} \quad (2.18)$$

Since $\mathbf{b}$ is a basis, the time rate of change of $\mathbf{b}$ is equal to the angular velocity of the frame with respect to the inertial frame crossed with the unit vectors of the frame as shown in equation (2.19).

$$\dot{\hat{\mathbf{b}}} = {}^{N}\omega^{B} \times [\mathbf{I}] \cdot \hat{\mathbf{b}} \quad (2.19)$$

${}^{N}\omega^{B}$ is the vector of the angular rates of the $\mathbf{b}$ frame with resepect to the Newtonian frame, $\mathbf{n}$. A skew-symmetric angular velocity tensor is introduced in equation (2.20) which produces equivalent results to the cross product operator in equation (2.19).

$$\frac{\partial}{\partial t}\left([\mathbf{T_{nb}}]\right)[\mathbf{T_{nb}}]^{-1}\begin{Bmatrix}\mathbf{b}_1\\ \mathbf{b}_2\\ \mathbf{b}_3\end{Bmatrix} = \begin{bmatrix}0 & -\omega_3 & \omega_2\\ \omega_3 & 0 & -\omega_1\\ -\omega_2 & \omega_1 & 0\end{bmatrix}\begin{Bmatrix}\mathbf{b}_1\\ \mathbf{b}_2\\ \mathbf{b}_3\end{Bmatrix} \quad (2.20)$$

Further simplifying the expression yields the relationship between the $\mathbf{b}$ frame

angular velocities to the transformation matrix, $[\mathbf{T_{nb}}]$ as shown in equation (2.21).

$$\frac{\partial}{\partial t}\left([\mathbf{T_{nb}}]\right)[\mathbf{T_{nb}}]^{-1} = \begin{bmatrix} 0 & -\omega_3 & \omega_2 \\ \omega_3 & 0 & -\omega_1 \\ -\omega_2 & \omega_1 & 0 \end{bmatrix} \tag{2.21}$$

The resulting **b** frame angular velocities, ω_B, are shown in equation (2.22).

$$\begin{Bmatrix} \omega_{B1} \\ \omega_{B2} \\ \omega_{B3} \end{Bmatrix} = \begin{Bmatrix} \omega_1 \\ \omega_2 \\ \omega_3 \end{Bmatrix} = \begin{Bmatrix} -\dot{w}'v' - \Omega\left(\frac{\left(v'^2-2\right)\left(w'^2-2\right)}{4}\right) \\ \frac{1}{2}\Omega v'\left(w'^2-2\right) - \frac{1}{2}\dot{w}'\left(v'^2-2\right) \\ \dot{v}' + \Omega w' \end{Bmatrix} \tag{2.22}$$

2.2 Shaft

The first component of the system is the drive shaft. The shaft translates rotation to all the components fixed to it. In this model, to investigate the effects of non-planar motion on passive balancing, the shaft is assumed to be flexible. The shaft is modeled as both a beam to predict deflection and a rod to predict twist. Small deflection and small twist are assumed allowing for the use Euler-Bernoulli beam theory.

The position vector locating the inertial axis of the shaft is defined in terms of blade deflections, v and w, in equation (2.23).

$$\mathbf{R}_{OC} = v(x,t)\mathbf{a}_2 + w(x,t)\mathbf{a}_3 \tag{2.23}$$

An illustration of vector $\mathbf{R}_{OC}$ is shown in Figure 2.4.

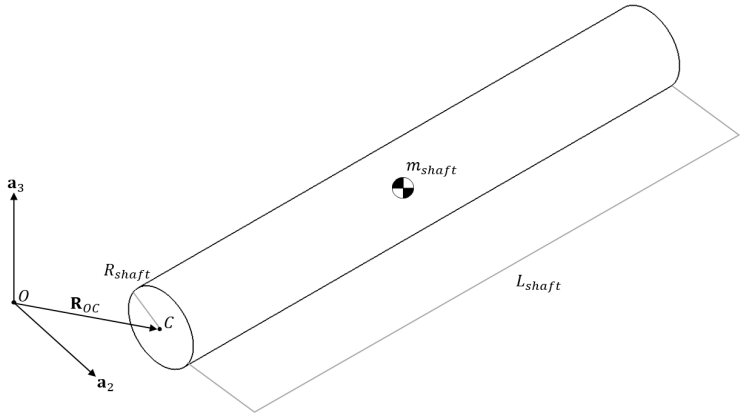

Figure 2.4: Shaft model.

The kinetic energy of the shaft is shown in equation (2.24):

$$\begin{aligned} T_{shaft} = \frac{1}{2}\int_0^{L_{shaft}} \{ & m_{shaft}\left(\dot{\mathbf{R}}_{OC}\cdot\dot{\mathbf{R}}_{OC}\right) \\ & + \left(J_{m_{shaft}}\omega_{B1}^2 + I_{m_{shaft}}\omega_{B2}^2 + I_{m_{shaft}}\omega_{B3}^2\right)\}\mathrm{d}x \end{aligned} \tag{2.24}$$

Where L_{shaft} is the shaft length and m_{shaft} is the shaft mass per unit length. $J_{m_{shaft}}$ is the shaft polar moment of inertia and $I_{m_{shaft}}$ is the shaft transverse moment of inertia. Equations (2.25) and (2.26) define $J_{m_{shaft}}$ and $I_{m_{shaft}}$.

$$J_{m_{shaft}} = \frac{m_{shaft}R_{shaft}^2}{2} \tag{2.25}$$

$$I_{m_{shaft}} = \frac{1}{12}m_{shaft}\left(3R_{shaft}^2 + L_{shaft}^2\right) \tag{2.26}$$

Here, R_{shaft} is the shaft radius. The potential energy of the shaft is shown in

equation (2.27).

$$\begin{aligned} U_{shaft} = \frac{1}{2}\int_0^{L_{shaft}} \{ & E_{shaft} I_{shaft} \left(\mathbf{R}''_{OC} \cdot \mathbf{R}''_{OC}\right) \\ & + G_{shaft} J_{shaft} (\hat{\phi}')^2 \\ & + 2 m_{shaft} \left(-\mathbf{F}_g \cdot \mathbf{R}_{OC}\right)\} \mathrm{d}x, \end{aligned} \tag{2.27}$$

where E_{shaft} is the shaft modulus of elasticity, I_{shaft} is the shaft second area moment of inertia, G_{shaft} is the shaft modulus of rigidity, J_{shaft} is the polar moment of area, and $\mathbf{F}_g$ is the gravitational body force.

Equation (2.28) demonstrates how the dot product of the second partial derivatives of $\mathbf{R}_{OC}$ with respect to x simplifies.

$$\mathbf{R}''_{OC} \cdot \mathbf{R}''_{OC} = v''^2 + w''^2 \tag{2.28}$$

I_{shaft} and J_{shaft} are geometric terms and for a circular cross-section shaft, they can be calculated using equations (2.29) and (2.30).

$$I_{shaft} = \frac{\pi}{4} R_{shaft}^4 \tag{2.29}$$

$$J_{shaft} = \frac{\pi}{2} R_{shaft}^4 \tag{2.30}$$

The gravitational body force, $\mathbf{F}_g$ is in terms of the gravitational constant, g, and the Earth-fixed inertial frame as shown in equation (2.31).

$$\mathbf{F}_g = -g\mathbf{x}_3 \tag{2.31}$$

Lastly, the Rayleigh dissipation energy of the shaft is displayed in equation (2.32) where ξ_{shaft} is the shaft structural damping coefficient.

$$\begin{aligned} D_{shaft} = \xi_{shaft} \int_0^{L_{shaft}} \{ & \frac{E_{shaft} I_{shaft}}{2} \left(\dot{\mathbf{R}}''_{OC} \cdot \dot{\mathbf{R}}''_{OC} \right) \\ & + \frac{G_{shaft} J_{shaft}}{2} \left(\dot{\phi}'^2 \right) \} \mathrm{d}x \end{aligned} \tag{2.32}$$

The energy equations will be used to construct the equations of motion through Lagrange's equations.

2.3 Hub

The second component that is considered in the model is a hub. A hub in this model is defined and a cylindrical body rigidly attached to the shaft at location L_{hub}. The kinetic energy of such hub is shown in equation (2.33). The rotary inertia of the hub is included in the kinetic energy term.

$$T_{hub} = \left[\frac{m_{hub}}{2} \left(\dot{\mathbf{R}}_{OC} \cdot \dot{\mathbf{R}}_{OC} \right) + \frac{1}{2} \left(J_{m_{hub}} \omega_{B1}^2 + I_{m_{hub}} \omega_{B2}^2 + I_{m_{hub}} \omega_{B3}^2 \right) \right]_{x=L_{hub}} \tag{2.33}$$

Here, $J_{m_{hub}}$ is the hub polar moment of inertia and $I_{m_{hub}}$ is the transverse moment of inertia. For a cylindrical hub, $J_{m_{hub}}$ and $I_{m_{hub}}$ can be calculated as shown in equations (2.34) and (2.35).

$$J_{m_{hub}} = \frac{m_{hub} R_{hub}^2}{2} \tag{2.34}$$

$$I_{m_{hub}} = \frac{1}{12} m_{hub} \left(3R_{hub}^2 + t_{hub}^2 \right) \tag{2.35}$$

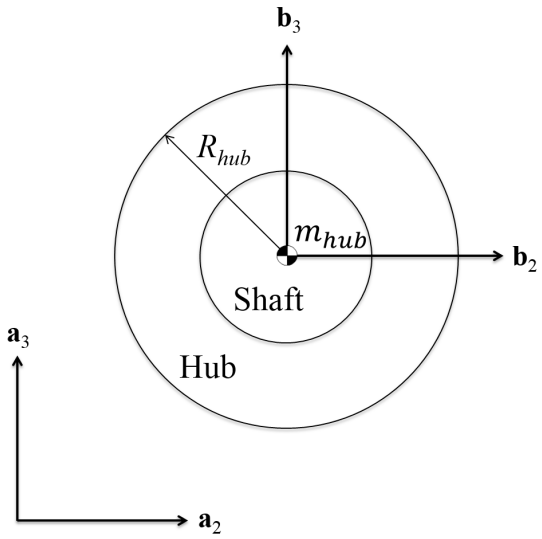

Figure 2.5: Hub model.

Where m_{hub} is the hub mass, R_{hub} is the hub radius and t_{hub} is the hub thickness. The hub potential energy is shown in equation (2.36). Since the hub is assumed to be rigid, the potential energy term has no strain energy. Instead, the only term in the potential energy of the hub expression is due to the gravitational body force, $\mathbf{F}_g$.

$$U_{hub} = \left[m_{hub}\left(-\mathbf{F}_g \cdot \mathbf{R}_{OC}\right)\right]_{x=L_{hub}} \tag{2.36}$$

2.4 Blades

The position vector locating a point P_i (shown in Figures 2.6 and 2.7) on the ith blade is noted in equation (2.37). The blades are located on a hub located at L_{hub} along the shaft length.

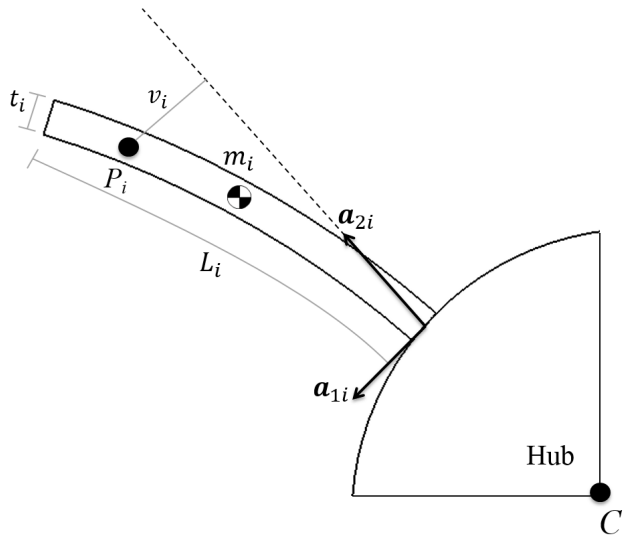

Figure 2.6: Attached blade model in $\mathbf{a}_{1i}$ and $\mathbf{a}_{2i}$ plane.

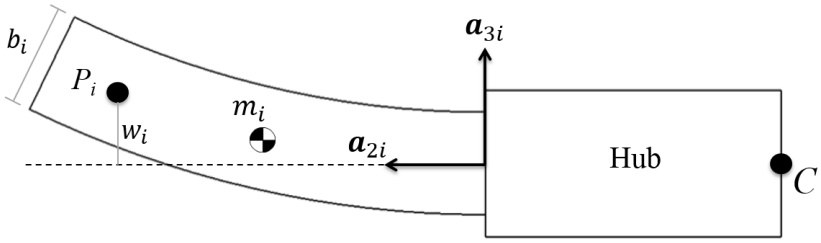

Figure 2.7: Attached blade model in $\mathbf{a}_{2i}$ and $\mathbf{a}_{3i}$ plane.

$$\mathbf{R}_{OP_i} = [\mathbf{R}_{OC} + \mathbf{R}_{CP_i}]_{x=L_{hub}} \tag{2.37}$$

In expanded form, R_{OP_i} becomes:

$$\begin{aligned}\mathbf{R}_{OP_i} = \mathbf{R}_{OC}|_{x=L_{hub}} + v_i(x_i,t)\mathbf{a}_{1i} + w_i(x_i,t)\mathbf{a}_{3i} \\ + [R_{hub} + x_i - \frac{1}{2}\int_0^{x_i}\left(w_i'(x_i,t)^2 + v_i'(x_i,t)^2\right)\mathrm{d}x_i]\mathbf{a}_{2i},\end{aligned} \tag{2.38}$$

where v_i is the ith blade deflection in the $\mathbf{a}_{1i}$ direction and w_i is the ith blade

deflection in the $\mathbf{a}_{2i}$ direction. x_i is the local length-wise coordinate of the ith blade. The kinetic energy of the blade is then defined by equation (2.39), where it is the sum of all blade kinetic energies. N_b is the number of blades attached to the hub.

$$T_{blade} = \left[\sum_{i=1}^{N_b} \frac{1}{2} \int_0^{L_i} m_{blade_i} \left(\dot{\mathbf{R}}_{OP_i} \cdot \dot{\mathbf{R}}_{OP_i} \right) \mathrm{d}x_i \right]_{x=L_{hub}} \tag{2.39}$$

The total blades potential energy is shown in equation (2.40). The sources of blade potential energy are the strain energy in due to deflection and the potential energy from the gravitational body force, $\mathbf{F}_g$.

$$\begin{aligned} U_{blade} = & \sum_{i=1}^{N_b} \int_0^{L_i} \frac{1}{2} E_{blade} I_{blade,3} w_i''(x_i,t)^2 \mathrm{d}x_i \\ & + \sum_{i=1}^{N_b} \int_0^{L_i} \frac{1}{2} E_{blade} I_{blade,1} v_i''(x_i,t)^2 \mathrm{d}x_i \\ & + \sum_{i=1}^{N_b} \int_0^{L_i} m_{blade_i} \left(-\mathbf{F}_g \cdot \mathbf{R}_{OP_i} \right) \mathrm{d}x_i \end{aligned} \tag{2.40}$$

Here, since the blade cross-section is assumed to be asymmetric, the second area moment of inertia varies between the cross-section axis. $I_{blade,1}$ is the blade second area moment of inertia about $\mathbf{a}_{1i}$. $I_{blade,3}$ is the blade second area moment of inertia about $\mathbf{a}_{3i}$. E_{blade} is the blade modulus of elasticity and m_{blade_i} is the blade mass per unit length. For a rectangular cross-section blade, $I_{blade,1}$ and $I_{blade,3}$ can be calculated as shown in equations (2.41) and (2.42).

$$I_{blade,1} = \frac{1}{12} b_i t_i^3 \tag{2.41}$$

$$I_{blade,3} = \frac{1}{12} t_i b_i^3, \tag{2.42}$$

where b_i is the ith blade width and t_i is the ith blade thickness. The Rayleigh dissipation energy of the blades is shown in equation (2.43).

$$\begin{aligned} D_{blade} = &\sum_{i=1}^{N_b} \frac{1}{2} \xi_{blade} E_{blade} I_{blade,3} \int_0^{L_i} \left(\dot{w}_i''(x_i,t)^2 \right) \mathrm{d}x_i \\ &+ \sum_{i=1}^{N_b} \frac{1}{2} \xi_{blade} E_{blade} I_{blade,1} \int_0^{L_i} \left(\dot{v}_i''(x_i,t)^2 \right) \mathrm{d}x_i \end{aligned} \tag{2.43}$$

Here, ξ_{blade} is the blade material damping coefficient. The virtual work, W_{blade}, for the blades is a product of the aerodynamic loads on their surfaces. The virtual work from aerodynamic loads on the blades is shown in equation (2.44) where a steady aerodynamic model is used.

$$\delta W_{blade} = -c_d \sum_{i=1}^{N_b} \int_0^{L_i} (v_{blade_i})^2 \delta u_{blade_i} \mathrm{d}x_i \tag{2.44}$$

v_{blade_i} is the local velocity component of the ith blade in the normal direction, u_{blade_i} is the local displacement of the ith blade in the normal direction and c_d is the effective blade drag coefficient per unit length. v_{blade_i} is defined in equation (2.45) and the expanded form is shown in equation (2.46).

$$v_{blade_i}(x_i,t) = \dot{\mathbf{R}}_{OP_i} \cdot \mathbf{a}_{3i} \tag{2.45}$$

$$\begin{aligned} v_{blade_i}(x_i,t) \cong &(\Omega v + \dot{w}) \cos(\psi_i) + (\Omega w - \dot{v}) \sin(\psi_i) \\ &+ (R_{hub} + x_i)(\dot{\hat{\phi}} + \Omega) + \dot{w}_i \end{aligned} \tag{2.46}$$

Similarly, v_{blade_i} is defined in equation (2.47) and the expanded form is shown in equation (2.48).

$$\delta u_{blade_i} = \delta \left[\mathbf{R}_{OP_i} - \mathbf{R}_{OP_i}|_{v=0,w=0,\hat{phi}=0,w_i=0} \cdot \mathbf{a}_{3i} \right] \tag{2.47}$$

$$\delta u_{blade_i} = \delta w \cos(\psi_i) - \delta v \sin(\psi_i) + (R_{hub} + x_i)\delta\hat{\phi} + \delta w_i \tag{2.48}$$

The blade aerodynamic drag coefficient per unit length is:

$$c_d = \frac{1}{2} C_d \rho_{air} b_i \tag{2.49}$$

Where C_d is the non-dimensional blade dragon coefficient and ρ_{air} is air density.

2.5 Imbalance Mass

The mass imbalance in the rotor could come from multiple sources. In essence, any asymmetric mass distribution will result in an unbalanced hub. In this section, the two types of imbalance masses are discussed. The first kind is a stationary "point mass" where there exists additional mass in the plane of the hub away from its center. The second kind is a blade-fixed mass which is point mass at a set location along a blade. The blade-fixed mass could be attributed to debris that can accumulate on the blade, to fabrication errors or blade damage. In the blade-fixed mass model, the mass moves according to the blades movement and vibration. Equations for both types of imbalance masses are derived.

2.5.1 Point Mass

For a point mass in the plane of a hub located at L_{hub} along the shaft length, the position vector, $\mathbf{R}_{OM}$, locating the mass is shown in equation (2.50).

$$\mathbf{R}_{OM} = \mathbf{R}_{OC}|_{x=L_{imb}} + R_{imb}\cos(\phi_m)\mathbf{b}_2 + R_{imb}\sin(\phi_m)\mathbf{b}_3 \tag{2.50}$$

$\mathbf{R}_{OM}$ depends on the radial location of the point mass, R_{imb}, and the azimuth angle of the mass, ϕ_m. After defining the point mass location vector, the kinetic energy for the point mass imbalance can be calculated. Equation (2.51) defines the kinetic energy. Since the mass is considered at a point, only ω_{B1} is considered for the rotary inertia of the mass.

$$T_{imb} = \frac{m_{imb}}{2}\left(\dot{\mathbf{R}}_{OM}\cdot\dot{\mathbf{R}}_{OM}\right) + \frac{m_{imb}}{2}\mathbf{R}_{OM}^2\omega_{B1}^2 \tag{2.51}$$

Here, m_{imb} is the mass of the point mass imbalance. The potential energy of the point mass is shown in equation (2.52) and it is a function of the gravitation body force, $\mathbf{F}_g$.

$$U_{imb} = m_{imb}\left(-\mathbf{F}_g\cdot\mathbf{R}_{OM}\right) \tag{2.52}$$

2.5.2 Blade-fixed Mass

The second type of mass imbalance considered in this research is imbalance due to mass where there is accretion or mass loss on a given blade. For a mass on the ith blade on a hub located at L_{hub} along the shaft length, the location vector, $\mathbf{R}_{OI_i}$, is

defined in equation (2.53).

$$\mathbf{R}_{OI_i} = [\mathbf{R}_{OC} + \mathbf{R}_{CP_i}]_{x=L_{hub}, x_i=L_i} \tag{2.53}$$

Equation (2.54) is the expanded form of $\mathbf{R}_{OI_i}$.

$$\begin{aligned}\mathbf{R}_{OI_i} = \mathbf{R}_{OC}|_{x=L_{hub}} &+ \{v_i(x_i,t)\mathbf{a}_{1i} + w_i(x_i,t)\mathbf{a}_{3i}\}_{x_i=L_i} \\ &+ \left\{[R_{hub} + x_i - \frac{1}{2}\int_0^{x_i}\left(w_i'(x_i,t)^2 + v_i'(x_i,t)^2\right)\mathrm{d}x_i]\mathbf{a}_{2i}\right\}_{x_i=L_i}\end{aligned} \tag{2.54}$$

After calculating the location vector, the kinetic energy of blade-fixed mass can be calculated. The kinetic energy of the mass is given in equation (2.55). Similarly to the point mass, only ω_{B1} is accounted for in the rotary inertia of this imbalance mass since it is considered only at a single point away from the center of the hub.

$$T_{bm} = \sum_{i=1}^{N_b} \frac{m_{bm}}{2}\left(\dot{\mathbf{R}}_{OI_i} \cdot \dot{\mathbf{R}}_{OI_i}\right) + \frac{m_{bm}}{2}\mathbf{R}_{OI_i}^2\omega_{B1}^2 \tag{2.55}$$

Here, m_{bm} is the mass of the imbalance that is attached to the blade. The potential energy of this mass is shown in equation (2.56) and it is a result of the gravitational body force, $\mathbf{F}_g$.

$$U_{bm} = \sum_{i=1}^{N_b} m_{bm}\left(-\mathbf{F}_g \cdot \mathbf{R}_{OI_i}\right) \tag{2.56}$$

2.6 Damper

The next component in the mathematical model is a damping component attached to the shaft at $L_{bearing_i}$ along the shaft length. Here, i represents the ith damper on the shaft. The model of the damper system is shown in figure 2.8.

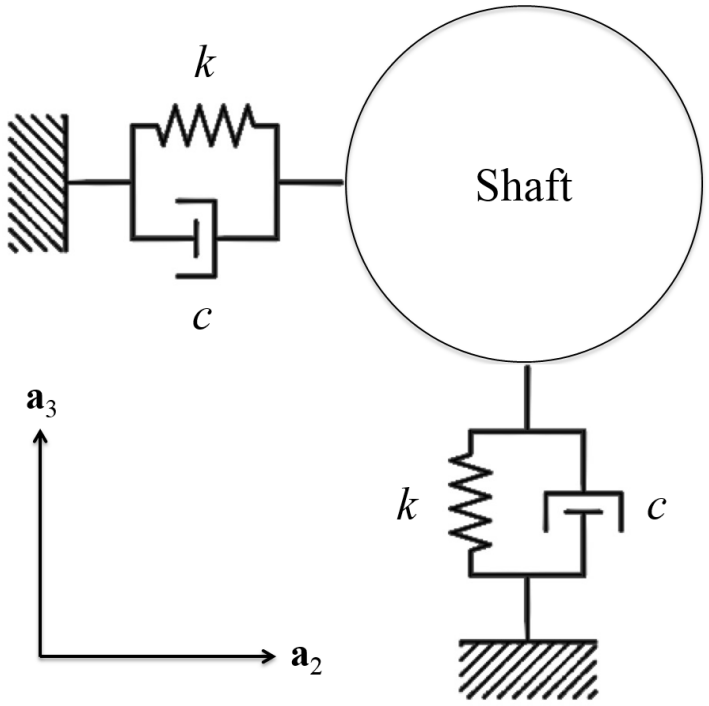

Figure 2.8: Damping system model.

Since the damper has no mass, the kinetic energy is equal to zero:

$$T_{bearing} = 0 \tag{2.57}$$

For the damper, some stiffness, k, is assumed which produces the following potential energy for the damper:

$$U_{bearing} = \frac{k}{2} \left[\mathbf{R}_{OC} \cdot \mathbf{R}_{OC} \right]_{x=L_{bearing_i}} \tag{2.58}$$

Where the dot product of $\mathbf{R}_{OC}$ can be simplified as shown in equation (2.59).

$$\mathbf{R}_{OC} \cdot \mathbf{R}_{OC} = v^2 + w^2 \tag{2.59}$$

The Rayleigh dissipation of the damper is a result of the damping coefficient, c, of the damper:

$$D_{bearing} = \frac{c}{2} \left[\dot{\mathbf{R}}_{OC} \cdot \dot{\mathbf{R}}_{OC} \right]_{x=L_{bearing_i}} \tag{2.60}$$

2.7 Passive Balancer

The equations of the passive balancer are derived for a single balancing mass with the index i. The balancer is located at L_{bmass} along the shaft length and the angle of the balancing mass, ϕ_{b_i}, is defined positive from the $\mathbf{b}_2$ axis (see Figure 2.9). R_b is the radial location of the balancing mass away from the hub center. Hence, the location vector of a balancing mass, $\mathbf{R}_{OB_i}$, is:

$$\begin{aligned} \mathbf{R}_{OB_i} = \left[\mathbf{R}_{OC} + \mathbf{R}_{CB_i} \right]_{x=L_{bmass}} = [v(x,t)\mathbf{a}_2 + w(x,t)\mathbf{a}_3 \\ + R_b \left(\cos[\phi_{b_i}(t)]\mathbf{b}_2 + \sin[\phi_{b_i}(t)]\mathbf{b}_3 \right)]_{x=L_{bmass}} \end{aligned} \tag{2.61}$$

The kinetic energy of the passive balancer is shown in equation (2.62). The summation of the energy terms extends to two balancing masses in the presented equations.

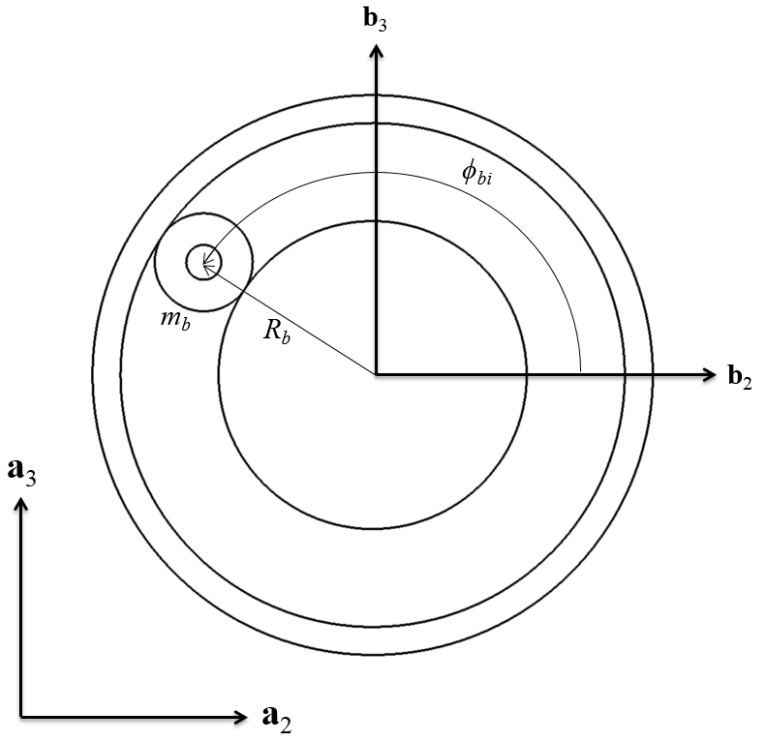

Figure 2.9: Passive balancer model.

$$T_{AB} = \sum_{i=1}^{2} \frac{m_{bmass}}{2} \left(\dot{\mathbf{R}}_{OB_i} \cdot \dot{\mathbf{R}}_{OB_i} \right) \tag{2.62}$$

Where m_{bmass} is the mass of the balancing mass. The potential energy of the balancing mass is shown in equation (2.63) and is a result of the gravitational body force, $\mathbf{F}_g$.

$$U_{AB} = \sum_{i=1}^{2} m_{bmass} \left(-\mathbf{F}_g \cdot \mathbf{R}_{OB_i} \right) \tag{2.63}$$

The Rayleigh dissipation energy of the balancer is calculated with the assumption of viscous damping due to the interaction between the balancing mass and the track. The viscous damping assumption results in the Rayleigh dissipation energy shown in equation (2.64).

$$D_{AB} = \sum_{i=1}^{2} \frac{c_{AB}}{2} R_b^2 \dot{\phi}_{b_i}^2 \tag{2.64}$$

However, this research suggests that the viscous damping model is inadequate alone in predicting the balancer mass movements. A better model should involve Coulomb friction. The accuracy of both models is comprehensively studied and compared to experimental results for validation. With Coulomb friction, the virtual work done by the balancer masses is:

$$\delta W_{AB} = -\left(\frac{\operatorname{sgn}(\dot{\phi}_{b_i}) \mu_{r,l} F_N}{r_b} \right) \delta\phi_{b_i}, \tag{2.65}$$

where $\mu_{r,l}$ is the rolling friction coefficient with dimension length, F_N is the normal force with respect to the ball/track contact surface and r_b is the balancing mass radius. The function, $\operatorname{sgn}(\dot{\phi}_{b_i})$, is defined as:

$$\operatorname{sgn}(\dot{\phi}_{b_i}) = \begin{cases} -1 & \text{if} \quad \dot{\phi}_{b_i} < 0 \\ 0 & \text{if} \quad \dot{\phi}_{b_i} = 0 \\ 1 & \text{if} \quad \dot{\phi}_{b_i} > 0 \end{cases} \tag{2.66}$$

The friction model is illustrated in Figure 2.10. F_f represents the rolling friction force due to the contact between the balancer ball and the track surfaces. The direction of the rolling friction depends on the motion of the balancing mass. A

criterion (shown in equation 2.67) was adopted to ensure that the friction force is never the driving force when ball velocity is zero. Here, F_b is the inertial loads that act on the balancing ball.

$$\text{if } \operatorname{sgn}(\dot{\phi}_{b_i}) \approx 0, \text{ then } \operatorname{sgn}(F_f) = -\operatorname{sgn}(F_b) \;\&\; |F_f| \leqslant |F_b| \tag{2.67}$$

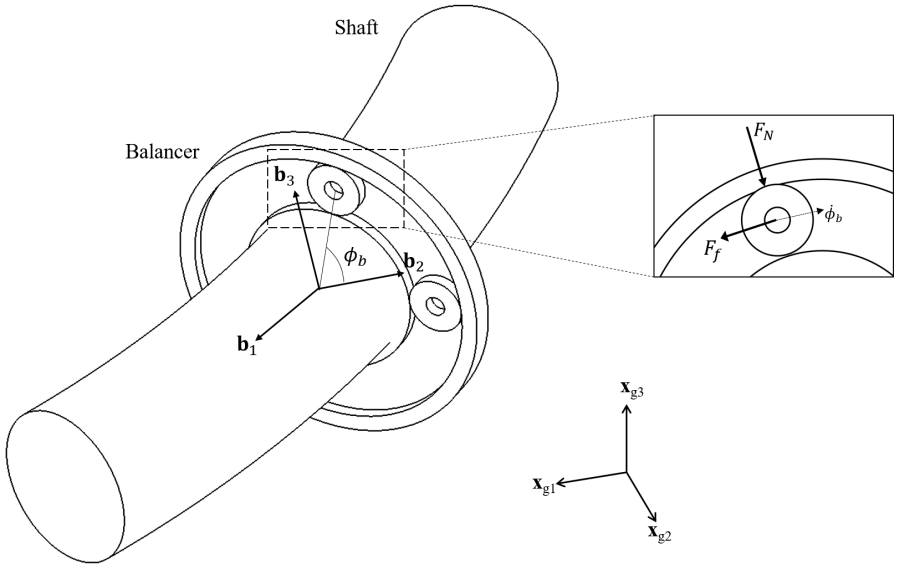

Figure 2.10: Schematic of passive balancer with friction.

At low shaft speeds, the normal force, F_N, is dominated by gravitational effects. While at high shaft speeds, the most significant contribution to the normal force is the centrifugal load. The total normal force used in this model is presented in equation 2.68 and combines both effects.

$$F_{N_i} = m_{bmass}\left[\left(\mathbf{F}_g \cdot \hat{\mathbf{R}}_{CB}\right) + R_b(\Omega + \dot{\phi}_{b_i})^2\right]_{x=L_{bmass}}, \tag{2.68}$$

where $\hat{\mathbf{R}}_{CB}$ is unit vector in the direction of $\mathbf{R}_{CB}$.

The collisions between the balancing masses were also considered in this model. Using an inelastic collision approximation, the post collision speeds were derived. For a coefficient of restitution, C_R, the angular velocities of the balancing masses after a collision is shown in equations 2.69 and 2.70.

$$\dot{\phi}_{1,new} = \frac{C_R m_{bmass,2}(\dot{\phi}_2 - \dot{\phi}_1) + m_{bmass,1}\dot{\phi}_1 + m_{bmass,2}\dot{\phi}_2}{m_{bmass,1} + m_{bmass,2}} \tag{2.69}$$

$$\dot{\phi}_{2,new} = \frac{C_R m_{bmass,1}(\dot{\phi}_1 - \dot{\phi}_2) + m_{bmass,1}\dot{\phi}_1 + m_{bmass,2}\dot{\phi}_2}{m_{bmass,1} + m_{bmass,2}} \tag{2.70}$$

2.8 System Discretization

To obtain the equations of motion for the system, elastic deflections and twists are approximated by an assumed modal expansion. The shaft transverse displacements, v and w are approximated as shown in equations (2.71) and (2.72).

$$v(x,t) = \sum_{i=1}^{N_m} \Theta_i(x)\eta_{v_i}(t) \tag{2.71}$$

$$w(x,t) = \sum_{i=1}^{N_m} \Theta_i(x)\eta_{w_i}(t) \tag{2.72}$$

Here, $\Theta_i(x)$ is the ith elastic mode shape for beam bending. η_{v_i} and η_{w_i} are the corresponding modal coordinates. For the system tested in this research, fixed-pinned boundary conditions are used for the shaft bending. The bending mode shapes and their calculation are provided in Appendix 1.1.3.

For shaft twist, $\hat{\phi}$, the approximation is shown in equation (2.73).

$$\hat{\phi}(x,t) = \sum_{i=1}^{N_m} \Phi_i(x)\eta_{\phi_i}(t) \tag{2.73}$$

Where $\Phi_i(x)$ is the ith elastic torsional mode shape and η_{ϕ_i} is the ith modal coordinate. For the system used in this research, cantilever or fixed-free boundary conditions were used for the shaft torsional mode shapes. The mode shapes in this case are provided in Appendix 1.2.1.

For the blade deflections, the ith blade deflections, v_i and w_i, are approximated by equations (2.74) and (2.75).

$$v_i(x_i,t) = \sum_{j=1}^{N_m} \Psi_{ij}(x_i)\eta_{v_ij}(t) \tag{2.74}$$

$$w_i(x_i,t) = \sum_{j=1}^{N_m} \Psi_{ij}(x_i)\eta_{w_ij}(t) \tag{2.75}$$

$\Psi_{ij}(x_i)$ is the jth elastic bending mode shape of the ith blade. η_{v_ij} and η_{w_ij} are the corresponding modal coordinates for the ith blade. The mode shapes for the blades are provided in Appendix 1.1.1 and the boundary conditions are assumed to be cantilever or fixed-free.

2.9 Total Energy

The total kinetic energy of the system is:

$$T = T_{shaft} + T_{hub} + T_{blade} + T_{bearing} + T_{AB} + T_{ice} + T_{imb} \tag{2.76}$$

The total potential energy of the system is:

$$U = U_{shaft} + U_{hub} + U_{blade} + U_{AB} + U_{bearing} + +U_{ice} + U_{imb} \tag{2.77}$$

The total Rayleigh dissipation energy of the system is:

$$D = D_{shaft} + D_{bearing} + D_{blade} + D_{AB} \tag{2.78}$$

The total virtual work of the system is:

$$\delta W = \delta W_{AB} + \delta W_{blade} = \mathbf{Q}^{\mathrm{T}} \delta \mathbf{q} \tag{2.79}$$

Where $\mathbf{Q}$ is the generalized force vector and $\mathbf{q}$ is the generalized coordinate vector.

2.10 Degrees of Freedom

For a system consisting of a shaft with N_m modes for 2 dimensional deflection and twist, N_b blades with $N_{m,b}$ modes for 2 dimensional deflection, and N_{AB} balancers with N_{bal} balancer masses, the number of degrees of freedom, N, is:

$$N = 3N_m + 2N_{m,b}N_b + N_{AB}N_{bal} \tag{2.80}$$

The $N \times 1$ generalized coordinate vector, $\mathbf{q}$, is then defined as:

$$\mathbf{q} = \begin{Bmatrix} \mathbf{q}_{shaft}^T & \mathbf{q}_{blade}^T & \mathbf{q}_{AB}^T \end{Bmatrix}^T \tag{2.81}$$

Where $\mathbf{q}_{shaft}$, the $3N_m \times 1$ shaft generalize coordinate vector, is defined in equation (2.82).

$$\mathbf{q}_{shaft} = \left\{ \boldsymbol{\eta_v}^T \quad \boldsymbol{\eta_w}^T \quad \boldsymbol{\eta_\phi}^T \right\}^T \tag{2.82}$$

$\boldsymbol{\eta_v}$, $\boldsymbol{\eta_w}$ and $\boldsymbol{\eta_\phi}$ are the model coordinate vectors for shaft bending in the $\mathbf{a}_2$ direction, shaft bending in the $\mathbf{a}_3$ direction and shaft twist about the $\mathbf{a}_1$ direction respectively. $\mathbf{q}_{blade}$, the $2N_{m,b}N_b \times 1$ shaft generalize coordinate vector, is defined in equation (2.83).

$$\mathbf{q}_{blade} = \left\{ \boldsymbol{\eta_{v1}}^T \quad \boldsymbol{\eta_{v2}}^T \quad ... \quad \boldsymbol{\eta_{vN_b}}^T \quad \boldsymbol{\eta_{w1}}^T \quad \boldsymbol{\eta_{w2}}^T \quad ... \quad \boldsymbol{\eta_{wN_b}}^T \right\}^T \tag{2.83}$$

Here, $\boldsymbol{\eta_{vi}}$ and $\boldsymbol{\eta_{wi}}$ are the model coordinate vectors for ith blade bending in the $\mathbf{a}_{i1}$ direction and ith blade bending in the $\mathbf{a}_{i3}$ direction respectively. $\mathbf{q}_{AB}$, the $N_{AB}N_{bal} \times 1$ shaft generalize coordinate vector, is defined in equation (2.84).

$$\mathbf{q}_{AB} = \left\{ \boldsymbol{\phi_{b1}} \quad \boldsymbol{\phi_{b2}} \quad ... \quad \boldsymbol{\phi_{bN_{AB}}} \right\}^T \tag{2.84}$$

Where ϕ_{bi} is the ith balancer mass location in the balancer track.

2.11 Equations of Motion

Having computed the kinetic, potential, Rayleigh dissipation energy along with the generalized force vector, the system equations of motion can be derived using Lagrange's equation:

$$\frac{\mathrm{d}}{\mathrm{d}t}\left[\frac{\partial T}{\partial \dot{\mathbf{q}}}\right] - \frac{\partial T}{\partial \mathbf{q}} + \frac{\partial U}{\partial \mathbf{q}} + \frac{\partial D}{\partial \dot{\mathbf{q}}} = \mathbf{Q} \tag{2.85}$$

Here, T is the total kinetic energy in the system. U is the total potential energy. D is the total Rayleigh dissipation energy and $\mathbf{Q}$ is the generalized force vector. $\mathbf{q}$ is the generalized coordinate vector and $\dot{\mathbf{q}}$ is the time derivative of the $\mathbf{q}$.

The resultant equations from equation (2.85) are placed into standard matrix form shown in equation (2.86). The system response is obtained using those equations of motion through a fourth order Runge-Kutta algorithm in a MATLAB® environment.

$$\mathbf{M}\ddot{q} + \mathbf{C}\dot{q} + \mathbf{K}q = \mathbf{F} \tag{2.86}$$

Where $\mathbf{M}$ is the system mass matrix, $\mathbf{C}$ is the system damping matrix, $\mathbf{K}$ is the system stiffness matrix and $\mathbf{F}$ is the system force vector.

Chapter 3

Experimental Testing of an Imbalanced Rotor with Passive Balancing

A test rig was developed and fabricated to test the effectiveness of a passive balancing device in suppressing rotor vibrations. This chapter describes the experimental configuration and outlines the different components of the test rig. The properties of the components forming the system are also provided. All parameters given were experimentally determined, and the procedures conducted to find these parameters are included in the section of each component. Finally, a test matrix for the main experiments is presented.

3.1 Test Rig

The experiment is comprised of a flexible 1566 steel shaft driven by a 2.1 horse power motor. The shaft is supported by fixed bearings to simulate fixed boundary

conditions. An imbalanced system along with a passive balancing device were mounted on the shaft. The imbalance system is a bladed-disk with attached eccentric mass. The passive balancer is a concentric track with two freely rotating masses. Additional damping was introduced into the system with a ground-fixed damper bearing.

Vibration amplitudes were measured using an optical displacement sensor. The motion of each balancing mass on the balancer track was captured using a high speed camera. To capture the motion at speeds up to 2200 RPM, video was recorded at 2000 frames per second. A schematic of the experimental setup is shown in Figure 3.1. Here, the location of each element along the shaft is listed. A photograph of the test rig can be seen in Figure 3.2. The following sections describe each component in detail and provide their relevant properties.

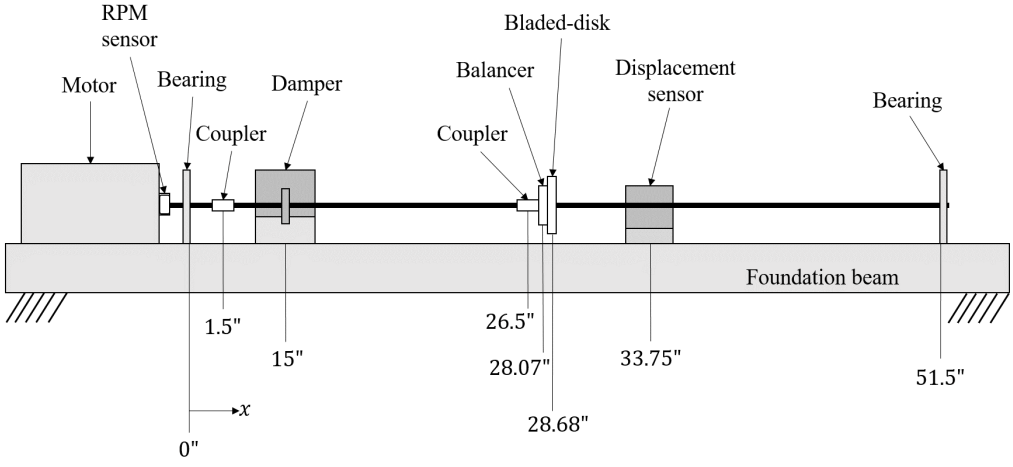

Figure 3.1: Schematic of experimental setup.

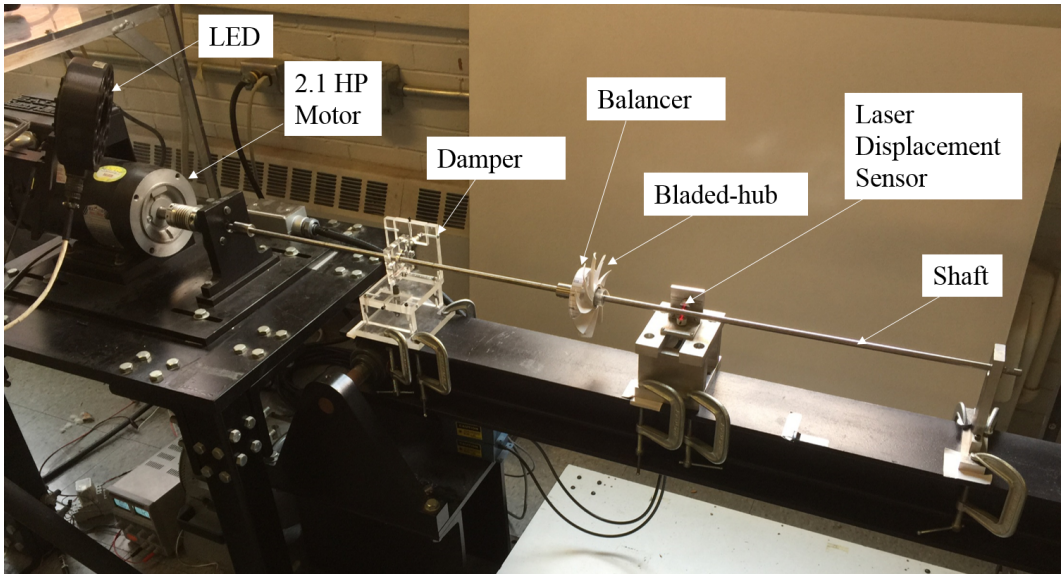

Figure 3.2: Photograph of experimental setup.

3.1.1 Shaft

The test rig includes a rotating shaft made of 1566 steel. Other than measurement devices, all other components in the experiment are in contact with the shaft. Properties of the shaft are listed in Table 3.1.

Table 3.1: Shaft properties.

Material	1566 Steel
Radius	$9.525 \times 10^{-3}\ m$
Density	$7779.43\ kg/m^3$
Length	$1.308\ m$
Modulus of elasticity	$179.78\ GPa$
Structural damping coefficient	$7.5 \times 10^{-5}\ s$

To determine the shaft modulus of elasticity, an experiment was performed. A schematic of the experiment is shown in Figure 3.3 and a photograph of the experiment is shown in Figure 3.4. A shaft, composed of the same material as

the one used in the test rig, was held at the root by fixed bearings to simulate cantilever suspension. Then, weights were added on the free end. The displacement at a specified location along the shaft was measured for varying tip loads.

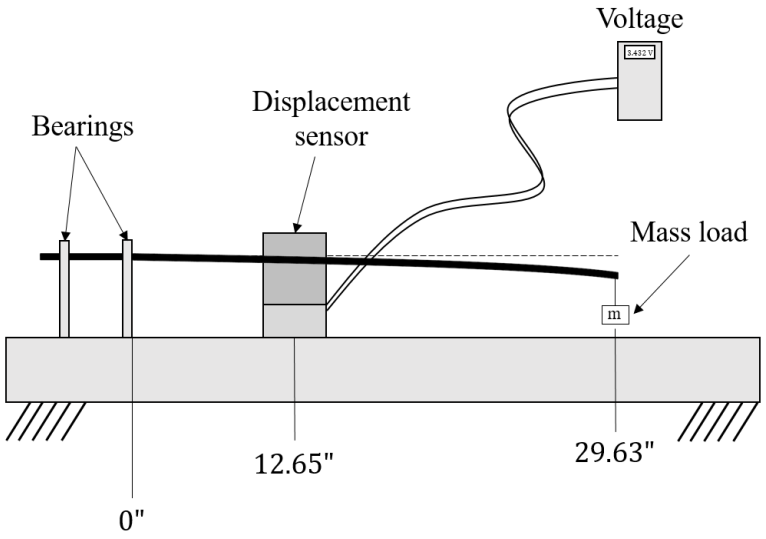

Figure 3.3: Schematic of the experimental setup for determining the shaft stiffness modulus.

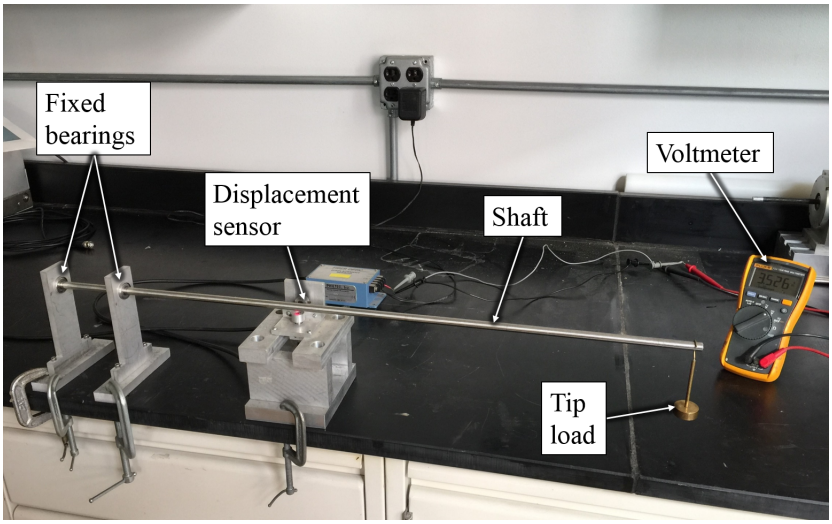

Figure 3.4: Experimental setup for determining the shaft stiffness modulus.

The measured shaft displacements for the different tip loads are plotted in Figure 3.5.

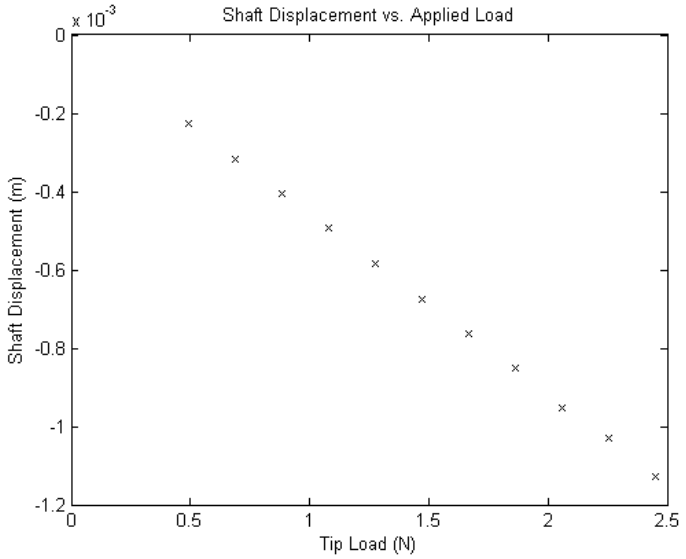

Figure 3.5: Experimentally measured shaft displacement under different tip loadings.

From the measured displacements and known loads, the modulus of elasticity was derived using Euler-Bernoulli beam theory. For a cantilever beam, the formula relating the modulus of elasticity to bending deflection is:

$$y(x) = \frac{Wx^2}{6EI}(3L - x), \tag{3.1}$$

where y is the beam deflection, W is the applied load, x is the distance along the beam from the root, E is the modulus of elasticity, I is the second moment of area, and L is the shaft length. The resulting calculations of the modulus of elasticity for each data point are plotted in Figure 3.6.

In Figure 3.6, the $\times$ markings represent the experimental modulus of elasticity while the line is the average of all the experimental values. The experimental mean

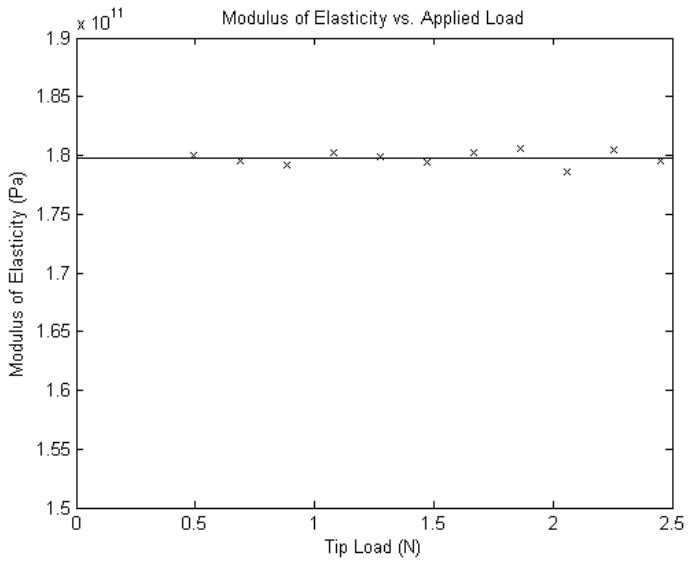

Figure 3.6: Shaft modulus of elasticity based on experimental measurements.

modulus of elasticity is found to be 179.78 GPa with a standard deviation of 3.4%.

The shaft structural damping was also measured experimentally. The free decay response was captured with an optical displacement sensor. A logarithmic decay curve was fitted to the response to determine the critical damping ratio, ζ. Multiple responses were captured and are shown in Figures 3.7–3.9. The black line denotes the fitted logarithmic decay curve. The average experimental critical damping ratio was found to be 0.33%.

To achieve the same critical damping ratio, the shaft structural damping factor was set to 7.5×10^{-5} s. The simulated free decay response of the shaft is shown in Figure 3.10. As shown, the fitted logarithmic decay curve demonstrates a matching critical damping ratio between the experiment and model.

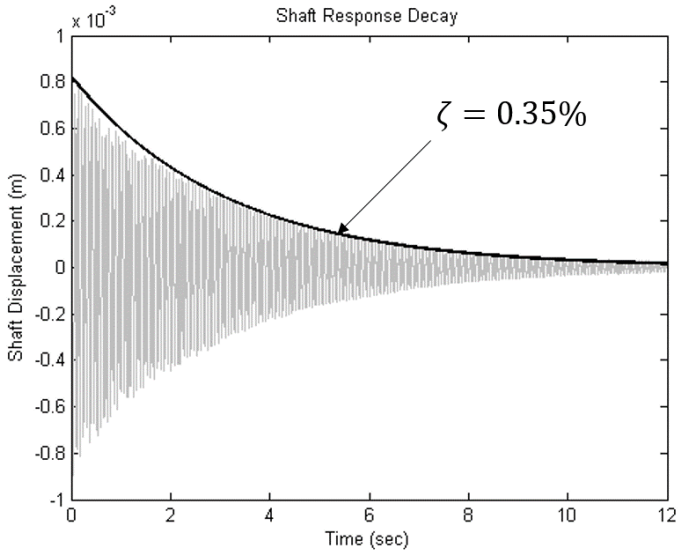

Figure 3.7: Free decay response of shaft without additional damping (run 1).

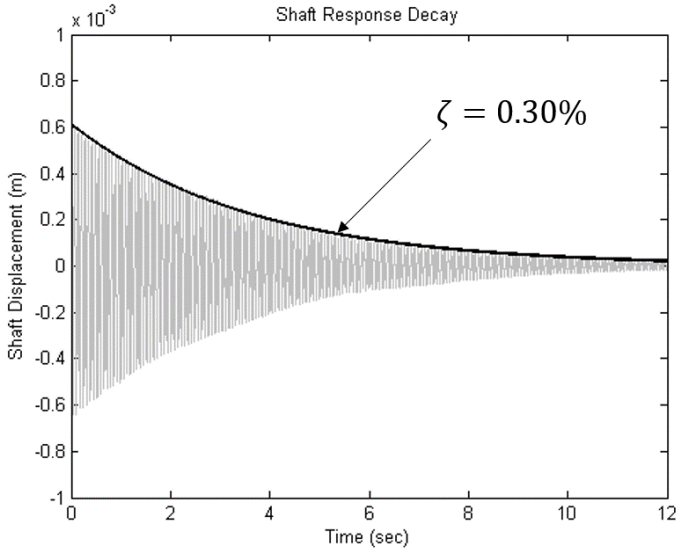

Figure 3.8: Free decay response of shaft without additional damping (run 2).

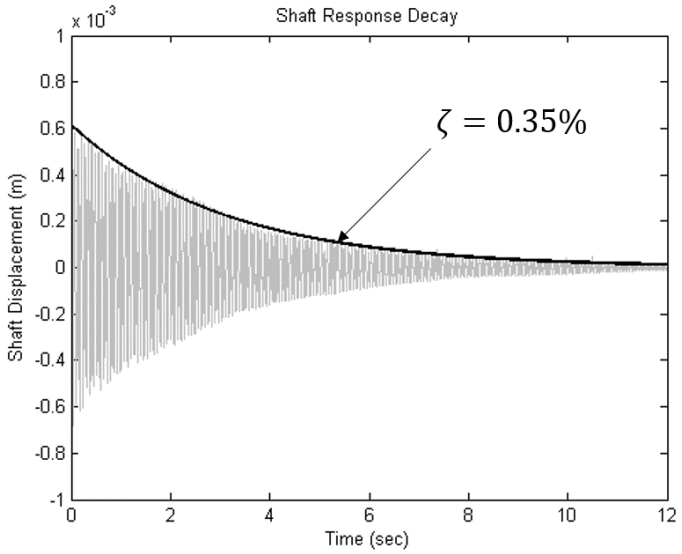

Figure 3.9: Free decay response of shaft without additional damping (run 3).

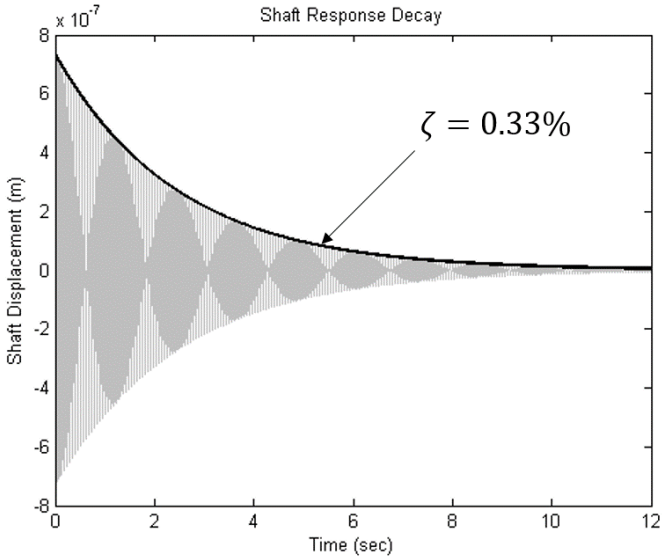

Figure 3.10: Simulated free decay response of shaft without additional damping.

3.1.2 Bearings

Two types of bearings were used in the test rig. The first type simulates a fixed boundary condition and is shown in Figure 3.11. This bearing is fixed to the foundation beam and for the purposes of the analysis, displacement of the shaft at this type of bearing is equal to zero (perfect fixed condition assumed).

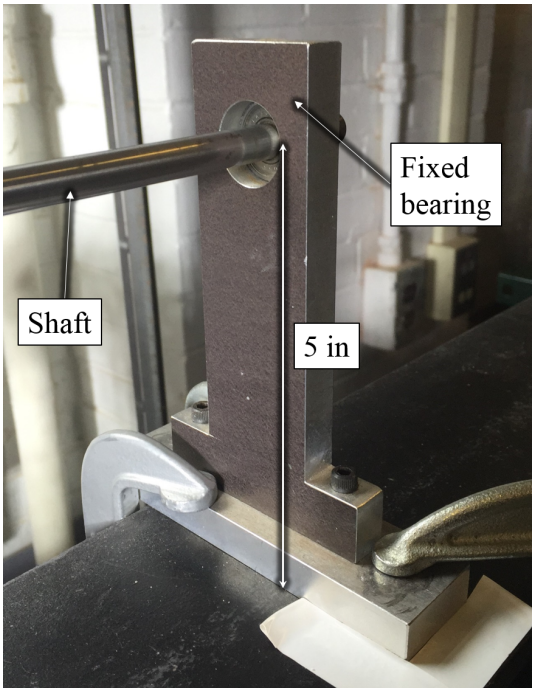

Figure 3.11: Photograph of fixed bearing.

The second type of bearing is the damper bearing. This bearing provides additional damping to the shaft as is typically the case in practical applications. A CAD model of the damper bearing is illustrated in Figure 3.12 and a photograph of the damper on the test rig is shown in Figure 3.13. The damper bearing consists of dual viscous dampers that are normal to the shaft. The dampers dissipate energy from the transverse vibrations of the shaft. Unlike the fixed bearing, this bearing does not restrict the motion of the shaft.

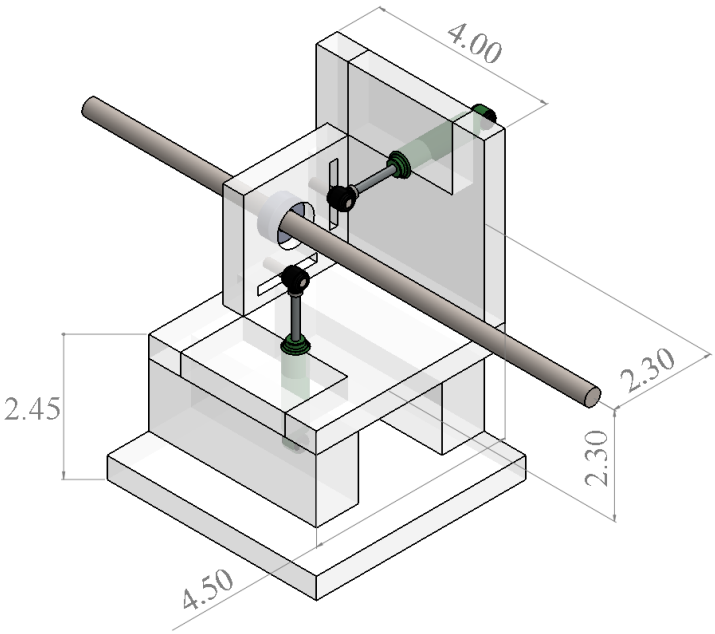

Figure 3.12: CAD model of damper bearing (inches).

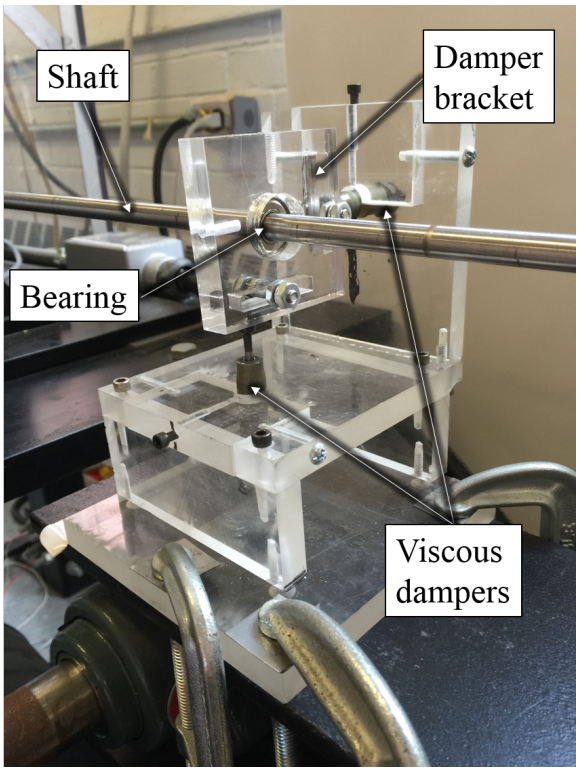

Figure 3.13: Photograph of damper bearing.

To determine the damping coefficients of the viscous dampers, an experiment was performed to study the free decay of a system with the damper bearing attached. The same system (Figures 3.7–3.9) was used, but for this experiment, the damper bearing was added. Several runs were completed and the free decay responses are shown in Figures 3.14–3.16). The experimental average critical damping ratio was found to be 9.67% with a standard deviation of 0.57% when the damper bearing was attached to the shaft.

To achieve the same critical damping ratio when the damper bearing was attached, the viscous damping coefficient was set to 23.0 kg/s. The simulated free decay response of the shaft with the damper bearing is shown in Figure 3.17. As shown, the critical damping ratio from the model matches the experimental value.

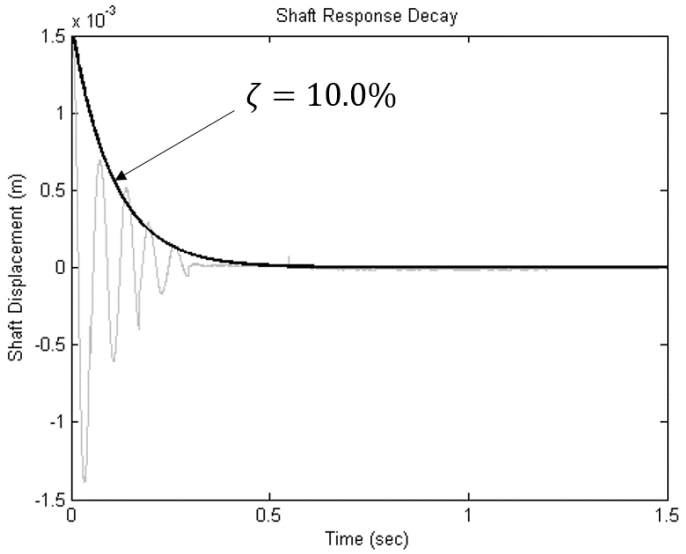

Figure 3.14: Free decay response of shaft with damper bearing (run 1).

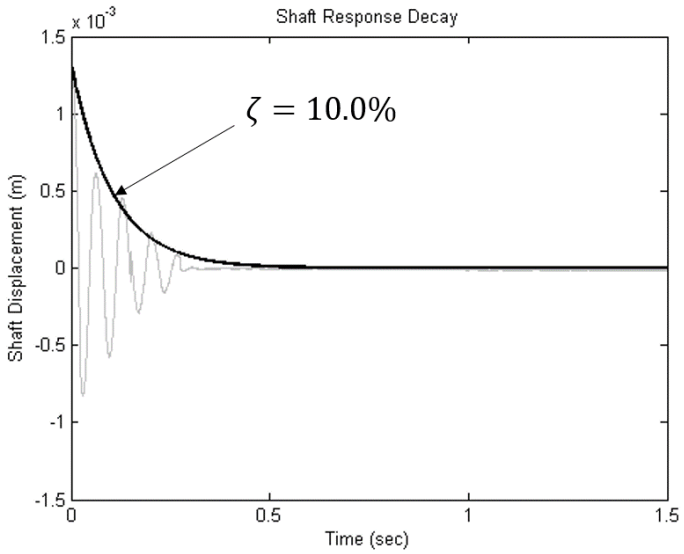

Figure 3.15: Free decay response of shaft with damper bearing (run 2).

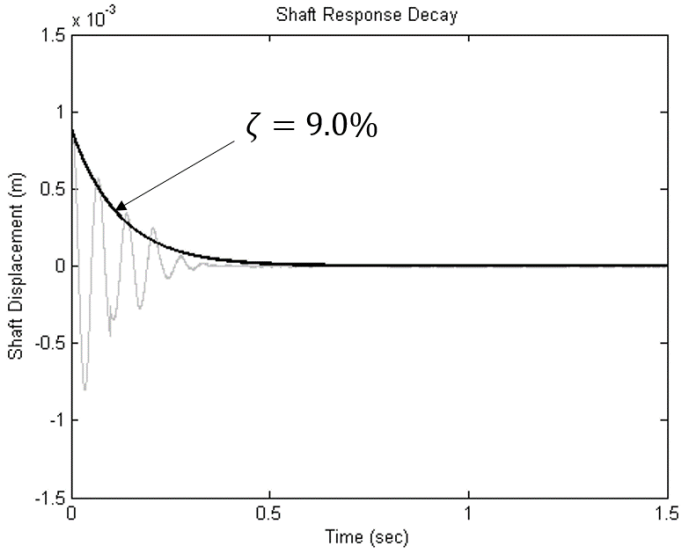

Figure 3.16: Free decay response of shaft with damper bearing (run 3).

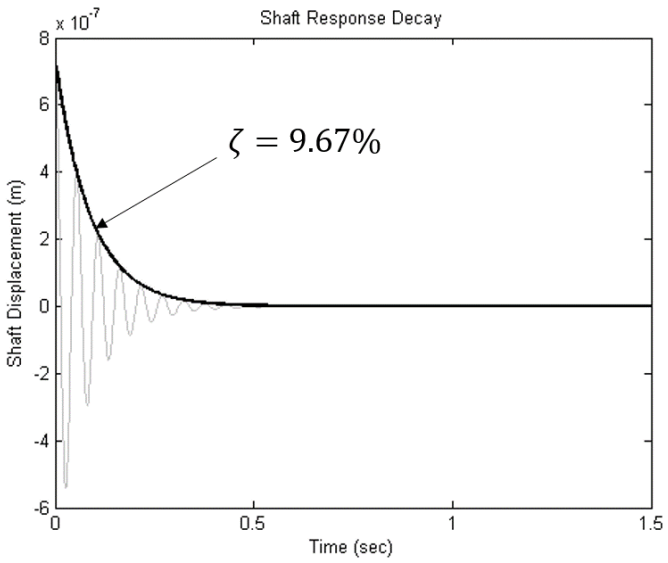

Figure 3.17: Simulated free decay response of shaft with damper bearing.

3.1.3 Passive Balancer

The passive balancer is a circular track designed to be attached in the vicinity to the imbalanced hub. In the experiments conducted in this research, two balancing masses are allowed to freely rotate concentrically about the geometric axis of the shaft. Properties of the passive balancer are listed in Tables 3.2 and 3.3.

Table 3.2: Balancer properties.

Material	Acrylic
Effective Radius	0.0305 m
Density	1916.70 kg/m^3
Thickness	16.11 mm
Location along shaft	0.713 m

The geometry of the passive balancing device is provided in Figure 3.18 and a photograph of the balancer is shown in Figure 3.19. Note that the angular

Table 3.3: Balancing mass properties.

Mass	$9.15 \times 10^{-3}\ kg$
Radius	$2.413 \times 10^{-2}\ m$
Mass radius	$1.016 \times 10^{-2}\ m$
Rolling friction coefficient	Varies
Coefficient of restitution	0.589

scale around the balancer is used to measure the location of the balancing masses circumferentially. The shape and size of the balancer was defined by the requirement to suppress vibrations due to imbalances below 10 grams and located 2 inches from the center of the shaft.

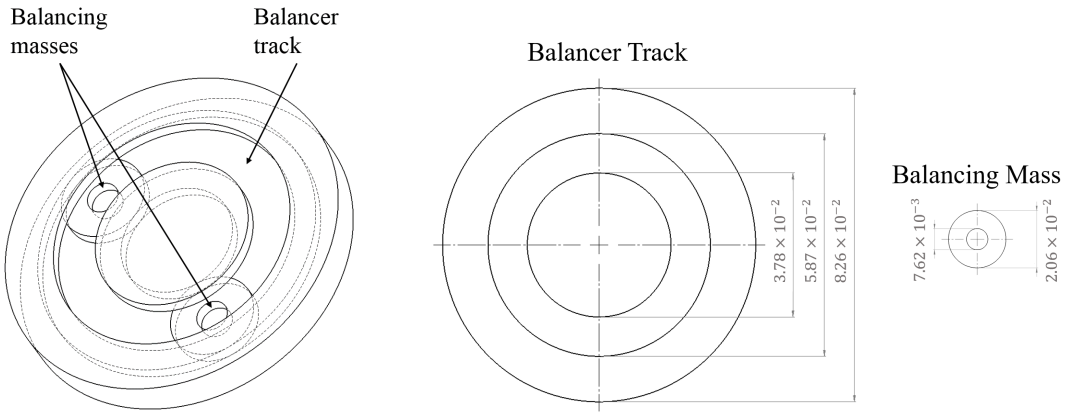

(a) CAD model of balancing device. (b) Dimensions of passive balancer and balancing mass (meters).

Figure 3.18: Schematics of passive balancer device.

Given that centrifugal loads are proportional to $mr\Omega^2$, the maximum imbalance arm that the dual balancer shown here can counter is equal to 2.01×10^{-4} m-kg. For example, an imbalance located 0.02m from the hub center could be at most $2.0208 \times 10^{-4}/0.02$kg, or 11g, for 100% counter balancing. A graphical representation of this is shown in Figure 3.20.

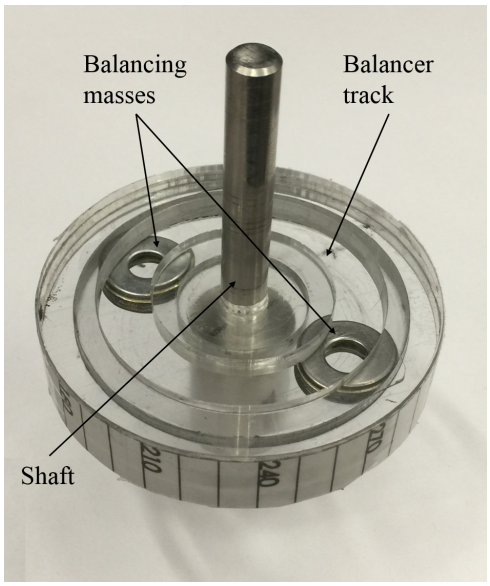

(a) Photograph of passive balancing device used in experiments.

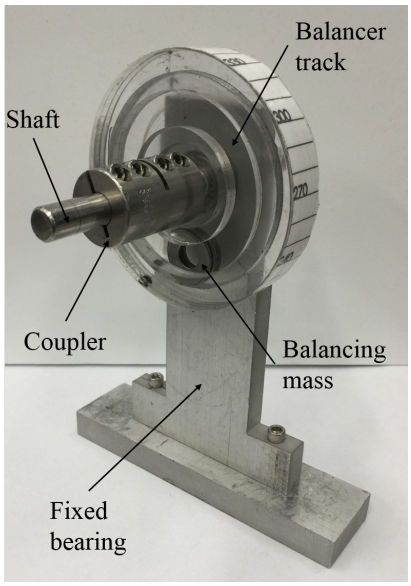

(b) Photograph of mounted passive balancing device.

Figure 3.19: Photographs of passive balancer device used in experiments.

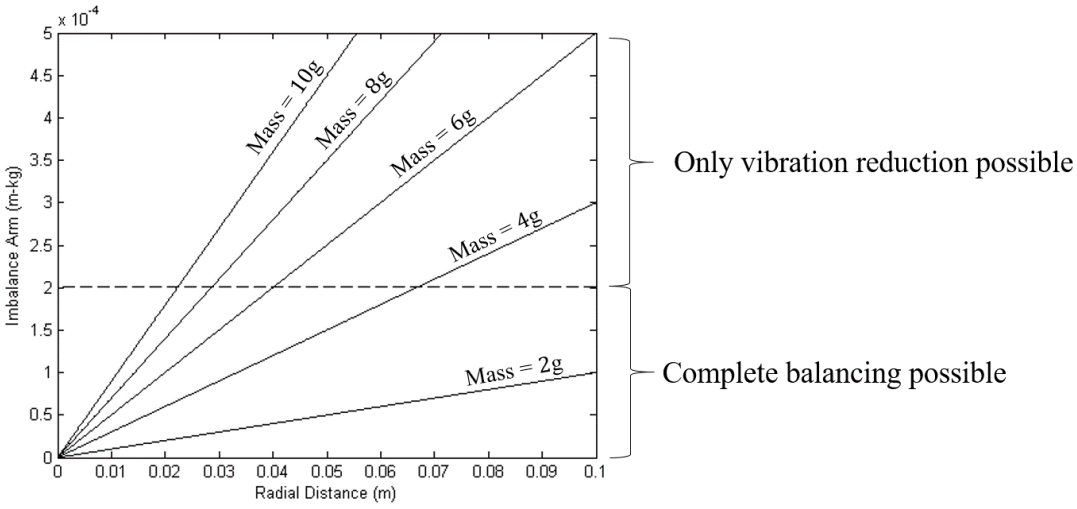

Figure 3.20: Combinations of imbalance arm and mass where balancing is possible (shown for a balancer with 2m-kg imbalance arm).

A great deal of attention is given to the interaction between the balancing masses and the track in this research. It was found that other than inertial forces,

the most significant influence to balancer motion is the static rolling friction. This can be clearly seen in an example shown in Figure 3.21. Here, the masses are at rest but not completely at the bottom of the track as one would expect due to gravity. The friction resisting the motion is greater than the gravitational load on the balancing masses.

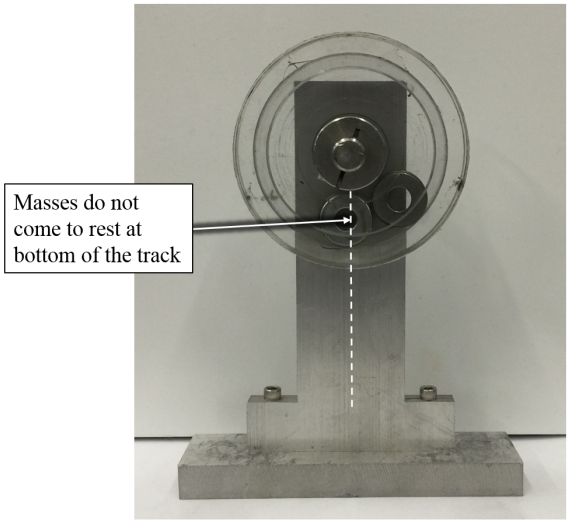

Figure 3.21: Effects of friction on ball motion.

Using high speed cameras to capture the motion of the balancing masses in the track, it was found that the masses do not slide but rather roll. Hence, the model and all calculations assume that the balancing masses roll in the track. To find the rolling friction coefficient of the mass/track, an experiment was conducted. High speed video recorded at 240 frames per second was used to capture the response of a balancing mass when released from rest. A time lapse of the video is shown in Figure 3.22. The balancing mass can be seen oscillating until coming to a stop.

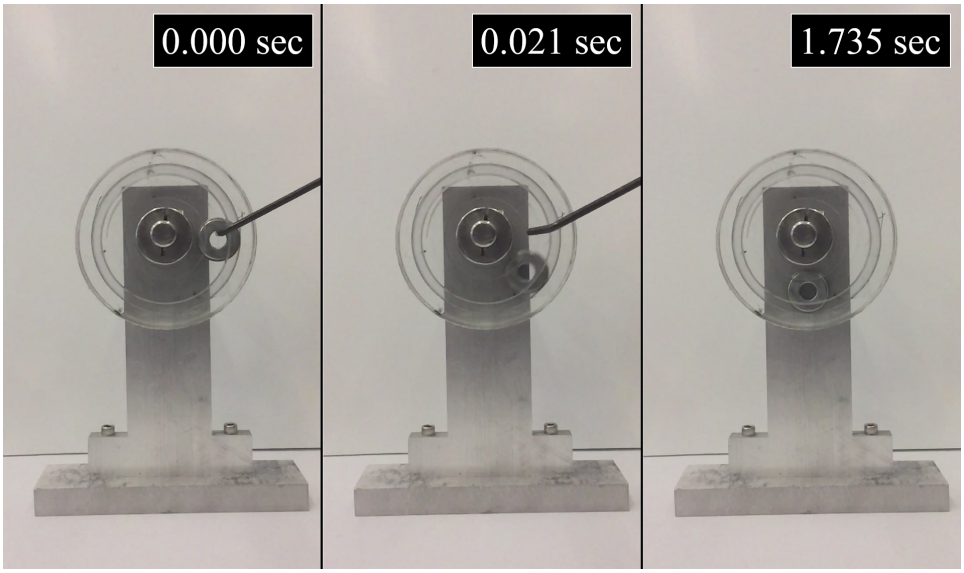

Figure 3.22: Time lapse of balancing mass going to rest (Run 6).

Multiple responses were captured and the results are listed in Table 3.4. When the balancing mass was held and then released from 0 degrees, it took an average of 1.761 seconds for its motion to decay. The standard deviation from 1.761 seconds is 0.040 seconds.

Table 3.4: High speed camera properties.

Run	Time
1	1.793 sec
2	1.806 sec
3	1.756 sec
4	1.802 sec
5	1.735 sec
6	1.735 sec
7	1.702 sec
Average:	1.761 sec

To achieve a similar response to the released mass, the viscous damping coefficient of the ball/track and the rolling resistance constant with dimension length were

modified. The parameter combinations that are used in the model are presented in Table 3.5. A typical rolling resistance constant for bearings is $1.00 \times 10^{-4} m$ [170], so model predictions will be generated with constants in that vicinity.

Table 3.5: Damping and friction parameters.

Case	Viscous damping coefficient (kg/s)	Rolling resistance constant (m)
1	0.05	0.00
2	0.03	2.00×10^{-4}
3	0.02	4.00×10^{-4}

The dimensionless rolling friction coefficient, μ_r, can be derived from the rolling resistance constant with dimension length, $\mu_{r,l}$, as shown in equation 3.2. The simulated mass release responses are shown in Figures 3.23–3.25.

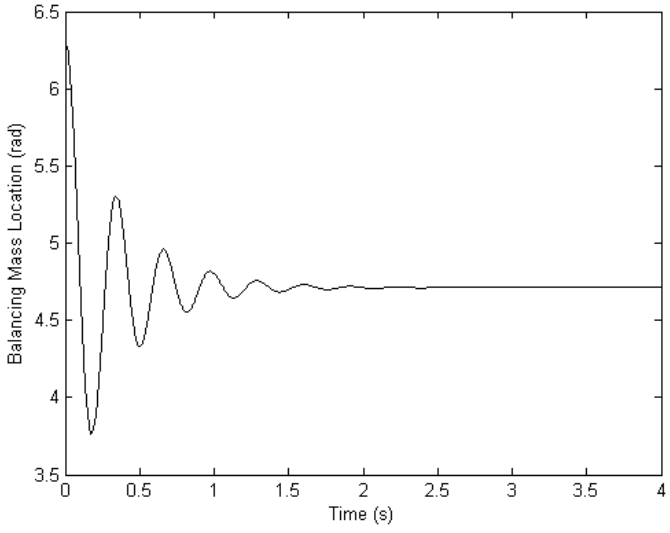

Figure 3.23: Simulated response of a mass released at 0 degrees ($c_{AB} = 0.05 kg/s$, $\mu_{r,l} = 0m$).

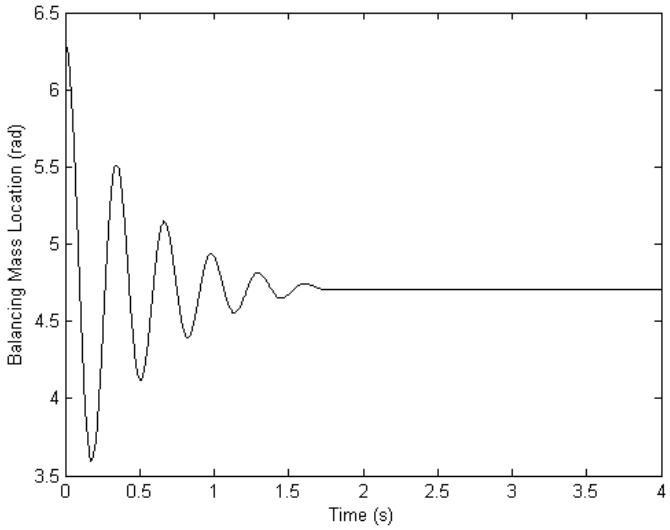

Figure 3.24: Simulated response of a mass released at 0 degrees ($c_{AB} = 0.03kg/s$, $\mu_{r,l} = 2.00 \times 10^4 m$).

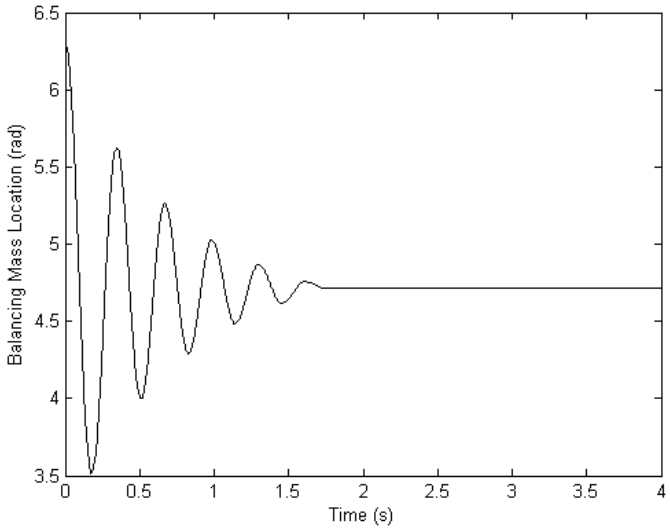

Figure 3.25: Simulated response of a mass released at 0 degrees ($c_{AB} = 0.02kg/s$, $\mu_{r,l} = 4.00 \times 10^4 m$).

$$\mu_r = \frac{\mu_{r,l}}{r_b} \tag{3.2}$$

Since the collisions between the balancing masses are inelastic, the coefficient of

restitution that describes the kinetic energy losses was obtained from published data. The coefficients of restitution for steel/steel impacts are shown in Figure 3.26. Those are experimental results generated by Sondergaard et al. in 1990 [34]. Given the dimensions of the balancing masses, the coefficient of restitution is 0.589.

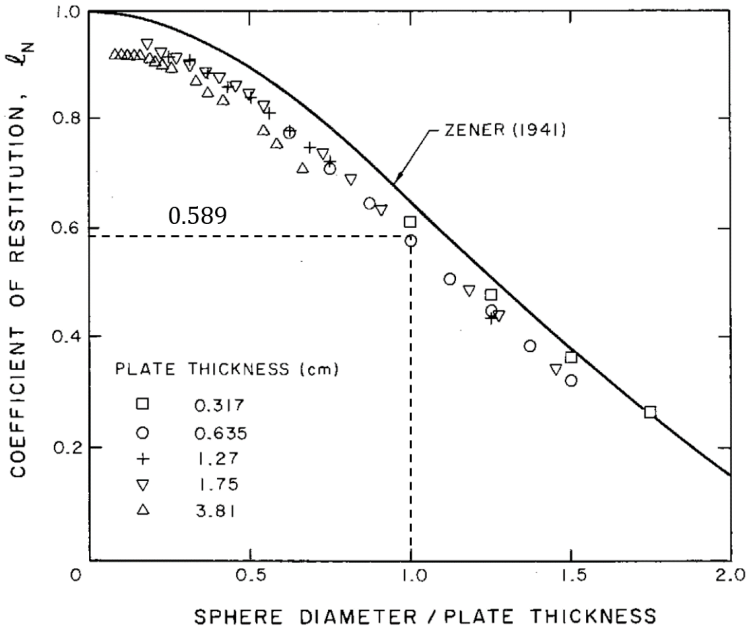

Figure 3.26: Coefficients of restitution for steel/steel collisions [34]

3.1.4 Bladed-hub

A bladed-hub (shown in Figure 3.27) is a component used in the experiment. Its purpose is providing means of attaching eccentric imbalance masses onto blades. This introduces controlled amount of imbalance where results can then be used to study the effectiveness of the passive balancer. Properties of the hub are listed in Table 3.6 and properties of the blades are listed in Table 3.7.

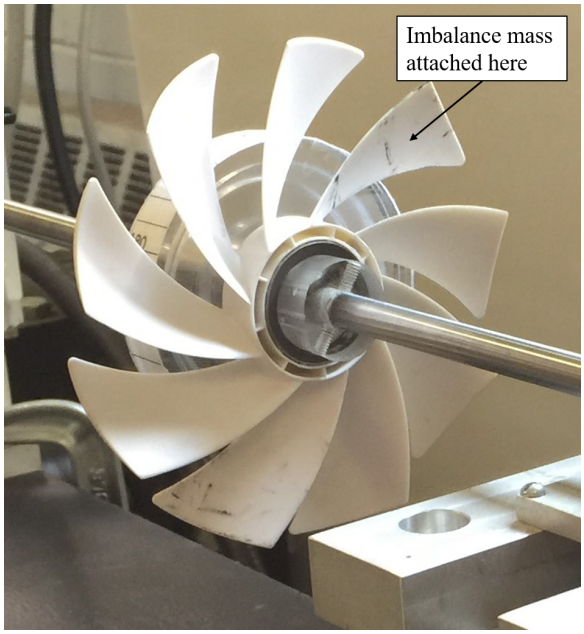

Figure 3.27: Photograph of bladed-hub.

Table 3.6: Hub properties.

Mass	$61.1 \times 10^{-3}\ kg$
Radius	$0.674\ in$
Thickness	$1.025\ in$
Location along shaft	$28.68\ in$

Table 3.7: Blade properties.

Number of blades	9
Mass	$2.25 \times 10^{-3}\ kg$
Radius	$2.6\ in$

3.1.5 Motor

The shaft is driven by a Baldor 2 HP CSM3558T-2 motor. The motor is capable of spinning the shaft with all components attached in the supercritical region up to

2000 RPM. With less components, the motor can spin up to 3500 RPM. The shaft speed can be controlled manually or programmed for specific speed profiles. The motor is fitted with an RPM sensor which is provides accurate means of recording the speed of the shaft.

3.2 Measurement Tools

Several sensors and instruments were used to collect experimental data from the test rig. An RPM sensor measured the speed of the shaft as rotated by the motor. An optical displacement sensor measured the shaft displacement. Data was collected using LABVIEW^{TM}. Special software was used view the high speed video footage from the camera.

3.2.1 Optical Displacement Sensor System

A Philtec, Inc. model RC90 fiber optic displacement sensor was used to measure the transverse vibrations of the shaft. The optical displacement sensor was chosen because it does not interfere with the shaft vibrations. It is completely detached from the shaft and has no influence on the response. A photograph of the displacement sensor is presented in Figure 3.28.

The accuracy of the fiberoptic displacement sensor was also a reason for using it. The displacement sensor has a resolution of $0.254\mu m$ which is satisfactory for the vibrations measured in the experiments and presented in this report. The calibration curve of the sensor is shown in Figure 3.29. The sensor possesses a linear range around 4mm, however, for the conversion from volts to mm in the

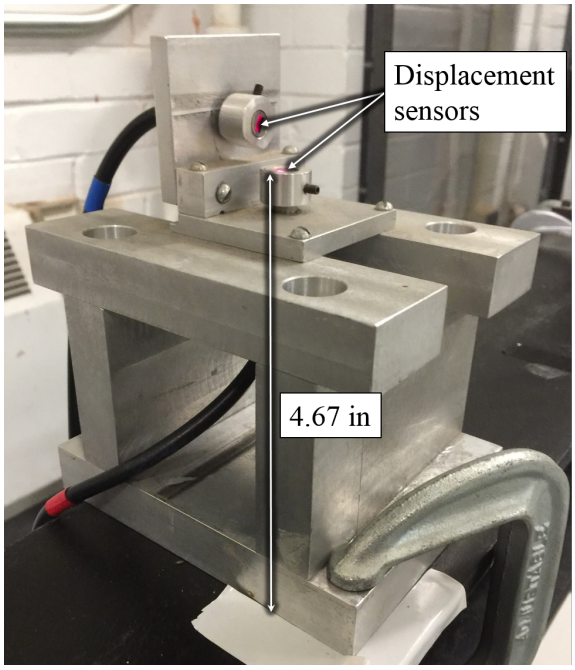

Figure 3.28: Photograph of the optical displacement sensor.

experimental data, the entire nonlinear curve was used for better accuracy.

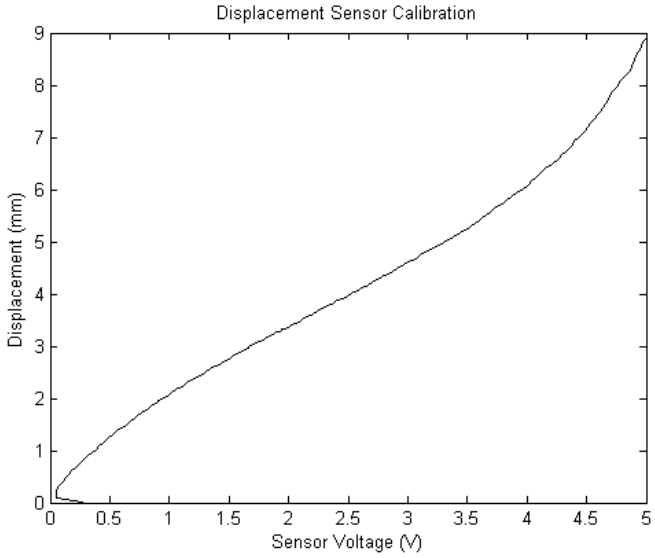

Figure 3.29: Calibration of optical displacement sensor.

3.2.2 High Speed Camera

A high speed camera was used in the data collection of the experiments. Due to the nature of the experiment, it is very difficult to measure the location of balancing masses. A high speed camera is very useful here since it allows the inspection of balancing mass locations from experiments. The camera used is the Phantom Mira 310 accompanied by an LED light source that was used to eliminate the capture area. The specifications of the camera are listed in Table 3.8.

Table 3.8: High speed camera properties.

Resolution	1280x800
Sample Rate	2000 pps
Exposure Time	490μs

3.3 Test Matrix

The main objective of the experiments was to evaluate the effectiveness of the passive balancing device. Hence, the test matrix is comprised of comparable scenarios where the passive balancing device is either attached or not included. First, the response of the system without the passive balancing device was experimentally evaluated at varying imbalance mass. The imbalance mass was varied in 2g increments ranging from 0g to 14g. A diagram of the testing procedure is presented in Figure 3.30. As shown, the rotation speed of the shaft is accelerated from rest to 1600 RPM, a supercritical speed, and then decelerated back to rest. For the entire speed variation, the RPM sensor records the speed of the shaft to first ensure accurate

RPM. The RPM data also allows the speed profile to be replicated in computer simulations.

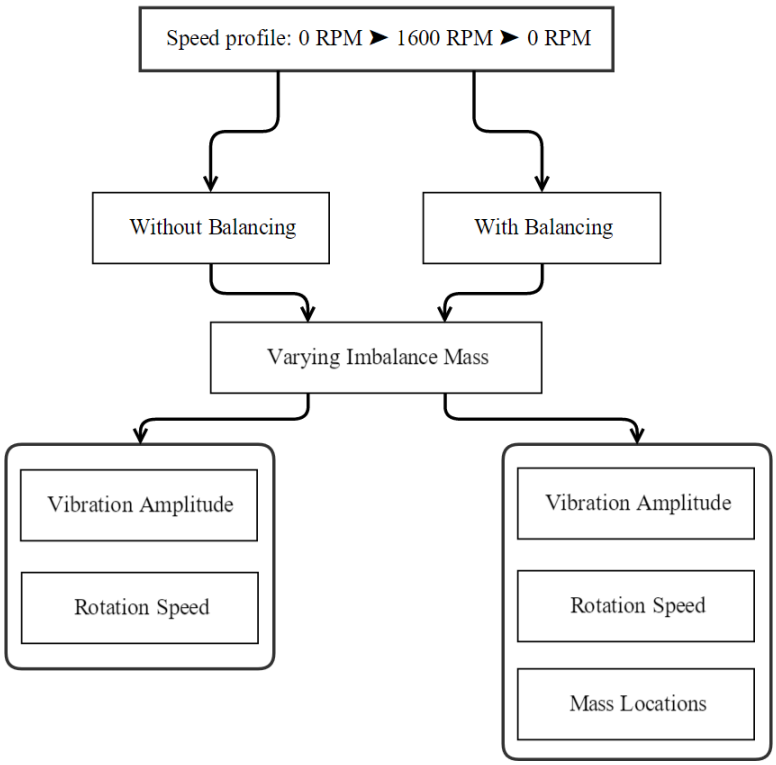

Figure 3.30: Experiment test matrix..

Along with RPM data, the vibration amplitude is recorded for the same duration. Data is collected for the time the shaft is accelerating, at steady-state, and when the shaft is decelerating. This is essential to study the transient as well as the steady state effects of passive balancing. The same testing procedures were then done again, but this time, the passive balancing device was mounted on the shaft. The collected data are shown in Table Figure 3.30 as well. The difference with the passive balancer experiments is the need to also measure the location of the balancing masses as well. The high speed camera was used to record the transient and steady-state balancing mass locations for each imbalance case.

Chapter 4

Experimental Results and Model Validation

In this chapter, the experimental and analytical results are presented. These results are then are then compared and the validity of the model is judged. Discussions are made about the transient and steady state responses of the system – namely, the transient response of the initial speed up from 0 RPM, the steady state response at the constant rpm region, and the transient response of the region of deceleration back to 0 RPM.

4.1 Experimental Results

Experimental system responses according to the test matrix shown in Chapter 3 are presented with and without a mounted passive balancing device. First, the motor RPM profile was made consistent between all experiment runs. The shaft was accelerated to supercritical speed at 1608 RPM and then held at constant speed to capture the steady state response. Following the steady state, the shaft

was decelerated back to rest. The profiles used in the experiment runs and the simulations are shown in Figure 4.1. The difference in time scale is only to decrease the computational requirement for the model simulations. Results are comparable still at each RPM region.

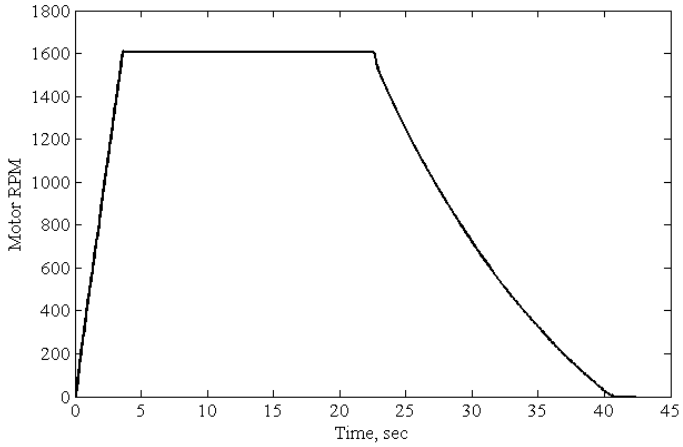

(a) Motor RPM profile used in experiments.

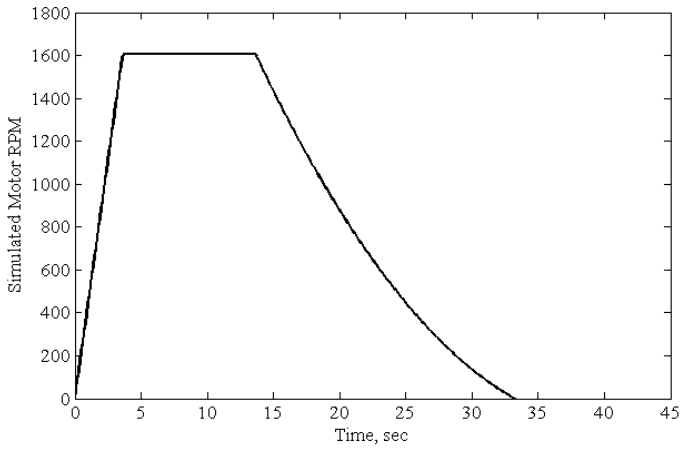

(b) Motor RPM profile used in simulations.

Figure 4.1: Motor RPM profile in experiment and simulation.

An example case to demonstrate the process of measuring the vibration amplitude is given in Figure 4.2. First, the shaft speed is measured and recorded along with the optical displacement sensor voltage. The voltage is then converted to

displacement using the calibration provided earlier in section 3.2.1. Finally, the vibration amplitude is calculated from the time history of the shaft displacement. In the same figure, the vibration amplitude is plotted against the shaft rotation speed.

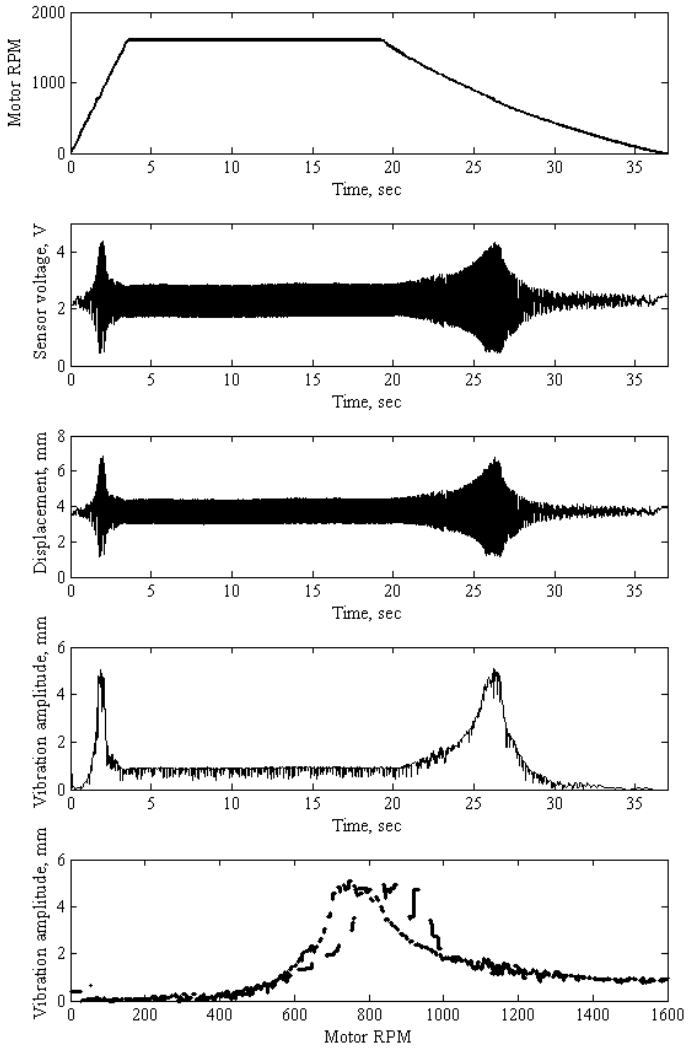

Figure 4.2: An example experimental case.

Before experiment runs were conducted, pre-existing vibrations in the test rig not due to hub mass imbalance or the passive balancers were found. These vibrations were removed from all subsequent experimental runs. The test rig was subjected to the RPM profile given earlier with no attached imbalance mass and no passive balancing device. The measured vibration amplitudes are given in Table 4.1 and the response is shown in Figure 4.3. The mean vibration amplitude is 4.586×10^{-4} meters with a standard deviation of 9.089×10^{-6} meters.

Table 4.1: Pre-existing vibration amplitude in test rig.

Run	Vibration Amplitude (m)
1	4.660×10^{-4}
2	4.618×10^{-4}
3	4.481×10^{-4}
4	4.498×10^{-4}
5	4.673×10^{-4}
Average:	4.586×10^{-4}

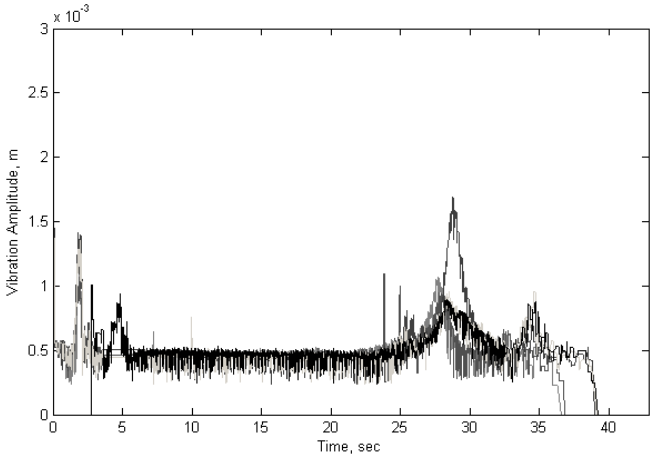

Figure 4.3: Vibration present in the test rig without additional imbalance or balancing (using previously shown RPM profile).

4.1.1 Performance Without Balancing

The shaft was spun in multiple runs for each added imbalance mass. The test rig setup remained consistent and the same RPM profile was applied. Mass was added in increments of $2g$ to the hub $1.8in$ from the center of the shaft. Example configurations are shown in Figure 4.5. A system without imbalance and without passive balancing is shown in Figure 4.5a, and a system with imbalance but without passive balancing is shown in Figure 4.5b.

The results along with their respective standard deviation are plotted in Figure 4.4. The response varies linearly with imbalance mass. The individual responses are later compared with model predictions.

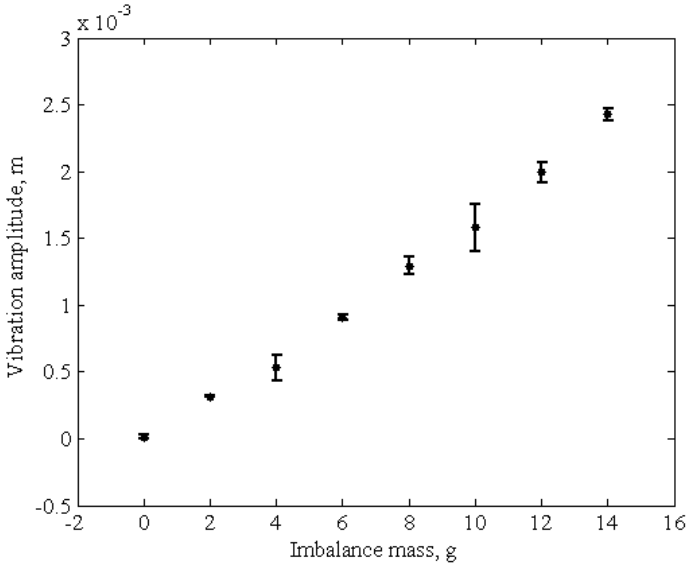

Figure 4.4: Experimental vibration amplitude without passive balancing device.

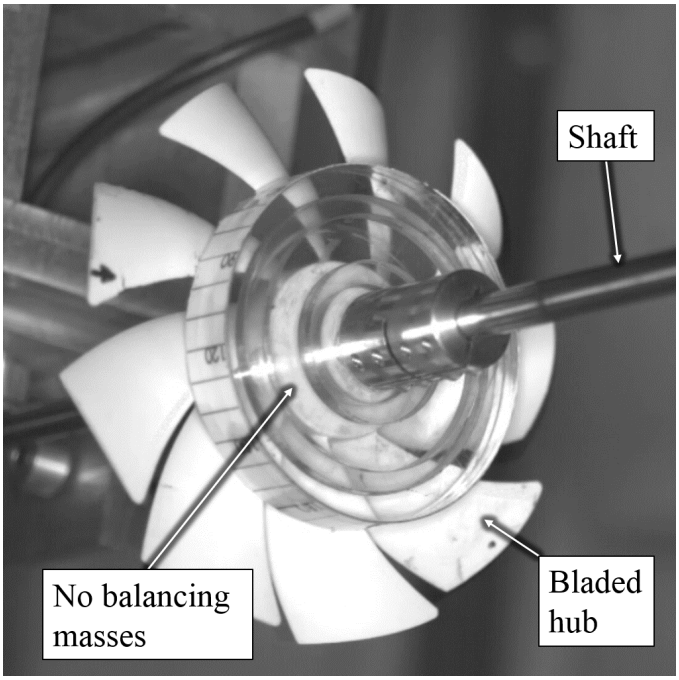

(a) Configuration without imbalance mass and balancing masses.

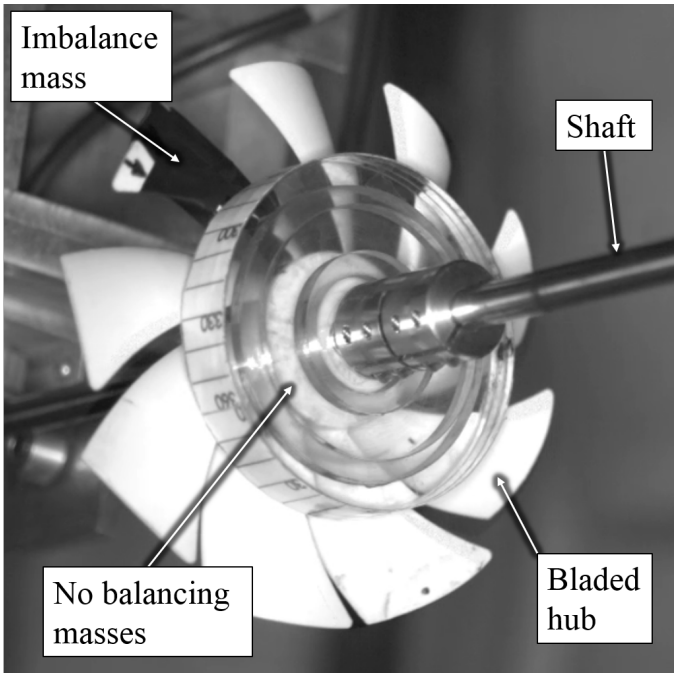

(b) Configuration with imbalance mass and without balancing masses.

Figure 4.5: Experimental configuration for performance without passive balancing.

The adjusted mean vibration amplitudes at each imbalance mass increment are presented in Table 4.2.

Table 4.2: Measured and adjusted vibration amplitudes when no passive balancing device is attached.

Intended Imbalance Mass (g)	Actual Imbalance Mass (g)	Measured Vibration Amplitude (m)	Adjusted Vibration Amplitude (m)
0	0	4.621×10^{-4}	1.411×10^{-5}
2	2	7.621×10^{-4}	3.141×10^{-4}
4	4	9.801×10^{-4}	5.320×10^{-4}
6	6	1.354×10^{-3}	9.061×10^{-4}
8	8	1.741×10^{-3}	1.293×10^{-3}
10	10	2.028×10^{-3}	1.580×10^{-3}
12	12	2.443×10^{-3}	1.994×10^{-3}
14	14	2.875×10^{-3}	2.427×10^{-3}

4.1.2 Performance With Balancing

The same experiment runs were carried on the test rig with the balancing device mounted on the hub. Again, imbalance mass was added in increments of $2g$ and $1.8in$ away from the center of the shaft. The vibration amplitude was measured for each run along with the balancing masses angular locations in the track. The imbalance mass had a phase of 45 degrees.

It is clear from the experimental results that passive balancing generally reduces vibrations when the system is operating at a supercritical speed. With the exception of the balancing response when there was no imbalance mass and some cases where there was a $2g$ imbalance mass, the passive balancing devices provided vibration suppression. The trend that is seen before reaching critical balancing potential (when balancing masses are completely opposite to the imbalance mass in the track)

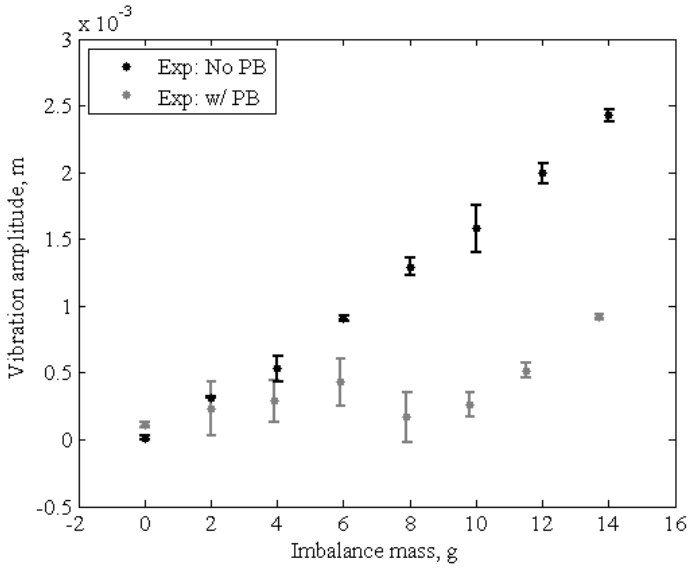

Figure 4.6: Experimental vibration amplitude with passive balancing device.

Table 4.3: Measured and adjusted vibration amplitudes when passive balancing device is attached.

Intended Imbalance Mass (g)	Actual Imbalance Mass (g)	Measured Vibration Amplitude (m)	Adjusted Vibration Amplitude (m)
0	0	5.604×10^{-4}	1.123×10^{-4}
2	2	6.761×10^{-4}	2.280×10^{-4}
4	3.9	7.352×10^{-4}	2.871×10^{-4}
6	5.9	8.770×10^{-4}	4.289×10^{-4}
8	7.9	6.149×10^{-4}	1.668×10^{-4}
10	9.8	7.068×10^{-4}	2.588×10^{-4}
12	11.5	9.641×10^{-3}	5.160×10^{-4}
14	13.7	1.366×10^{-3}	9.177×10^{-4}

is not found in any model that ignores balancer mass/track friction. The passive balancer performance is suboptimal in that region as is evident by the lack of complete vibration suppression. The model presented in this thesis aims to address that region where the total elimination of vibration is not occurring as predicted in many published models.

Before presenting model predictions for the non-balanced and balanced system, the experimentally measured system response where a balancer was not attached is compared to a response where the balancer was attached. The two cases presented in Figures 4.7 and 4.8 for an imbalance of 4g and 14g respectively depicts the effect of having a mounted passive balancing device. Overall, the device reduces shaft vibrations in the operational (steady state) region. In the transient states, the effect is not as clear. In one case, (Figure 4.7b) the passive balancer reduced the vibration amplitude in the both transient regions (acceleration and deceleration of shaft). In contrast, in Figure 4.8b, the passive balancer increased transient vibrations while still reducing steady state vibrations.

In the system response presented in Figure 4.7, the steady state vibration amplitude was reduced by 51% due to the presence of the passive balancer. The acceleration region vibration amplitude was reduced by 46% and the deceleration region vibration amplitude was reduced by 36%. For the system response presented in Figure 4.8, the steady state vibration decreased by 61%, the acceleration region amplitude increased by 28.8%, and the deceleration region amplitude increased by 32%.

There is a distinction between the balancer performance when low imbalance is present (imbalance mass that is less than the maximum balancing potential of the passive balancer) versus a high imbalance scenario. Comparing Figures 4.7 and 4.8, the passive balancing masses in the 4g imbalance scenario required more time to reach steady state and introduced an additional transient region. However, in this case, peak and steady-state vibration amplitudes were reduced in all operating regions. In the 14g imbalance scenario, the passive balancer reaches steady state

faster, however, the transient vibration amplitudes were amplified.

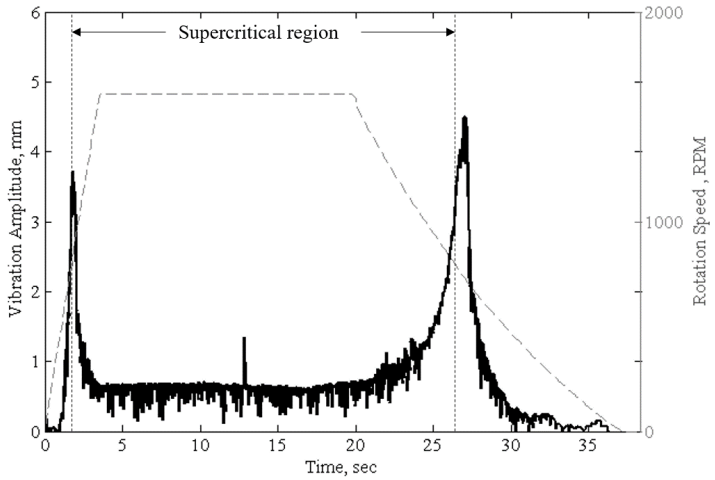

(a) System response without passive balancing.

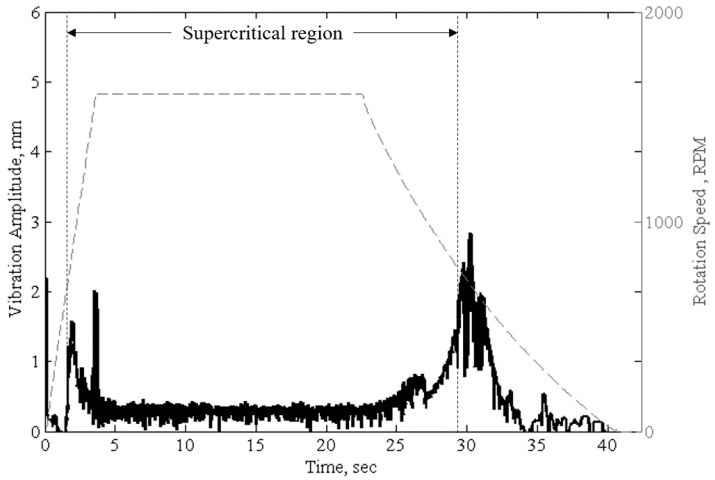

(b) System response with passive balancing.

Figure 4.7: Experimental system responses without and with passive balancing, and 4g imbalance mass.

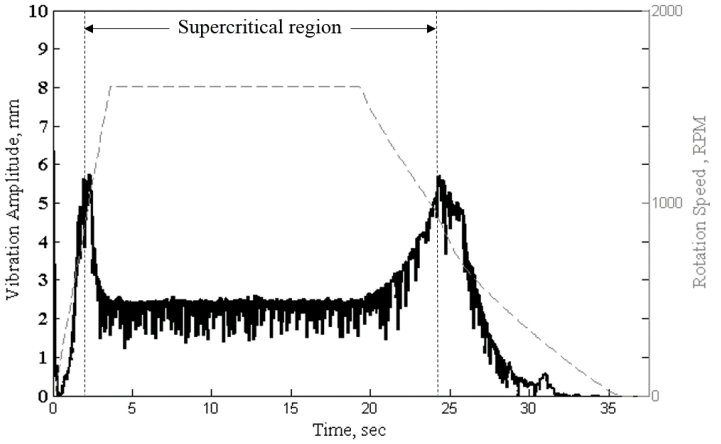

(a) System response without passive balancing.

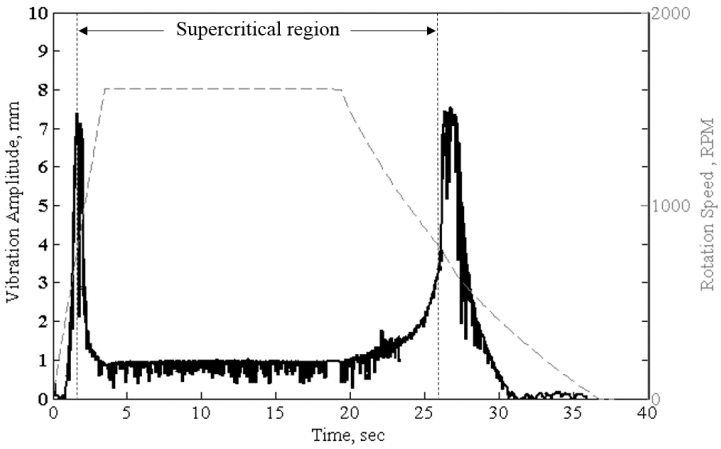

(b) System response with passive balancing.

Figure 4.8: Experimental system responses without and with passive balancing, and 14g imbalance mass.

4.2 Model Prediction: Without Balancer

System responses were numerically evaluated for the experimental system without a passive balancing device attached. The parameters used in the simulation studies are the same as the ones listed in Chapter 2. The mode shapes used for the shaft bending satisfy a fixed-pinned condition and are listed in Appendix 1.1.3.

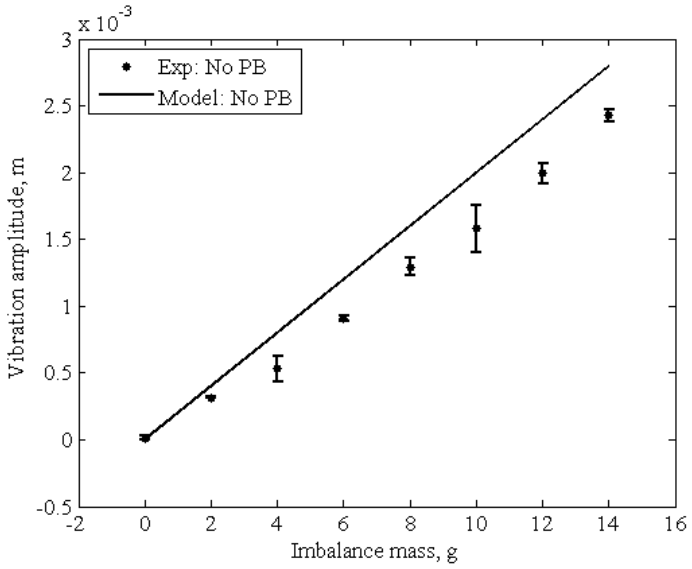

Figure 4.9: Model prediction of vibration amplitude without passive balancing device.

The model predicts the same linear relationship between the vibration amplitude and the attached imbalance mass. However, it over predicts the vibration amplitude. This is most likely due to the boundary condition assumption because fixed-pinned boundary conditions do not perfectly represent the rotating system present in the test rig. The system response is compared for the cases with imbalance mass of 2g, 8g, and 14g. Then, the first resonance frequency is compared between the experiment and the model.

The accuracy of the model in those cases is best described in Table 4.4. Two trends can be derived from the relationship between the model predictions and the experimental results for a shaft without a passive balancer. First, the predicted transient response is not highly accurate for high imbalance mass (56%) and more accurate for low imbalance (8%). The steady state prediction is more accurate ranging between 31% and 12%. The steady state prediction improved as imbalance

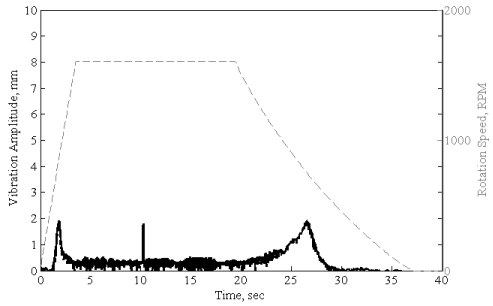

(a) Experimental system response without passive balancing.

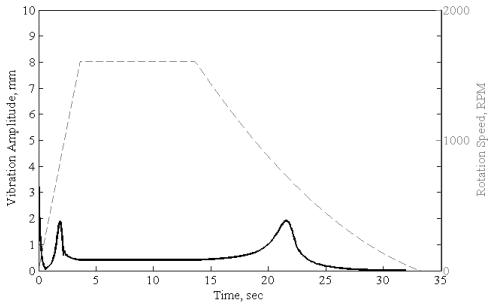

(b) Simulated system response without passive balancing.

Figure 4.10: Experimental and simulated system responses without passive balancing, and 2g imbalance mass.

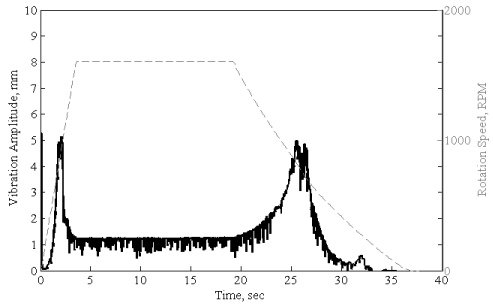

(a) Experimental system response without passive balancing.

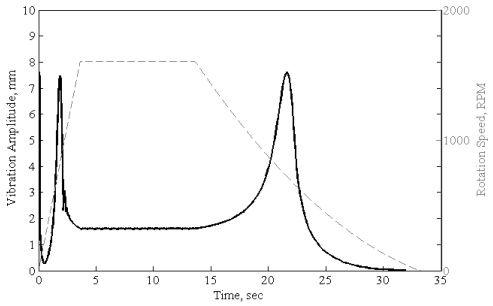

(b) Simulated system response without passive balancing.

Figure 4.11: Experimental and simulated system responses without passive balancing, and 8g imbalance mass.

mass was added to the system. The effect was the opposite on the transient response vibration amplitudes. The large disparity in the predicted and actual values can be attributed to the boundary condition assumption. In addition, during passage through resonance, computer models tend to show excessively high amplitudes which could be occurring in this case.

Finally, the resonance of the structure was investigated experimentally and numerically. The system response and its relationship with the shaft speed is shown

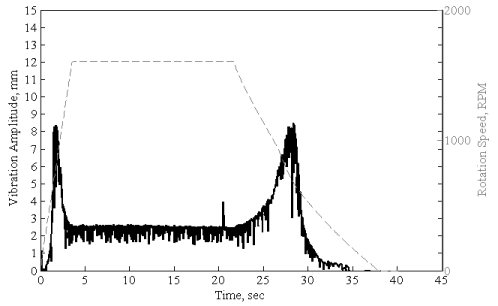

(a) Experimental system response without passive balancing.

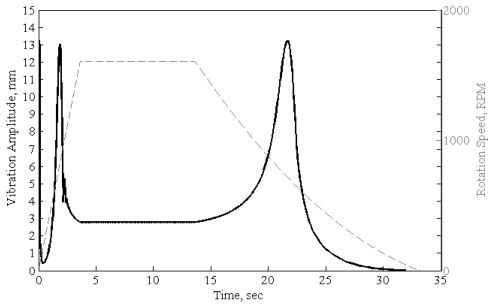

(b) Simulated system response without passive balancing.

Figure 4.12: Experimental and simulated system responses without passive balancing, and 14g imbalance mass.

Table 4.4: Accuracy of the model in predicting shaft vibration without passive balancing.

Imbalance Mass, g	Acceleration Transient Amplitude, mm	Steady State Amplitude, mm	Deceleration Transient Amplitude, mm
Experiment			
2	1.914	0.311	1.918
8	5.134	1.246	4.996
14	8.349	2.481	8.473
Simulation			
2	1.761	0.409	1.914
8	7.413	1.614	7.602
14	13.02	2.787	13.19
Simulation Accuracy			
2	-7.99%	+31.51%	-0.21%
8	+44.39%	+29.53%	+52.16%
14	+55.95%	+12.33%	+55.67%

in Figure 4.13. The amplitudes are exaggerated at resonance as can be seen about 800 RPM. The model predicted first resonance was within 3% of the experimental value.

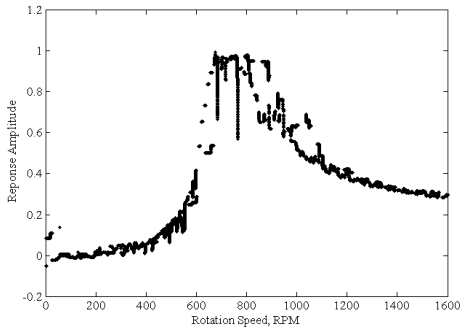

(a) Experimental system response versus shaft speed.

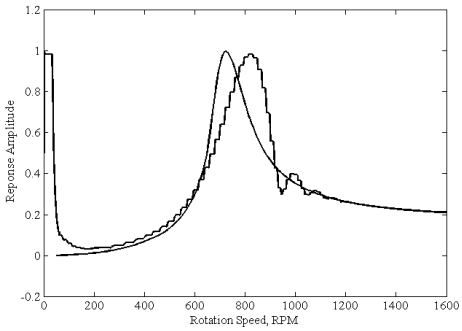

(b) Simulated system response versus shaft speed.

Figure 4.13: Experimental and simulated system responses versus the shaft speed.

4.3 Model Prediction: With Balancer

As mentioned earlier, the mode will be used to predict the dynamic behavior of the passive balancer in three cases. Mainly, the friction will be varied ranging from no friction (complete viscous damping) to high friction. This section highlights the effects that friction has on the ability to predict passive balancer performance.

4.3.1 Reference Case: No Friction and No Collision

Before the predictions of the new model are presented, a three dimensional model with no collision and no friction is used to generate a reference for the accuracy of previous models. It should be noted that even this artificially limited model is still a more comprehensive model that current models typically used in passive balancing studies. Currently, studies ignore some or all physical effects such as gravity, rotational inertia and three dimensionality. The predictions of this reference model aim to represent published modeling efforts but, in reality, this model will have predictions with higher accuracy than published models.

Numerical simulations were carried out to generate system responses with the passive balancing. For the model with no balancing mass collision and no friction between the masses and the track, the results are plotted in Figure 4.14. This model, which relies on viscous damping as the sole source of balancer energy dissipation, predicts perfect balancing over the entire range of operation for the passive device. This model is unable to capture the suboptimal performance of the passive balancer below the critical balancing potential. This is aligned with what has been shown in studies using viscous damping as the only source of energy dissipation.

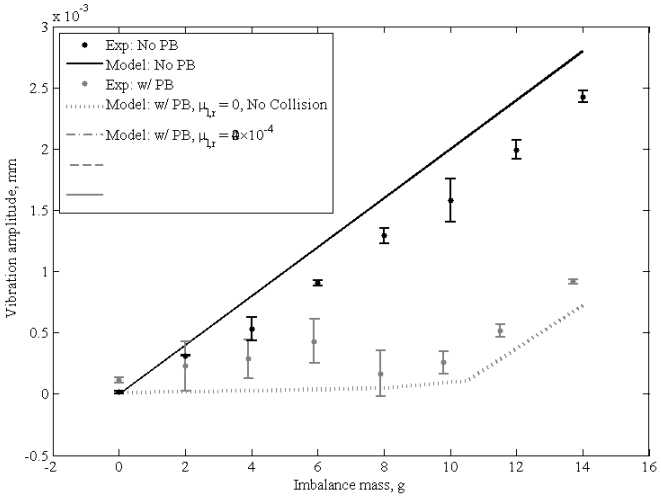

Figure 4.14: Experimental vibration amplitude with passive balancing device, no friction, and no collision.

It is clear that this is not always the case achieving perfect balancing as the experimental results clearly demonstrate that passive balancing does not completely eliminate vibration in certain conditions. In addition, this model over predicts the balancing capability of the passive balancer due to the lack of balancing mass collisions. As shown for imbalance masses above 10g, the model predicts more vibration suppression than possible. This is due to the balancing masses assuming

the exact location in the track according to the model (compared to being separated because they physically cannot reach the perfect equilibrium position).

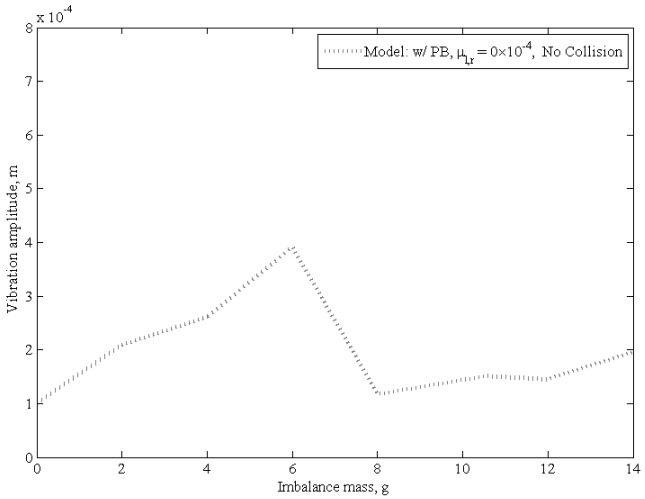

Figure 4.15: Discrepancy of amplitude prediction of the passive balancing model without collision and friction.

The difference between the predicted and experimental vibration amplitudes is shown in Figure 4.15. The following sections discuss and present results from the new model which includes balancing mass collision, viscous damping, and mass rolling resistance.

4.3.2 Case 1: No Friction

Currently published works and studies predominantly deploy viscous damping as the only source of energy dissipation in the passive balancer model. This section will present yielded results for a passive balancing system where only viscous damping is present. Numerically evaluated system responses according to the test matrix are presented in Figure 4.16. This figure presents previous results as well as the passive balancing prediction from case 1. This model predicts perfect balancing

wherever possible (only limited by the mass of the balancing masses).

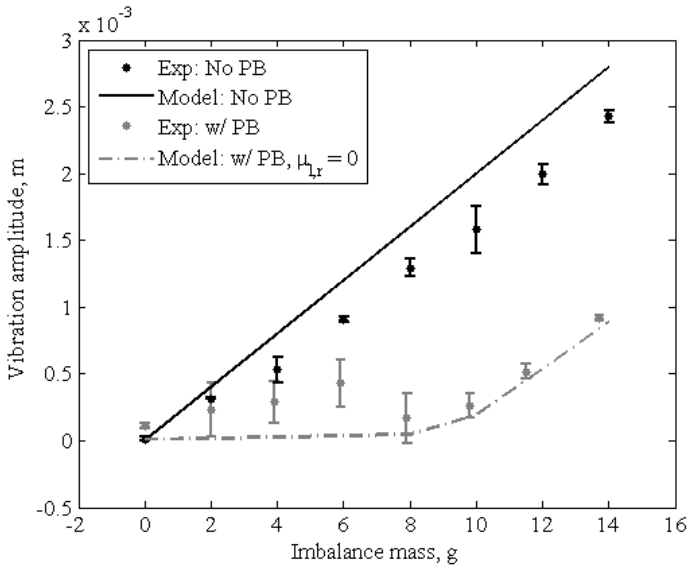

Figure 4.16: Experimental vibration amplitude with passive balancing device and no friction.

The results are very similar to the predictions of the reference model. Both do not predict the degraded performance of the passive balancing device. The model here however features balancing mass inelastic collisions. The effect of this addition can be seen at high imbalance mass. In this model, the vibration amplitude prediction is not over predicted like the model which lacked mass collision. The difference between the predicted vibration amplitude values and the experimentally measured ones is shown in Figure 4.17. When compared to the plot of the reference model, this model is more accurate when the imbalance mass is high.

Example response of the balancing masses under this model are shown in Figures 4.18 and 4.19. The balancing masses converge during steady state to cancel or reduce vibration due to mass imbalance in the hub. In Figure 4.19b, the balancing masses cannot converge further as they cannot go through on another. This is a

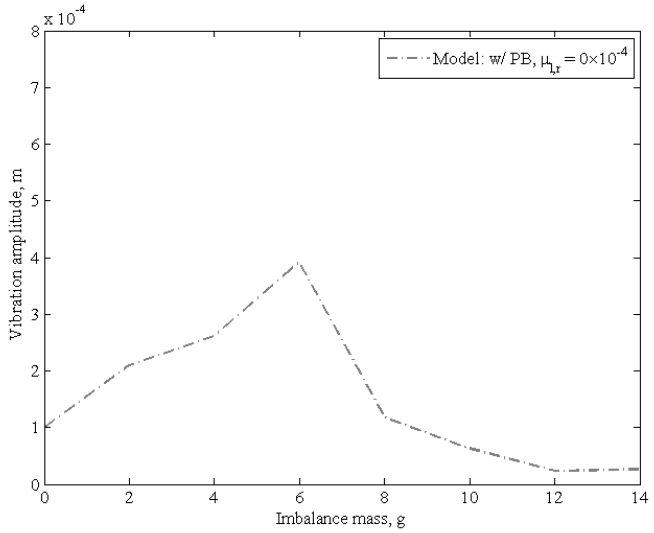

Figure 4.17: Discrepancy of amplitude prediction of the passive balancing model without friction.

key improvement over previous models where balancing masses or balls are usually allowed to pass through other masses.

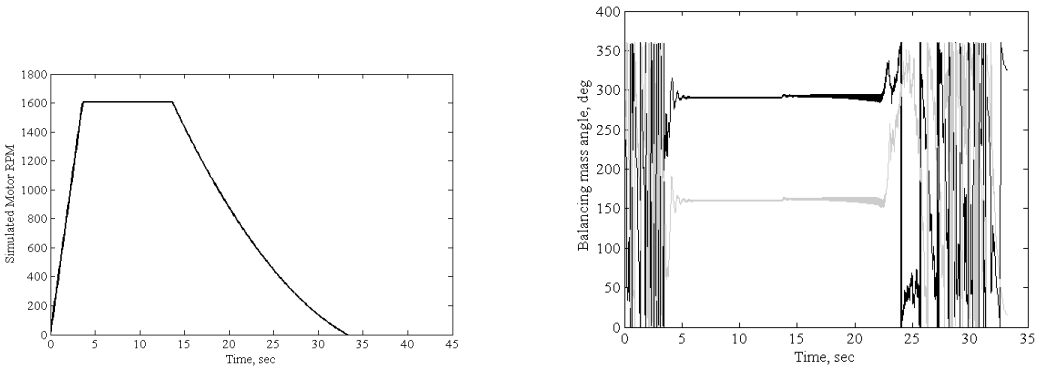

(a) Shaft speed profile.

(b) Model predicted balancing mass location.

Figure 4.18: Simulated passive balancer response (case 1, 4g imbalance mass)

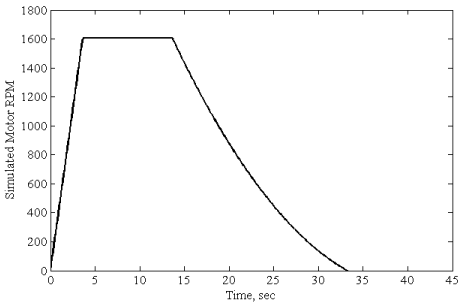

(a) Model predicted balancing mass location.

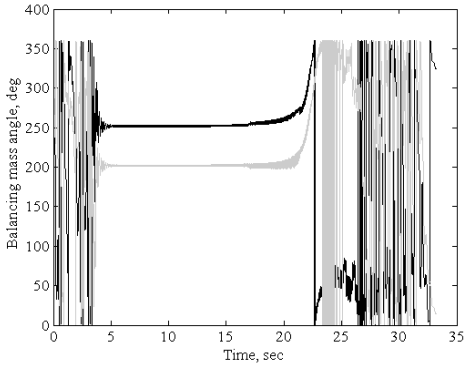

(b) Model predicted balancing mass location.

Figure 4.19: Simulated passive balancer response (case 1, 12g imbalance mass)

4.3.3 Case 2: Low Friction

In this section, numerical simulation results of the model with low friction ($\mu_{l,r} = 2 \times 10^{-4}$) and viscous damping are presented. The performance of the passive balancer in terms of steady-state vibration amplitude is shown in Figure 4.20. The end result is extremely similar to the performance predicted by a viscous damping model. Here, the passive balancer also performs optimally in all imbalance conditions.

The discrepancy between the predicted values of this model and the experimental values is plotted in Figure 4.21. Since the performance was very similar to the performance predicted in case 1, the variance between the predictions and the experiment match case 1 closely.

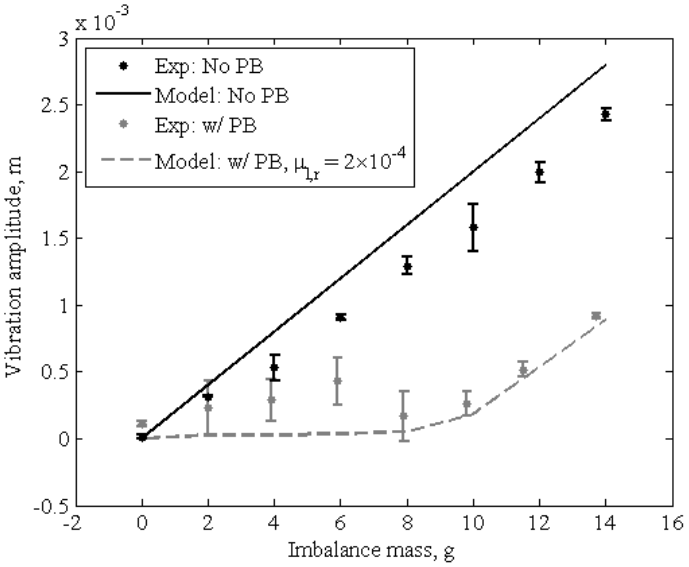

Figure 4.20: Experimental vibration amplitude with passive balancing device and low friction.

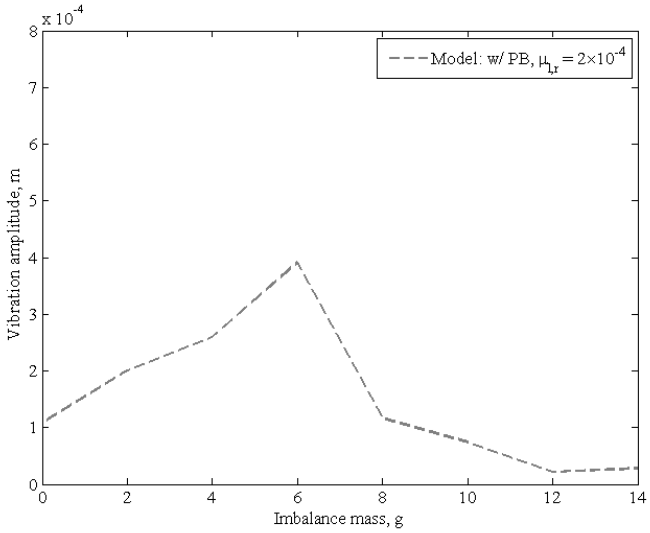

Figure 4.21: Discrepancy of amplitude prediction of the passive balancing model with low friction.

4.3.4 Case 3: Friction

In the third case, additional friction is added to the model. Specifically, the rolling friction coefficient is increased to 4×10^{-4}. The results of the computer simulations of each imbalance mass case are plotted in Figure 4.22. Clearly, the model with the friction from case 3 resembles the experimental response of the system more than the other two cases. In this case, the passive balancer correctly does not perform optimally before the critical balancing potential is reached. There are residual vibrations since the force that guides the balancing masses is not greater that the friction resisting the motion. Due to the nature of viscous damping, this problem is not represented at all when viscous damping is used as the sole energy loss mechanism.

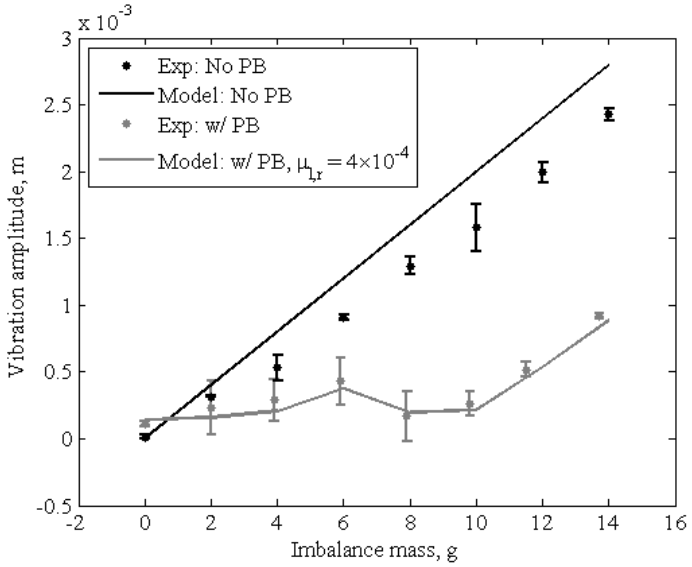

Figure 4.22: Experimental vibration amplitude with passive balancing device and friction.

The difference between the predicted values in case 3 and their experimental counterparts is shown in Figure 4.23. The discrepancy is lower than the previously

presented models. At the highest, the model with adequate friction improved the predicted value by 86%. A more detailed accuracy comparison is provided at the end of this chapter.

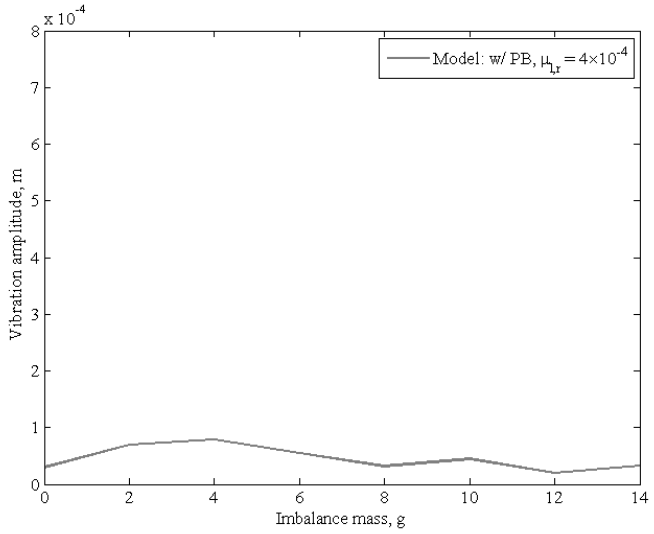

Figure 4.23: Discrepancy of amplitude prediction of the passive balancing model with friction.

The balancing mass locations were captured for each experiment run using the high speed camera. Example photo stills from the high speed videos are shown in Figure 4.24. The measured balancing mass positions are shown in Figures 4.25–4.32. The angles of the masses are accurate to 5 degrees. Overlaid onto the mass position charts is the imbalance mass location as well as the predicted balancing mass locations based on case 3.

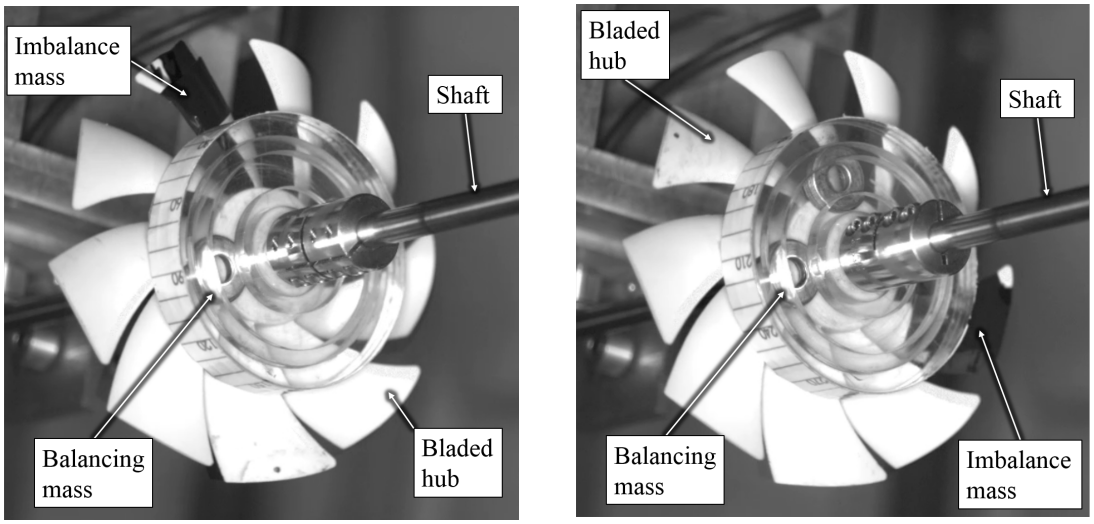

(a) Balancing mass located at 94 degrees. (b) Balancing mass located at 212 degrees.

Figure 4.24: High speed video allows measuring balancing mass circumferential location.

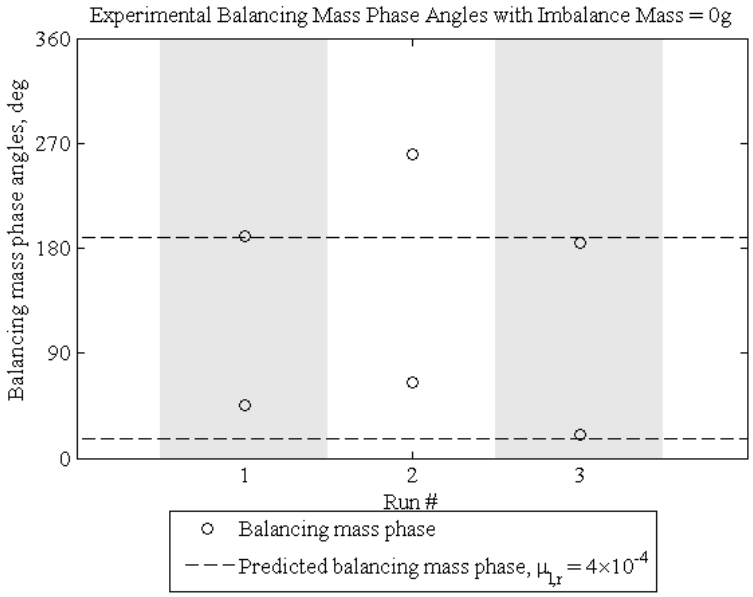

Figure 4.25: Experimental balancing mass locations and predicted locations in case 3 (imbalance mass = 0g).

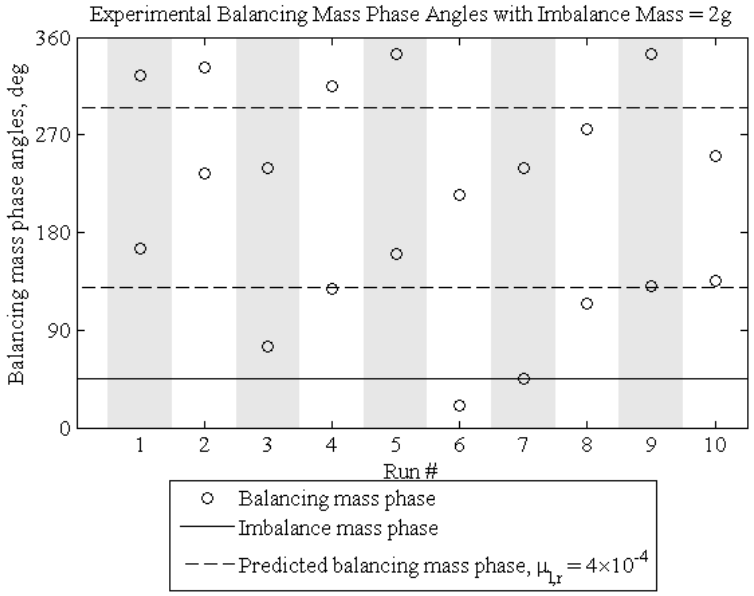

Figure 4.26: Experimental balancing mass locations and predicted locations in case 3 (imbalance mass = 2g).

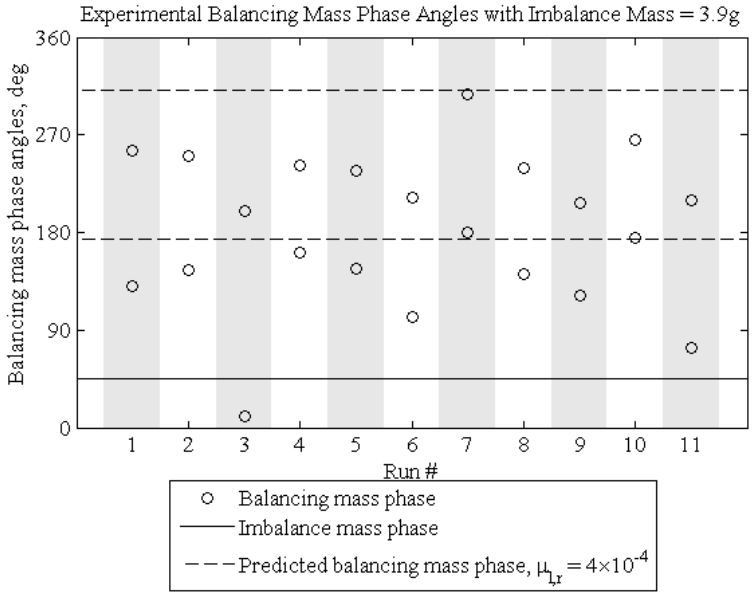

Figure 4.27: Experimental balancing mass locations and predicted locations in case 3 (imbalance mass = 3.9g).

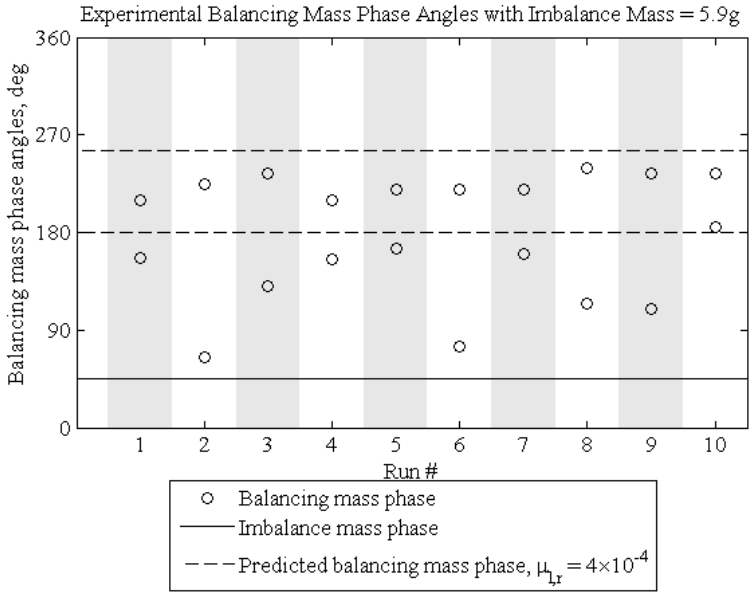

Figure 4.28: Experimental balancing mass locations and predicted locations in case 3 (imbalance mass = 5.9g).

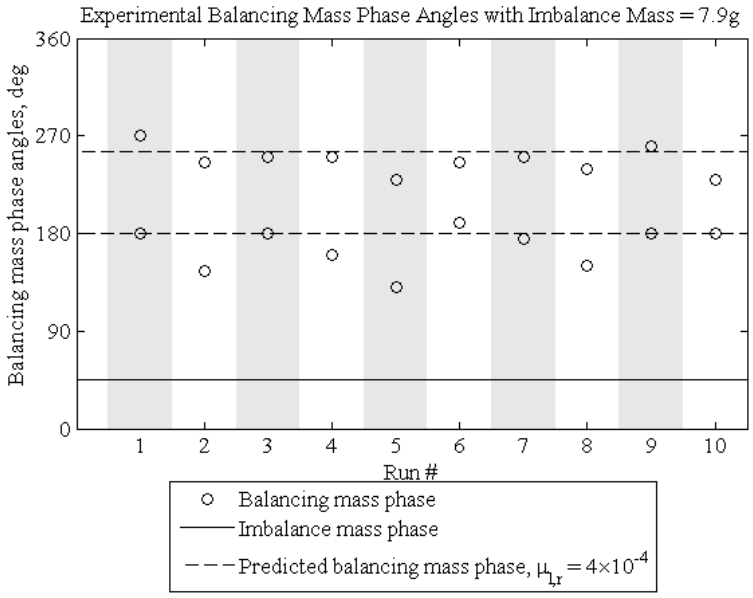

Figure 4.29: Experimental balancing mass locations and predicted locations in case 3 (imbalance mass = 7.9g).

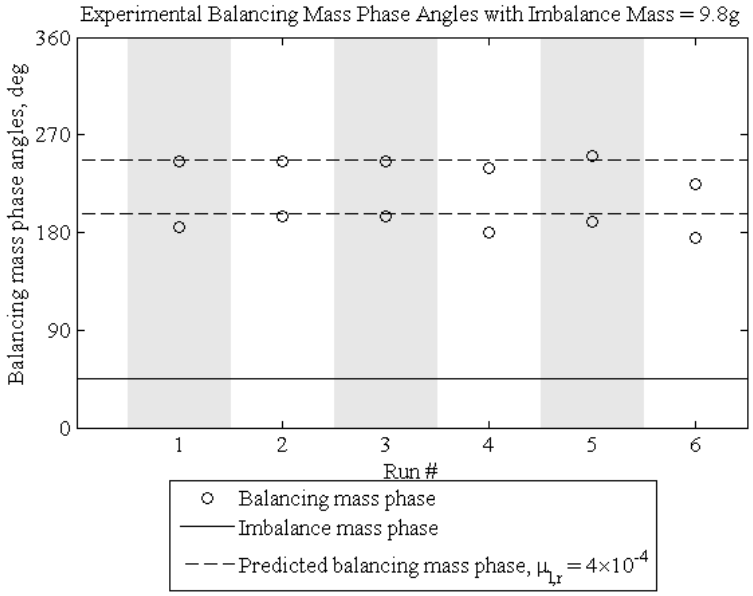

Figure 4.30: Experimental balancing mass locations and predicted locations in case 3 (imbalance mass = 9.8g).

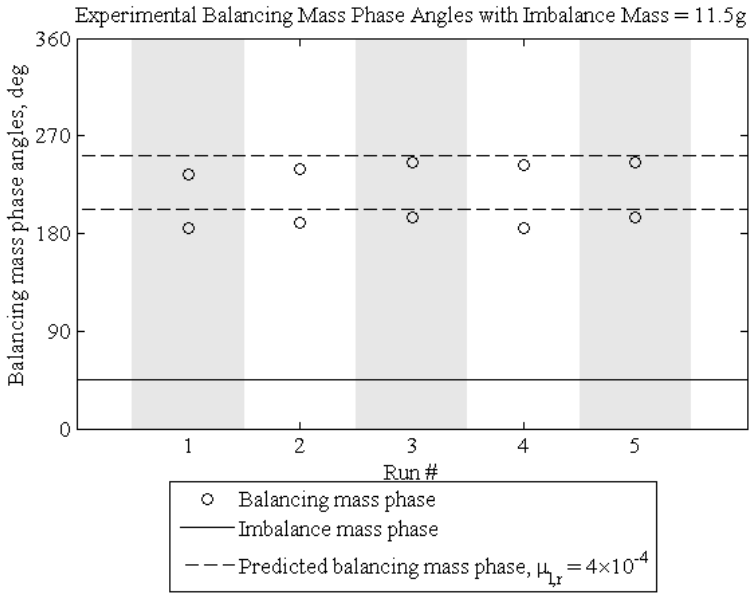

Figure 4.31: Experimental balancing mass locations and predicted locations in case 3 (imbalance mass = 11.5g).

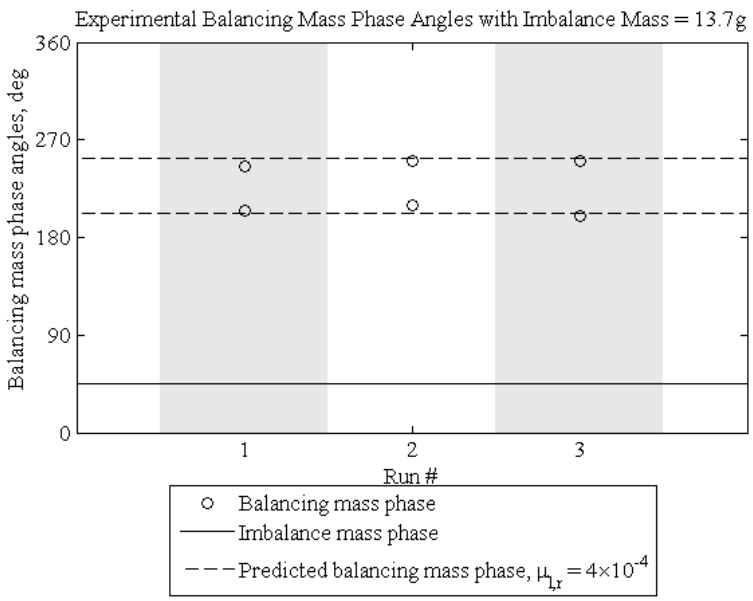

Figure 4.32: Experimental balancing mass locations and predicted locations in case 3 (imbalance mass = 13.7g).

As shown, the balancing masses locations are not uniform when the system has low imbalance mass. This is due to friction increasingly becoming the driving force of the passive balancer as the imbalance in the system decreases. Taking the experimental balancing mass positions shown in Figure 4.26, for example, the balancing masses might appear to not follow any trend. However, if the difference between the balancing mass positions was plotted (Figure 4.33), the trend in the mass positions becomes obvious.

At low imbalance mass, such as 2g, the forcing function acting on the balancing masses due to the imbalance is outweighed by the friction loads. Hence, the balancing masses assume locations which are 180 ($\pm$ the effects of friction) degrees apart. In Figure 4.33, the dots represent the experimentally measured angular difference of the balancing masses in each run. The solid line marks the 180 degrees

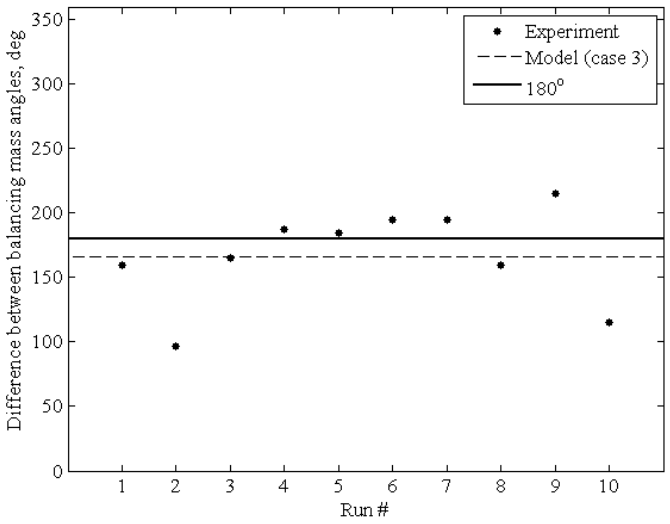

Figure 4.33: Difference between balancing mass positions (imbalance mass = 2g).

angle and the dashed line is the predicted difference from case 3. In runs 2 and 10, the balancing masses assume positions that better reduce vibration.

The model presented here was able to predict many of the non-optimal balancer mass locations (shown in Figures 4.25–4.32). It has been shown experimentally before that the passive balancers randomly end in locations near the equilibrium state when friction is involved [164]. However, here it has been predicted through full non-linear simulation and verified experimentally.

Several of those matching simulated cases are compared to their experimental counterpart. The transient and steady-state responses are compared for the passive balanced system with an imbalance mass of 0, 6, 12, and 14g. In Figures 4.34–4.37, the experimentally determined system response is displayed for a shaft with added imbalance pass and a mounted passive balancing device. In addition, the model predicted (case 3) system response is presented along with the predicted balancing mass behavior.

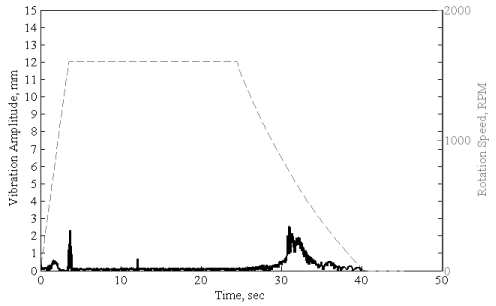

(a) Experimental system response.

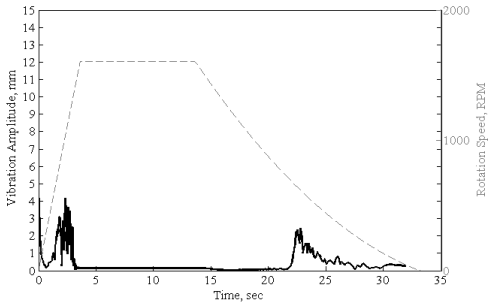

(b) Simulated system response.

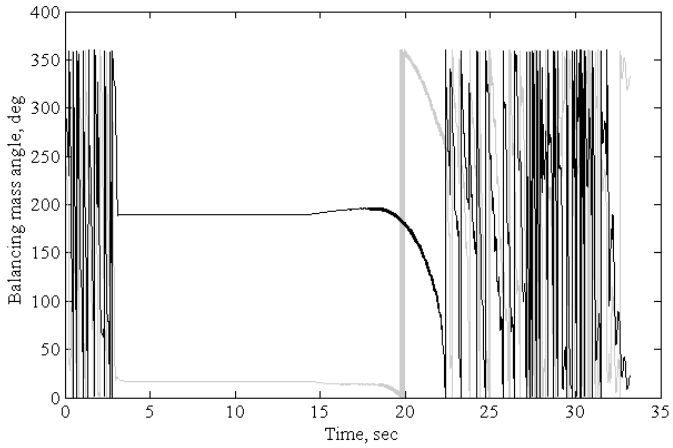

(c) Simulated balancing mass locations.

Figure 4.34: Experimental and simulated system responses (case 3, 0g imbalance mass)

For the 0g imbalance condition, the model was able to predict the non-zero residual vibration due to the balancing masses not assuming perfect balancing positions. In fact, the model predicts the balancing masses to reside in 17 and 189.5 degrees (non-180 degree difference). The experimental measurement of the presented response is 20 and 185 degrees (±5). Clearly, the model is capable of predicting the suboptimal balancer performance. Here, the steady-state amplitude from the experimental measurement is 0.103mm while the model predicted value is 0.142mm.

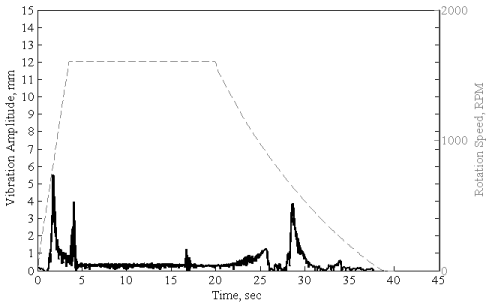

(a) Experimental system response.

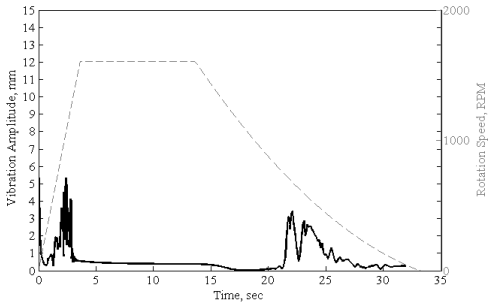

(b) Simulated system response.

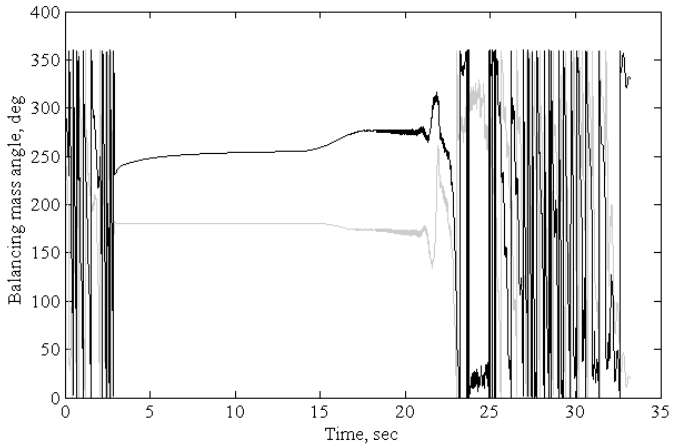

(c) Simulated balancing mass locations.

Figure 4.35: Experimental and simulated system responses (case 3, 6g imbalance mass)

Similarly, the model was able to predict correct balancing mass positions in suboptimal equilibrium. For the 6g imbalance configuration, the steady state vibration amplitude predicted by the model varied by 6% from the experimental value. The first transient state amplitude only varied by 3%, while the second transient amplitude was under predicted by 11%.

For the 12g and 14g cases, high accuracy was achieved for the first transient amplitude and the steady state. The steady state response from the model was within 3% of the experimental for both cases. The first transient amplitude was

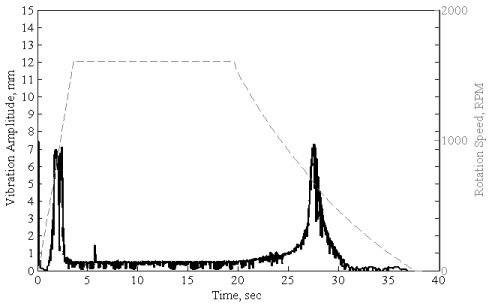

(a) Experimental system response.

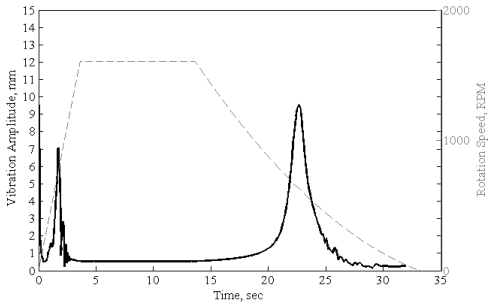

(b) Simulated system response.

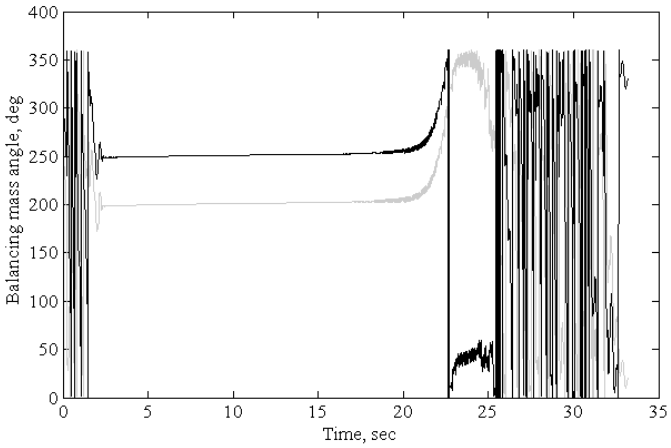

(c) Simulated balancing mass locations.

Figure 4.36: Experimental and simulated system responses (case 3, 12g imbalance mass)

within 1% for the 12g imbalance load and 22% over predicted for the 14g case. The second transient amplitude did not share the same accuracy; both simulations over predicted by 30% and 40% respectively.

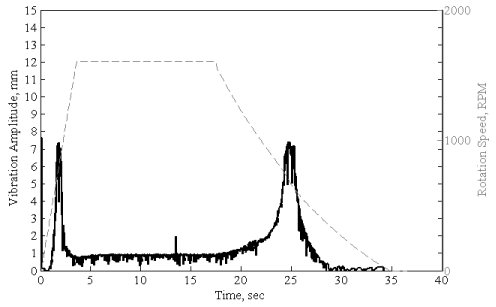

(a) Experimental system response.

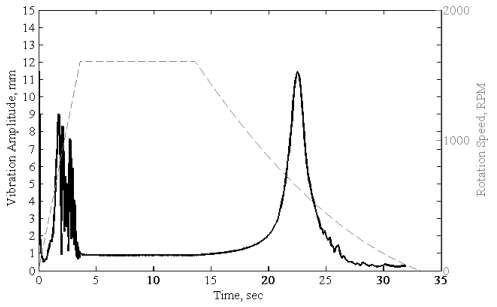

(b) Simulated system response.

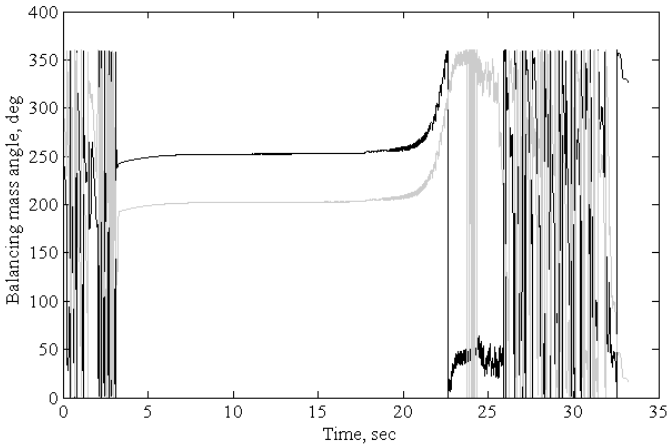

(c) Simulated balancing mass locations.

Figure 4.37: Experimental and simulated system responses (case 3, 14g imbalance mass)

4.4 Comparison of Model Cases

From the conventional viscous damping model and new friction model, predictions from numerical simulations were presented in this section. The predicted steady state vibration amplitudes from the experiment and model cases are presented in Figure 4.38. The dots in the plot represent the experimental data while the lines and dashed lines are the various model predictions. Overall, only the case with significant friction contribution (case 3) captured the trend in passive balancer performance at low imbalance mass. The other two model cases and the reference model were inadequate in predicting the complete balancer performance.

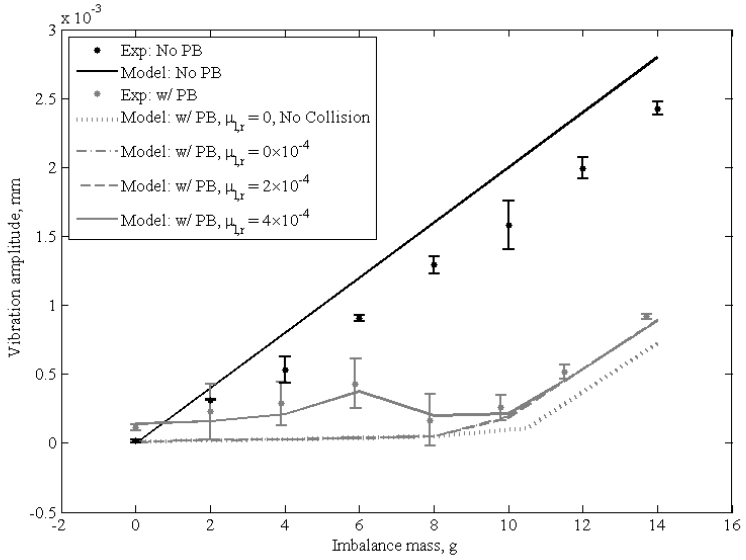

Figure 4.38: Vibration amplitude from experimental and numerically predicted data.

A detailed accuracy study of the different model cases is given in Tables 4.5 and 4.6. The overall accuracy of the model cases was derived by averaging the absolute value of the percent margin of error at each imbalance mass increment.

The result confirms that case 3 is the most accurate in predicting passive balancer performance with an accuracy of 17.55%. Case 1 and 2 share similar accuracy at 58.14% and 58.99% accuracy respectively. The reference case which lacked friction and balancing mass collisions was shown to have a margin of error of 67.67%.

Table 4.5: Steady state vibration amplitudes from experiment and passive balancing models.

Imbalance	Steady-state Vibration Amplitude, mm				
Mass, g	Experiment	Reference Case	Case 1	Case 2	Case 3
0	0.1123	0.0125	0.0125	0.0041	0.1420
2	0.2280	0.0185	0.0185	0.0271	0.1589
4	0.2871	0.0256	0.0256	0.0274	0.2082
6	0.4289	0.0374	0.0374	0.0374	0.3744
8	0.1668	0.0494	0.0494	0.0503	0.1985
10	0.2587	0.1073	0.1958	0.1847	0.2143
12	0.5160	0.3713	0.5392	0.5374	0.5356
14	0.9177	0.7220	0.8915	0.8891	0.8852

Table 4.6: Vibration amplitude accuracy of the passive balancing models.

Imbalance	Steady-state Vibration Amplitude Accuracy (%)				
Mass, g	Experiment	Reference	Case 1	Case 2	Case 3
0	–	−88.86	−88.86	−96.34	+26.40
2	–	−91.87	−91.87	−88.13	−30.32
4	–	−91.09	−91.09	−90.44	−27.48
6	–	−91.29	−91.29	−91.27	−12.70
8	–	−70.38	−70.38	−69.84	+19.02
10	–	−58.53	−24.32	−28.61	−17.17
12	–	−28.04	+4.49	+4.14	+3.79
14	–	−21.32	−2.85	−3.11	−3.54
Mean margin of error::		67.67%	58.14%	58.99%	17.55%

The model presented in case 3 is clearly the most accurate. It is at least 3.3 times more accurate than all the other models presented. The accuracy of the models is visualized in Figures 4.39 and 4.40. The lines in Figure 4.39 represent the value of the difference between what each model predicted and the experimental value while the lines in Figure 4.40 are the percent error for each model in each imbalance case. Of all cases, the model with friction and collision provided the least error–amplitude and percentage wise.

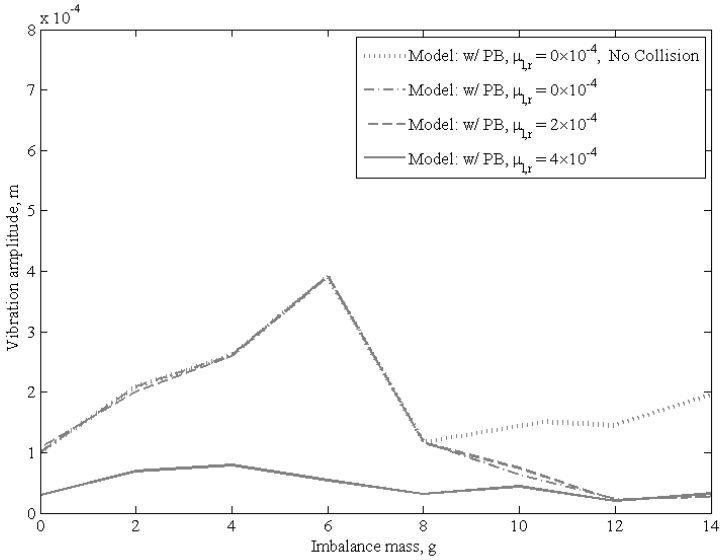

Figure 4.39: Discrepancy between predicted and experimental vibration amplitudes by the different models.

The effect friction has on balancer performance can be seen in the simulation results presented in Figures 4.41 and 4.42. The final steady state positions of the balancing masses are shown in Figure 4.41 according to the different model cases. In the reference case and cases 1 and 2, the masses assume the perfect balancing positions indicating the low or non-existent friction. On the other hand, case 3 results clearly show that the balancing masses do not assume perfect balancing

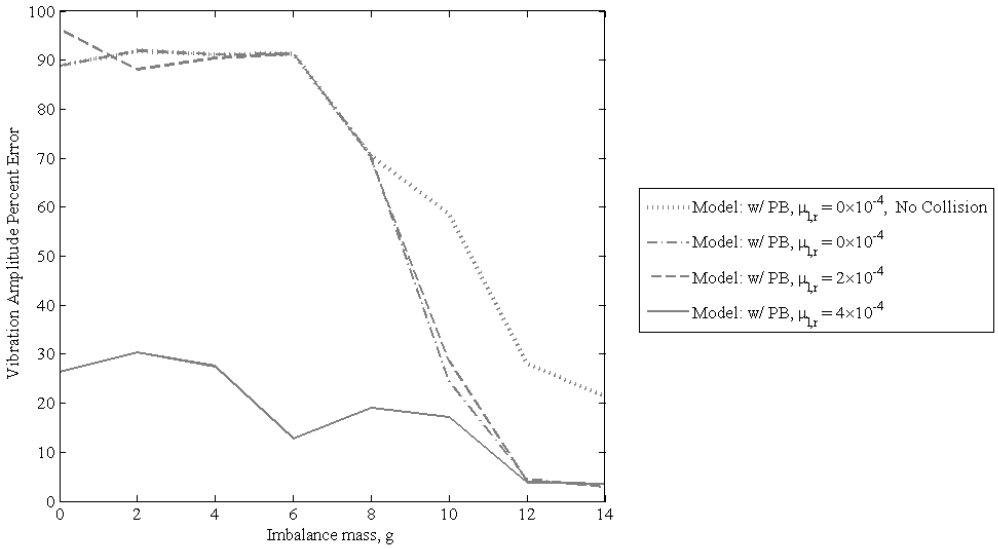

Figure 4.40: Percent error between predicted and experimental vibration amplitudes by the different models.

positions, but, rather, they assume positions around the equilibrium.

The effect can also be seen in Figure 4.42 where the angular position difference between the balancing mass is plotted. At low imbalance, namely, 0g, the balancing masses assume positions 180 degrees apart in all cases but case 3. This negates any imbalance the masses might introduce since they counter the forces themselves. The masses in case 3 do not assume positions 180 degrees apart, thus, introducing residual vibrations due to their positions.

The effect of balancing mass collision can be seen in Figures 4.41 and 4.41. The model prediction of the reference case which ignores balancer mass collision predicted the masses would be 0 degrees apart. This improved the balancing performance since the centrifugal force vector of both masses points exactly away from the imbalance mass. However, this is not possible in most balancer designs since the balancing masses would encounter one another and collide.

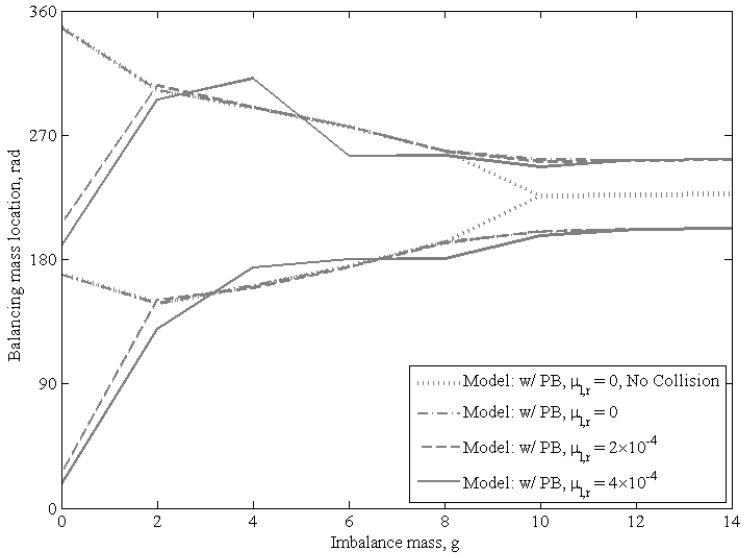

Figure 4.41: Balancing mass angles under different friction conditions.

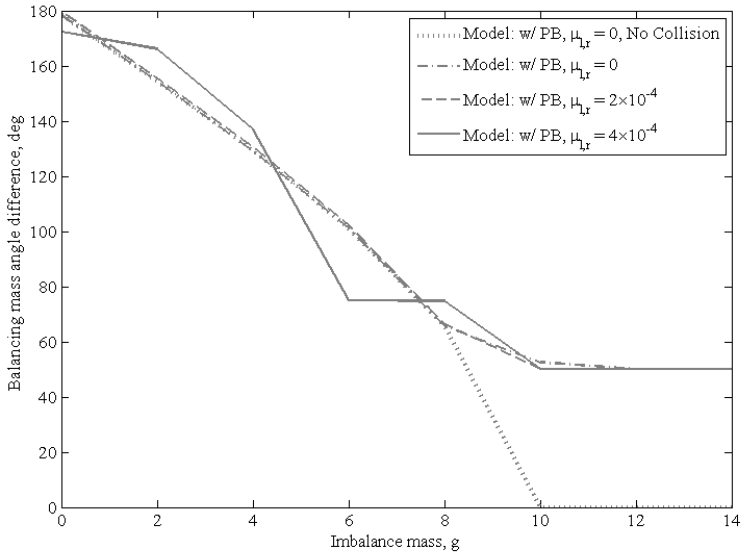

Figure 4.42: Angle difference between the balancing masses.

Chapter 5 | Conclusions and Recommendations for Future Work

5.1 Concluding Remarks

This chapter summarizes the work done and reported on in this thesis. Comments on the current state of research as well as future work recommendations are discussed.

5.1.1 Mathematical Model

The first part of this research provided a comprehensive physics-based model to describe the dynamic passive balancing behavior in supercritical shafts. The equations of motion were derived in three dimensional space using Lagrange's equation. The shaft was allowed to bend and twist in three dimensions to account for non-planar effects such as the teetering of shaft elements. No restrictions were placed on the shaft speed other than being a function of time. This allows for the study of speed varying scenarios such as transient responses due to acceleration or

declaration of the shaft. In addition, gravity and rotational inertia were considered in the model. The model accounts for the shaft in any orientation with respect to the ground.

Great detail went in the passive balancer model presented in this work. Many dynamic effects that are usually ignored in passive balancing studies or not deployed comprehensively with other effects were considered in this model. The mathematical tools provided could model multiple balancers with multiple balancing masses in each all in the same system. A novel model for the static rolling resistance was also provided. Only experiments or steady state analysis previously showed the effects of friction on the passive balancer performance. This model is capable of simulating full system responses with friction taken into account.

Another detail in the passive balancer that was not ignored is the collision of balancing masses within the balancer track. Nearly all passive balancing studies forfeit the effects of the balancing masses impacting during operation. First, this ignores a significant source of energy dissipation which may lead to inaccurate results. And, also, models that ignore balancing mass collisions achieves better balancing performance that possible physically. This is due to the balancing masses colliding at the equilibrium position and not being able to at the same perfect balancing location. The model also includes viscous damping effects between the balancing mass and balancer track.

Mathematical formulations for other shaft elements were provided as well. A dashpot/spring model was provided to add addition stiffness or damping into the system. A hub model with n elastic blades was discussed. Different types of imbalance masses were also detailed. The model is not limited to any configuration

of the elements provided besides the need for a rotor such as a shaft.

5.1.2 Experiments Summary

A test rig was devised to experimentally determine the realistic passive balancing performance in rotating shafts. Several measurement devices were used to characterize the system performance under each configuration. Several conclusions can be drawn from the experimental work conducted here:

1. The passive balancing device reduced vibration for all configurations except the already balanced configuration.

2. There exists residual vibrations introduced by the passive balancing device at low imbalance mass. This was shown in the model to be due to rolling resistance.

3. The final position of the balancing masses is not reliable in regions where the balancer possesses suboptimal performance

4. The balancing masses assume steady-state positions within seconds past the first natural mode. If the steady-state rotational velocity is high enough, the balancing masses assume the equilibrium positions before the shaft reaches the steady-state velocity.

5. In some cases, the balancing masses reduced transient response but, typically, caused an increase.

The vibration suppression performance of the passive balancer is summarized in Table 5.1. Saturation of the balancing potential is reached by 10g of imbalance

mass. This means that the balancing masses are providing the most balancing possible which is limited by their mass and radial distance from the center of the shaft.

Table 5.1: Experimental vibration suppression performance of passive balancer.

Imbalance Mass, g	Vibration Reduction, %
0	+0.112 mm
2	−27.40%
4	−46.03%
6	−52.67%
8	−87.10%
10	−83.63%
12	−74.13%
14	−62.18%

5.1.3 Model Validation

The model presented in this thesis was able to accurately capture performance of the passive balancing device. Three cases were suggested and studied. The first case relied only on viscous damping as the means of energy dissipation in the passive balancer. This is heavily assumed in most studies on passive balancing. The comparison of this case with the experiment showed that it is predicting the balancer performance with 58.14% error. The second case studied was with some additional friction which proved not enough to represent the system. This case shared a similar accuracy to the first case with 58.99% error.

The last case studied was with higher rolling resistance. This proved to be capable of accurately predicting balancer performance. This is clearly demonstrated

in Figure 5.1. The solid line represents the predictions made with this case. The model in this configuration was able to predict balancer performance within 17.55% error. This is a major improvement over the other cases.

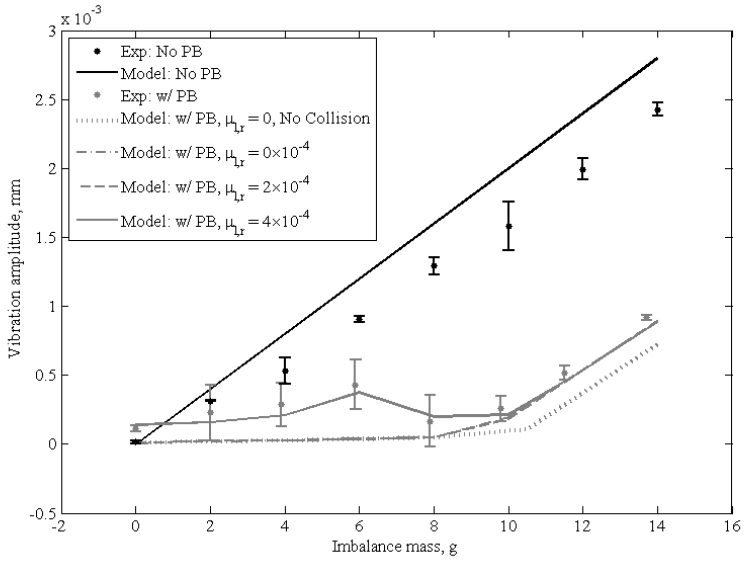

Figure 5.1: Vibration amplitude from experimental and numerically predicted data.

A graphical comparison between all the models discussed in this thesis is presented in Figure 5.2. It can be seen that with the addition of complex effects, the accuracy of passive balancer performance predictions was significantly improved. From the least complex model presented here (A) to the most advanced (D), the accuracy of model predictions was improved by a factor of 3.86.

The accomplished of the validated model can be summarized:

1. With the addition of inelastic collision between the balancing masses, the accuracy of the predicted results was improved by 16.39% overall and by a factor of 6.7 times in the high imbalance configurations (24.68% vs. 3.67%).

2. With the addition of friction in the form of rolling resistance to the model,

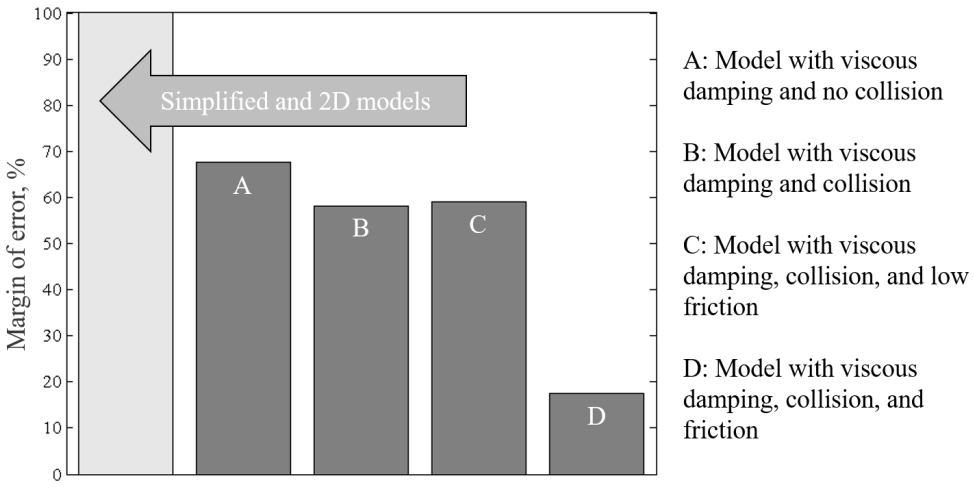

Figure 5.2: Passive balancer model accuracy.

the accuracy of the predicted results was improved by a factor of 3.31 (58.14% vs. 17.55%).

3. The comprehensive model presented in this work, which includes both friction and mass collisions, improved the overall accuracy of predicted results by a factor 3.86 (67.67% vs. 17.55%).

4. The proposed model produced predicted values with a mean 17.55% margin of error when compared to experimental values. The model was able to predict the degraded performance of the passive balancer due to friction. It adequately accounts for balancing mass interaction with other balancing masses and the balancer track.

Several other conclusions can be made on the state of passive balancer modeling. The key points based on the model formulation and the results of the model validation are:

1. Collision between balancing masses should not be ignored for improved accuracy in high imbalance scenarios.

2. Viscous damping alone does not accurately predict residual vibrations which arise from the interaction between the balancing masses and the balancer track.

3. The residual vibrations due to the passive balancing device can be predicted using the friction model presented in this report.

4. The model presented in this work is capable of accurately representing the dynamics of passive balancing devices for rotary systems.

5.2 Recommendations for Future Work

5.2.1 Parameter Optimization

For future work, it is recommended to design balancers with the effects of friction in mind. It was demonstrated here experimentally and analytically that friction degrades the performance of a passive balancing device in the presence of low imbalanced hubs. The first step to addressing this issue is determining the rolling resistance coefficient and coefficient of restitution experimentally. This should be done for various materials to optimize the design and avoid excessive degradation of passive balancing performance.

Other parameters such as the location of the passive balancer or the number of passive balancers should be investigated with the comprehensive model provided here. An optimized placement of the passive balancing device could result in increased balancing performance. Finally, special attention should be paid to the boundary conditions of the rotor. It plays a significant role in the prediction and analysis process.

5.2.2 Balancer Design

It is recommended to further study the passive balancer design to eliminate or reduce some of the inherent side effects of passive balancing. Suggested improvements to the balancer design are shown in Figure 5.3. A partitioned track (shown in Figure 5.3a) may reduce the transient response of the balancing masses and narrow the band where limit cycles are prevalent. The channeled design (shown in Figure 5.3b) should be given heavy consideration as well since it can reduce the negative effects of friction in the passive balancer.

Both modeling and experimental efforts should be exerted to accomplish better balancing performance. The model provided in this thesis can adequately represent the channeled balancer design. With small modification, the model could be used to predict the performance of the partitioned balancer design. The model provided here is a great tool to optimize system parameters and balancer design.

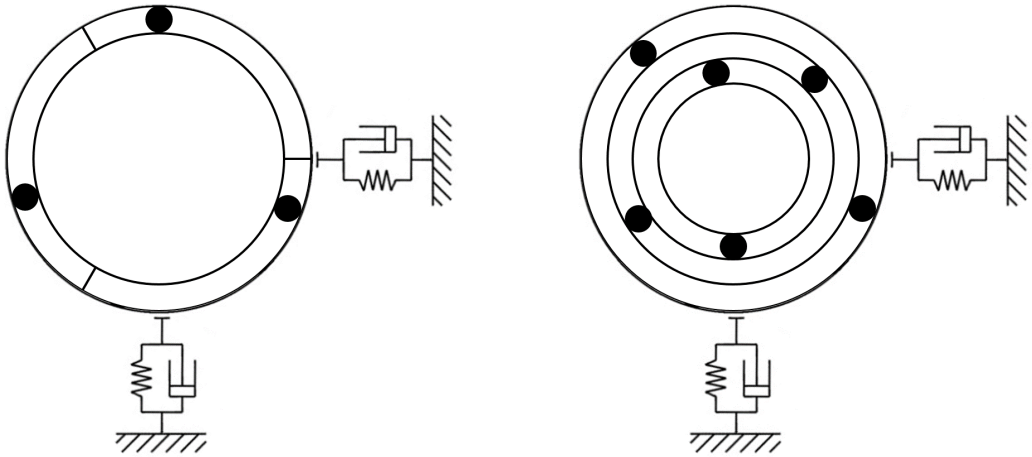

(a) Partitioned ball-type passive balancing device.

(b) A ball-type passive balancing device with multiple tracks.

Figure 5.3: Suggested balancer designs for future work.

5.2.3 Target Applications

There is a vast number of applications that passive balancing is applicable to. The lack of a power requirement and general simplicity of implementation makes passive balancing an attractive option for vibration suppression. Rotor craft implementation analysis is recommended as future work. Helicopters are prone to hub vibrations due to an uneven mass distribution in the rotor plane. A passive balancing device could potentially eliminate the need for manual track and balance for helicopter blades in addition to providing unpowered vibration suppression during vehicle operation. Similarly, a study should be conducted on passive balancing in turbo machinery.

5.2.4 Model Improvements

The model could be improved by studying the effects of external loads in more detail. For instance, external shaft or system impacts can be modeled to study the response of the passive balancer. In some cases, an operating rotary machine is subjected to external loads in the process of normal operation. One example is hand held power tools where contact is made with objects outside of the system. In helicopters, a more detailed aerodynamic model would be coupled with the model presented here to judge the performance of a mounted passive balancing device.

Other improvements to the model could be allowing for the partitioning of the shaft to allow for multiple boundary conditions. This would increase the complexity of the model and allow for more accurate representation of some systems where the rotor is bounded at several locations.

Appendix

Analytical Derivations of Various Mode Shapes

1 Normal Modes

1.1 Beam Bending

$$U_{bend} = \int_0^L \frac{1}{2} EI(y'')^2 \mathrm{d}x \tag{.1}$$

$$T_{bend} = \int_0^L \frac{1}{2} \mu \dot{y}^2 \mathrm{d}x \tag{.2}$$

$$\mathcal{L} = T_{bend} - U_{bending} = \int_0^L \left[\frac{1}{2} \mu \dot{y}^2 - \frac{1}{2} EI(y'')^2 \right] \mathrm{d}x \tag{.3}$$

$$\delta W_{NC} = 0 \tag{.4}$$

$$\delta \int_{t_1}^{t_2} \mathcal{L} \mathrm{d}t = - \int_{t_1}^{t_2} \delta W_{NC} \mathrm{d}t \tag{.5}$$

$$\delta \int_{t_1}^{t_2} \int_0^L \left[\frac{1}{2} \mu \dot{y}^2 - \frac{1}{2} EI (y'')^2 \right] \mathrm{d}x \mathrm{d}t = 0 \tag{.6}$$

$$\int_{t_1}^{t_2} \int_0^L \left[\mu \dot{y} \delta \dot{y} - EI y'' \delta y'' \right] \mathrm{d}x \mathrm{d}t = 0 \tag{.7}$$

$$\int_{t_1}^{t_2} \int_0^L \mu \dot{y} \delta \dot{y} \mathrm{d}x \mathrm{d}t = \int_0^L \int_{t_1}^{t_2} \mu \dot{y} \delta \dot{y} \mathrm{d}x \mathrm{d}t \tag{.8}$$

$$\int_0^L \int_{t_1}^{t_2} \mu \dot{y} \delta \dot{y} \mathrm{d}x \mathrm{d}t = \int_0^L \left\{ \left[\mu \dot{y} \delta y \right]_{t=t_1}^{t=t_2} - \int_{t_1}^{t_2} \mu \ddot{y} \delta y \mathrm{d}t \right\} \mathrm{d}x = - \int_{t_1}^{t_2} \mu \ddot{y} \delta y \mathrm{d}t \mathrm{d}x \tag{.9}$$

$$\int_{t_1}^{t_2} \int_0^L - EI y'' \delta y'' \mathrm{d}x \mathrm{d}t = \int_{t_1}^{t_2} \left\{ - \left[EI y'' \delta y' \right]_{x=0}^{x=L} + \int_0^L (EI y'')' \delta y' \mathrm{d}x \right\} \mathrm{d}t \tag{.10}$$

$$\begin{aligned} &\int_{t_1}^{t_2} \int_0^L - EI y'' \delta y'' \mathrm{d}x \mathrm{d}t = \\ &\int_{t_1}^{t_2} \left\{ - \left[EI y'' \delta y' \right]_{x=0}^{x=L} + \left[(EI y'')' \delta y \right]_{x=0}^{x=L} - \int_0^L (EI y'')'' \delta y \mathrm{d}x \right\} \mathrm{d}t \end{aligned} \tag{.11}$$

$$\int_{t_1}^{t_2}\left\{\int_0^L\left[-\mu\ddot{y}-(EIy'')''\right]\delta y\mathrm{d}x-EIy''(L)\delta y'(L)+EIy''(0)\delta y'(0)\right\}\mathrm{d}t \\ +\int_{t_1}^{t_2}\left\{(EIy''(L))'\delta y(L)-(EIy''(0))'\delta y(0)\right\}\mathrm{d}t=0 \tag{.12}$$

$$EIy''''+\mu\ddot{y}=0 \tag{.13}$$

$$\begin{aligned} EIy''(L)=0 \quad or \quad \delta y'(L)=0 \\ EIy''(0)=0 \quad or \quad \delta y'(0)=0 \\ EIy'''(L)=0 \quad or \quad \delta y(L)=0 \\ EIy'''(0)=0 \quad or \quad \delta y(0)=0 \end{aligned} \tag{.14}$$

$$y(x,t)=Y(x)e^{iwt} \tag{.15}$$

$$EIY''''-\mu w^2=0 \tag{.16}$$

$$Y''''-\sigma^4 Y=0 \tag{.17}$$

$$\sigma^4=\frac{\mu w^2}{EI} \tag{.18}$$

$$Y(x)=C_1\sin(\sigma x)+C_2\cos(\sigma x)+C_3\sinh(\sigma x)+C_4\cosh(\sigma x) \tag{.19}$$

$$
\begin{aligned}
Y'(x) &= C_1\sigma\cos(\sigma x) - C_2\sigma\sin(\sigma x) + C_3\sigma\cosh(\sigma x) + C_4\sigma\sinh(\sigma x) \\
Y''(x) &= -C_1\sigma^2\sin(\sigma x) - C_2\sigma^2\cos(\sigma x) + C_3\sigma^2\sinh(\sigma x) + C_4\sigma^2\cosh(\sigma x) \\
Y'''(x) &= -C_1\sigma^3\cos(\sigma x) + C_2\sigma^3\sin(\sigma x) + C_3\sigma^3\cosh(\sigma x) + C_4\sigma^3\sinh(\sigma x)
\end{aligned}
\tag{.20}
$$

1.1.1 Cantilever Beam

$$
\begin{aligned}
\delta y(0) &= 0 \\
\delta y'(0) &= 0 \\
EIy''(L) &= 0 \\
EIy'''(L) &= 0
\end{aligned}
\tag{.21}
$$

$$
\begin{aligned}
\delta y(0) &= 0 = C_2 + C_4 \\
\delta y'(0) &= 0 = C_1 + C_3 \\
EIy''(L) &= 0 = -C_1\sin(\sigma L) - C_2\cos(\sigma L) + C_3\sinh(\sigma L) + C_4\cosh(\sigma L) \\
EIy'''(L) &= 0 = -C_1\cos(\sigma L) + C_2\sin(\sigma L) + C_3\cosh(\sigma L) + C_4\sinh(\sigma L)
\end{aligned}
\tag{.22}
$$

$$
\begin{bmatrix}
0 & 1 & 0 & 1 \\
1 & 0 & 1 & 0 \\
-\sin(\sigma L) & -\cos(\sigma L) & \sinh(\sigma L) & \cosh(\sigma L) \\
-\cos(\sigma L) & \sin(\sigma L) & \cosh(\sigma L) & \sinh(\sigma L)
\end{bmatrix}
\tag{.23}
$$

$$\det \begin{bmatrix} 0 & 1 & 0 & 1 \\ 1 & 0 & 1 & 0 \\ -\sin(\sigma L) & -\cos(\sigma L) & \sinh(\sigma L) & \cosh(\sigma L) \\ -\cos(\sigma L) & \sin(\sigma L) & \cosh(\sigma L) & \sinh(\sigma L) \end{bmatrix} = 0 \tag{.24}$$

$$1 + \cos(\sigma L)\cosh(\sigma L) = 0 \tag{.25}$$

$$\sigma L = 1.8751, 4.6941, 7.8548, 10.996, 14.137, ... \tag{.26}$$

$$Y_n(x) = C_1 \sin(\sigma_n x) + C_2 \cos(\sigma_n x) + C_3 \sinh(\sigma_n x) + C_4 \cosh(\sigma_n x) \tag{.27}$$

$$\begin{gathered} C_4 = -C_2 \\ C_3 = -C_1 \\ C_1\left(-\sin(\sigma_n L) - \sinh(\sigma_n L)\right) + C_2\left(-\cos(\sigma_n L) - \cosh(\sigma_n L)\right) = 0 \\ C_2 = \tfrac{\sin(\sigma_n L)+\sinh(\sigma_n L)}{\cos(\sigma_n L)+\cosh(\sigma_n L)} C_1 \end{gathered} \tag{.28}$$

$$\begin{aligned} Y_n(x) = C_1\{&\sin(\sigma_n x) - \sinh(\sigma_n x) \\ &+ \frac{\sin(\sigma_n L) + \sinh(\sigma_n L)}{\cos(\sigma_n L) + \cosh(\sigma_n L)}(\cos(\sigma_n x) - \cosh(\sigma_n x))\} \end{aligned} \tag{.29}$$

1.1.2 Fixed-fixed Beam

$$\begin{aligned} \delta y(0) &= 0 \\ \delta y'(0) &= 0 \\ \delta y(L) &= 0 \\ \delta y'(L) &= 0 \end{aligned} \tag{.30}$$

$$\begin{aligned} \delta y(0) &= 0 = C_2 + C_4 \\ \delta y'(0) &= 0 = C_1 + C_3 \\ \delta y(L) &= 0 = C_1 \sin(\sigma L) + C_2 \cos(\sigma L) + C_3 \sinh(\sigma L) + C_4 \cosh(\sigma L) \\ \delta y'(L) &= 0 = C_1 \sigma \cos(\sigma L) - C_2 \sigma \sin(\sigma L) + C_3 \sigma \cosh(\sigma L) + C_4 \sigma \sinh(\sigma L) \end{aligned} \tag{.31}$$

$$\begin{bmatrix} 0 & 1 & 0 & 1 \\ 1 & 0 & 1 & 0 \\ \sin(\sigma L) & \cos(\sigma L) & \sinh(\sigma L) & \cosh(\sigma L) \\ \cos(\sigma L) & -\sin(\sigma L) & \cosh(\sigma L) & \sinh(\sigma L) \end{bmatrix} \tag{.32}$$

$$\det \begin{bmatrix} 0 & 1 & 0 & 1 \\ 1 & 0 & 1 & 0 \\ \sin(\sigma L) & \cos(\sigma L) & \sinh(\sigma L) & \cosh(\sigma L) \\ \cos(\sigma L) & -\sin(\sigma L) & \cosh(\sigma L) & \sinh(\sigma L) \end{bmatrix} = 0 \tag{.33}$$

$$\cos(\sigma L) \cosh(\sigma L) = 1 \tag{.34}$$

$$\sigma L = \begin{bmatrix} 4.730040744862704 \\ 7.853204624095837 \\ 10.995607838001670 \\ 14.137165491257464 \\ 17.278759657399480 \\ 20.420352245626059 \\ 23.561944902040455 \\ 26.703537555508188 \\ 29.845130209103253 \\ 32.986722862692822 \\ 36.128315516282619 \\ 39.269908169872416 \\ 42.411500823462198 \\ 45.553093477052002 \\ 48.694686130641799 \end{bmatrix} \tag{.35}$$

$$Y_n(x) = C_1 \sin(\sigma_n x) + C_2 \cos(\sigma_n x) + C_3 \sinh(\sigma_n x) + C_4 \cosh(\sigma_n x) \tag{.36}$$

$$
\begin{aligned}
C_4 &= -C_2 \\
C_3 &= -C_1 \\
(\sin(\sigma L) - \sinh(\sigma L))C_1 &+ (\cos(\sigma L) - \cosh(\sigma L))C_2 = 0 \\
C_2 &= -\frac{(\sin(\sigma L) - \sinh(\sigma L))}{(\cos(\sigma L) - \cosh(\sigma L))}C_1
\end{aligned}
\tag{.37}
$$

$$
\begin{aligned}
Y_n(x) = C_1\{&\sin(\sigma_n x) - \sinh(\sigma_n x) \\
&+ \frac{(\sin(\sigma_n L) - \sinh(\sigma_n L))}{(\cos(\sigma_n L) - \cosh(\sigma_n L))}(\cosh(\sigma_n x) - \cos(\sigma_n x))\}
\end{aligned}
\tag{.38}
$$

1.1.3 Fixed-pinned Beam

$$
\begin{aligned}
\delta y(0) &= 0 \\
\delta y'(0) &= 0 \\
\delta y(L) &= 0 \\
\delta y'(L) &= 0
\end{aligned}
\tag{.39}
$$

$$
\begin{aligned}
\delta y(0) = 0 &= C_2 + C_4 \\
\delta y'(0) = 0 &= C_1 + C_3 \\
\delta y(L) = 0 &= C_1(\sinh(\sigma L) - \sin(\sigma L)) + C_2(\cosh(\sigma L) - \cos(\sigma L)) \\
\delta y''(L) = 0 &= C_1\sigma^2(\sinh(\sigma L) + \sin(\sigma L)) + C_2\sigma^2(\cosh(\sigma L) + \cos(\sigma L))
\end{aligned}
\tag{.40}
$$

$$
\det \begin{bmatrix} \sinh(\sigma L) - \sin(\sigma L) & \cosh(\sigma L) - \cos(\sigma L) \\ \sinh(\sigma L) + \sin(\sigma L) & \cosh(\sigma L) + \cos(\sigma L) \end{bmatrix} = 0 \tag{.41}
$$

$$\tanh(\sigma L) - \tanh(\sigma L) = 0 \tag{.42}$$

$$\sigma L = \begin{bmatrix} 3.926602312047919 \\ 7.068582745628732 \\ 10.210176122813031 \\ 13.351768777754094 \\ 16.493361431346408 \\ \cdots \\ \pi(n + 1/4) \end{bmatrix}, n = 1, 2, 3, \ldots \tag{.43}$$

$$\begin{aligned} Y_n(x) = C_1\{&\sinh(\sigma_n x) - \sin(\sigma_n x) \\ &- \frac{(\sinh(\sigma_n L) + \sin(\sigma_n L))}{(\cosh(\sigma_n L) + \cos(\sigma_n L))}(\cosh(\sigma_n x) - \cos(\sigma_n x))\} \end{aligned} \tag{.44}$$

1.2 Beam Torsion

$$U_{torsion} = \int_0^L \int_A \frac{1}{2} G(\mu\phi')^2 \mathrm{d}A\mathrm{d}x \tag{.45}$$

$$U_{torsion} = \int_0^L \frac{1}{2} GJ(\phi')^2 \mathrm{d}x \tag{.46}$$

$$T_{torsion} = \int_0^L \frac{1}{2} \mu\dot{\phi}^2 \mathrm{d}x \tag{.47}$$

$$\mathcal{L} = T_{torsion} - U_{torsion} = \int_0^L \left[\frac{1}{2}\mu\dot{\phi}^2 - \frac{1}{2}GJ(\phi')^2\right] \mathrm{d}x \tag{.48}$$

$$\delta W_{NC} = 0 \tag{.49}$$

$$\delta \int_{t_1}^{t_2} \mathcal{L} \mathrm{d}t = - \int_{t_1}^{t_2} \delta W_{NC} \mathrm{d}t \tag{.50}$$

$$\delta \int_{t_1}^{t_2} \int_0^L \left[\frac{1}{2} \mu \dot{\phi}^2 - \frac{1}{2} GJ (\phi')^2 \right] \mathrm{d}x \mathrm{d}t = 0 \tag{.51}$$

$$\int_{t_1}^{t_2} \int_0^L \left[\mu \dot{\phi} \delta \dot{\phi} - GJ \phi' \delta \phi' \right] \mathrm{d}x \mathrm{d}t = 0 \tag{.52}$$

$$\int_{t_1}^{t_2} \int_0^L \mu \dot{\phi} \delta \dot{\phi} \mathrm{d}x \mathrm{d}t = \int_0^L \int_{t_1}^{t_2} \mu \dot{\phi} \delta \dot{\phi} \mathrm{d}x \mathrm{d}t \tag{.53}$$

$$\begin{aligned} \int_0^L \int_{t_1}^{t_2} \mu \dot{\phi} \delta \dot{\phi} \mathrm{d}x \mathrm{d}t &= \int_0^L \left\{ \left[\mu \dot{\phi} \delta \phi \right]_{t=t_1}^{t=t_2} - \int_{t_1}^{t_2} \mu \ddot{\phi} \delta \phi \mathrm{d}t \right\} \mathrm{d}x \\ &= - \int_{t_1}^{t_2} \mu \ddot{\phi} \delta \phi \mathrm{d}t \mathrm{d}x \end{aligned} \tag{.54}$$

$$\int_{t_1}^{t_2} \int_0^L -GJ \phi' \delta \phi' \mathrm{d}x \mathrm{d}t = \int_{t_1}^{t_2} \left\{ - \left[GJ \phi' \delta \phi \right]_{x=0}^{x=L} + \int_0^L (GJ \phi'') \delta \phi \mathrm{d}x \right\} \mathrm{d}t \tag{.55}$$

$$\int_{t_1}^{t_2} \left\{ \int_0^L \left[-\mu \ddot{\phi} + GJ \phi'' \right] \delta \phi \mathrm{d}x - GJ \phi'(L) \delta \phi(L) + GJ \phi'(0) \delta \phi(0) \right\} \mathrm{d}t \tag{.56}$$

$$GJ\phi'' - \mu\ddot{\phi} = 0 \tag{.57}$$

$$\begin{aligned} GJ\phi'(L) = 0 \quad or \quad \delta\phi(L) = 0 \\ GJ\phi'(0) = 0 \quad or \quad \delta\phi(0) = 0 \end{aligned} \tag{.58}$$

$$\phi(x,t) = \Phi(x)e^{iwt} \tag{.59}$$

$$GJ\Phi'' + \mu w^2\Phi = 0 \tag{.60}$$

$$\Phi'' + \kappa^2\Phi = 0 \tag{.61}$$

$$\kappa^2 = \frac{\mu w^2}{GJ} \tag{.62}$$

$$\Phi(x) = C_1 \sin(\kappa x) + C_2 \cos(\kappa x) \tag{.63}$$

$$\Phi'(x) = C_1\kappa \cos(\kappa x) - C_2\kappa \sin(\kappa x) \tag{.64}$$

1.2.1 Cantilever Beam

$$\begin{aligned} GJ\phi'(L) = 0 \\ \delta\phi(0) = 0 \end{aligned} \tag{.65}$$

$$\begin{aligned} \delta\phi(0) &= 0 = C_2 \\ GJ\delta\phi'(L) &= 0 = C_1\kappa\cos(\kappa L) \end{aligned} \tag{.66}$$

$$\cos(\kappa L) = 0 \tag{.67}$$

$$\kappa L = \frac{\pi}{2}(2n+1), n = 1, 2, 3, ... \tag{.68}$$

$$\Phi_n(x) = C_1 \sin(\kappa_n x) \tag{.69}$$

Bibliography

[1] Kunz, D. L. and M. C. Newkirk (2009) "A Generalized Dynamic Balancing Procedure for the AH-64 Tail Rotor," *Journal of Sound and Vibration*, **326**(1-2), pp. 353–366.

[2] Frothingham, R. (1999) "Centrifugation without a balance tube," *American Biotechnology Laboratory*, **17**(3), p. 84.

[3] Cubberly, W. and R. Bakerjian (1989) *Tool and Manufacturing Engineers Handbook*, desk ed., Dearborn, Michigan.

[4] Soltis, J., J. Palacios, D. Wolfe, and T. Eden (2013) "Evaluation of Ice Adhesion Strength on Erosion Resistant Materials," in *54th AIAA/ASME/ASCE/AHS/ASC Structures, Structural Dynamics, and Materials Conference*, Structures, Structural Dynamics, and Materials and Co-located Conferences, American Institute of Aeronautics and Astronautics.

[5] Palazzolo, A. B., S. Jagannathan, A. F. Kascak, G. T. Montague, and L. J. Kiraly (1993) "Hybrid Active Vibration Control of Rotorbearing Systems Using Piezoelectric Actuators," *Journal of Vibration and Acoustics*, **115**(January 1993), pp. 111–119.

[6] Carmignani, C., P. Forte, and E. Rustighi (2001) "Active Control of Rotor Vibrations By Means of Piezoelectric," in *ASME 2001 Design Engineering Technical Conferences and Computers and Information in Engineering Conference*, Pittsburgh, Pa, pp. 1–8.

[7] Knospe, C. R., R. W. Hope, S. M. Tamer, and S. J. Fedigan (1995) "Robustness of Adaptive Unbalance Control of Rotors with Magnetic Bearings," *Journal of Vibration and Control*, **2**(1), pp. 33–52.

[8] Santos, I. F. and F. H. Russo (1998) "Tilting-Pad Journal Bearings With Electronic Radial Oil Injection," *Journal of Tribology*, **120**(3), p. 583.

[9] Zeidan, F. Y., L. San Andres, and J. M. Vance (1996) "Design and application of squeeze film dampers in rotating machinery," in *25th Turbomachinery Symposium*, Houston, Texas, pp. 169–188.

[10] Wang, J., N. Feng, G. Meng, and E. J. Hahn (2006) "Vibration Control of Rotor by Squeeze Film Damper with Magnetorheological Fluid," *Journal of Intelligent Material Systems and Structures*, **17**(April), pp. 353–357.

[11] Van de Vegte, J. (1981) "Balancing of flexible rotors during operation," *Journal of Mechanical Engineering Science*, **23**(5), pp. 257–261.

[12] Blanco-Ortega, A., F. Beltran-Carbajal, A. Favela-Contreras, and G. Silva-Navarro (2008) "Active disk for automatic balancing of rotor-bearing sytems," in *American Control Conference*, Seattle, Washington, pp. 3023–3028.

[13] Hredzak, B. and G. Guo (2006) "Adjustable Balancer With Electromagnetic Release of Balancing Members," *IEEE TRANSACTIONS ON MAGNETICS*, **42**(5), pp. 1591–1596.

[14] Blanco-Ortega, A., F. Beltran-Carbajal, G. Silva-Navarro, and M. A. Oliver-Salazar (2010) "Active vibration control of a rotor-bearing system based on dynamic stiffness," *Revista Facultad De Ingenieria-Universidad De Antioquia*, (55), pp. 125–133.

[15] Muszynska, A., W. D. Franklin, and D. E. Bently (1988) "Rotor Active "Anti-Swirl" Control," *Journal of Vibration, Acoustics, Stress, and Reliability in Design*, **110**, pp. 143–150.

[16] Jalili, N. (2002) "A Comparative Study and Analysis of Semi-Active Vibration-Control Systems," *Journal of Vibration and Acoustics*, **124**(4), p. 593.

[17] Karnopp, D., M. J. Crosby, and R. a. Harwood (1974) "Vibration Control Using Semi-Active Force Generators," *Journal of Engineering for Industry*, **96**(2), p. 619.

[18] Zhu, C.-s. (2003) "A disc-type magneto-rheologic fluid damper," *Journal of Zhejiang University Science*, **4**(5), pp. 514–519.

[19] Onoda, J., T. Sanot, and K. Kamiyama (1992) "Active, Passive, and Semiactive Vibration Suppression by Stiffness Variation," *AIAA Journal*, **30**(12), pp. 2922–2929.

[20] Liu, Y., H. Matsuhisa, and H. Utsuno (2008) "Semi-active vibration isolation system with variable stiffness and damping control," *Journal of Sound and Vibration*, **313**(1-2), pp. 16–28.

[21] Kerwin, E. M. J. (1959) "Damping of Flexural Waves by a Constrained Viscoelastic Layer," *Journal of the Acoustical Society of America*, **31**, pp. 952–962.

[22] Ellis, R. C., R. A. Fink, and R. W. Rich (1989) "Eddy current damper," *23rd Aerospace Mechanisms Symposium*, **1**, pp. 127–137, arXiv:1011.1669v3.

[23] Delprete, G. G. C., A. Tonoli, E. Rava, and L. Mazzocchetti (1994) "Analytical and Experimental Investigation of a Magnetic Radial Passive Damper," *3rd International Symposium on Magnetic Bearings*, (October 2015), pp. 255–264.

[24] Forward, R. L. (1979) "Electronic damping of vibrations in optical structures." *Applied Optics*, **18**(5), pp. 690–7.

[25] Dell'Isola, F., C. Maurini, and M. Porfiri (2004) "Passive damping of beam vibrations through distributed electric networks and piezoelectric transducers: prototype design and experimental validation," *Smart Materials and Structures*, **13**(2), pp. 299–308, 1007.1863.

[26] Becker, J., O. Fein, M. Maess, and L. Gaul (2006) "Finite element-based analysis of shunted piezoelectric structures for vibration damping," *Computers & Structures*, **84**(31-32), pp. 2340–2350.

[27] Duh, J. and W. Miao (1983) *Development of monofilar rotor hub vibration absorber*, *Tech. rep.*, NASA.

[28] Darlow, M. S., A. J. Smalley, and A. G. Parkinson (1981) "Demonstration of a Unified Approach to the Balancing of Flexible Rotors," *Journal of Engineering for Power*, **103**(80), pp. 101–107.

[29] Chao, P. C.-P., C.-K. Sung, S.-T. Wu, and J.-S. Huang (2007) "Nonplanar Modeling and Experimental Validation of a Spindle-Disk System Equipped With an Automatic Balancer System in Optical Disk Drives," *Microsystem Technologies*, **13**(8-10), pp. 1227–1239.

[30] DeSmidt, H. A. (2009) "Imbalance Vibration Suppression of a Supercritical Shaft via an Automatic Balancing Device," *Journal of Vibration and Acoustics*, **131**(August), p. 041001.

[31] Rodrigues, D. J., A. R. Champneys, M. I. Friswell, and R. E. Wilson (2008) "Automatic Two-plane Balancing for Rigid Rotors," *International Journal of Non-Linear Mechanics*, **43**, pp. 527–541.

[32] Lu, C.-J. and M.-C. Wang (2011) "Stability Analysis of a Ball-Rod-Spring Automatic Balancer," *International Journal of Mechanical Sciences*, **53**(10), pp. 846–854.

[33] Kim, T. and S. Na (2013) "New Automatic Ball Balancer Design to Reduce Transient-response in Rotor System," *Mechanical Systems and Signal Processing*, **37**(1-2), pp. 265–275.

[34] Sondergaard, R., K. Chaney, and C. E. Brennen (1990) "Measurements of Bouncing Off Flat Plate," *Journal of Applied Mechanics*, **112**(90), pp. 694–699.

[35] Johnson, C. D. (1995) "Design of Passive Damping Systems," *Journal of Vibration and Acoustics*, **117**, pp. 171–176.

[36] Weir, E. and L. Lander (2005) "Hand-Arm Vibration Syndrome," *Canadian Medical Association Journal*, **172**(8), pp. 1001–1002.

[37] Vergara, M., J.-L. Sancho, P. Rodríguez, and A. Pérez-González (2008) "Hand-Transmitted Vibration in Power Tools: Accomplishment of Standards and Users' Perception," *International Journal of Industrial Ergonomics*, **38**(9-10), pp. 652–660.

[38] Yap, F., N. Vahdati, and H. Harmoko (2006) "Design and analysis of vibration isolation systems for hard disk drives," *Journal of Magnetism and Magnetic Materials*, **303**(2), pp. e52–e56.

[39] Heo, J. W., J. T. Chung, and J. M. Park (2002) "Vibration and noise reduction of an optical disk drive by using a vibration absorber," *Ieee Transactions on Consumer Electronics*, **48**(4), pp. 874–878.

[40] Amoo, L. M. (2013) "On the design and structural analysis of jet engine fan blade structures," *Progress in Aerospace Sciences*, **60**, pp. 1–11.

[41] Rahman, M., Z. C. Ong, W. T. Chong, S. Julai, and S. Y. Khoo (2015) "Performance enhancement of wind turbine systems with vibration control: A review," *Renewable and Sustainable Energy Reviews*, **51**, pp. 43–54.

[42] Ferrer, R., T. Krysinski, P. a. Aubourg, and S. Bellizzi (2001) "New Methods for Rotor Tracking and Balance Tuning and Defect Detection Applied to Eurocopter Products," in *American Helicopter Society 57th Annual Forum*, American Helicopter Society.

[43] Nelson, G., R. Rajamani, and A. Erdman (2014) "Noise control challenges for auscultation on medical evacuation helicopters," *Applied Acoustics*, **80**, pp. 68–78.

[44] Majewski, T., D. Szwedowicz, and A. H. Riquelme (2011) "Automatic elimination of vibrations for a centrifuge," *Mechanism and Machine Theory*, **46**(3), pp. 344–357.

[45] Subramaniam, B. and K. Ulrich (1998) "Producibility analysis using metrics based on physical process models," *Research in Engineering Design*, **10**(4), pp. 210–25.

[46] (2014) *Aluminum Extrusion Manual*, 4th ed., Aluminum Extruders Council, Wauconda, Illinois.

[47] Blanco-Ortega, A., G. Silva-navarro, J. Colín-ocampo, M. Oliver-salazar, and G. Vela-valdés (2012) "Automatic Balancing of Rotor-Bearing Systems," in *Advances on Analysis and Control of Vibrations - Theory and Applications*, chap. 10, InTech, pp. 213–230.

[48] Han, Y. and J. Palacios (2012) "Analytical and Experimental Determination of Airfoil Performance Degradation Due to Ice Accretion," in *4th AIAA Atmospheric and Space Environments Conference*, June, pp. 1–25.

[49] Suggs, C. W. and C. J. Abrams (1983) "Vibration isolation of power tools operators," in *27th Annual Meeting of the Human Factors Society*, pp. 606–610.

[50] Gurram, R., S. Rakheja, and A. Brammer (1995) "Driving-point mechanical impedance of the human hand-arm system: synthesis and model development," *Journal of Sound and Vibration*, **180**(3), pp. 439–458.

[51] Goodman, T. P. (1964) "A Least-Squares Method for Computing Balance Corrections," *Journal of Engineering for Industry*, **86**(3), pp. 273–277.

[52] Lund, J. W. and J. Tonnesen (1972) "Analysis and Experiments on Multi-Plane," *Journal of Engineering for Industry*, **94**(1), pp. 233–242.

[53] Lee, C. W., Y. D. Joh, and Y. D. Kim (1990) "Automatic modal balancing of flexible rotors during operation: computer controlled balancing head," *Proceedings of the Institution of Mechanical Engineers, Part C: Journal of Mechanical Engineering Science*, **204**(1), pp. 19–28.

[54] Dyer, S. W., J. Shi, J. Ni, and K.-K. Shin (2002) "Robust Optimal Influence-Coefficient Control of Multiple-Plane Active Rotor Balancing Systems," *Journal of Dynamic Systems, Measurement, and Control*, **124**(1), p. 41.

[55] Manchala, D. W., A. B. Palazzolo, A. F. Kascak, G. T. Montague, and G. V. Brown (1997) "Constrained quadratic programming, active control of rotating mass imbalance," *Journal of Sound and Vibration*, **205**(5), pp. 561–580.

[56] Gill, P. E., W. Murray, and M. A. Saunders (1984) "Procedures for Optimization Problems with a Mixture of Bounds and General Linear Constraints," *ACM Transactions on Mathematical Software*, **10**(3), pp. 282–298.

[57] Gill, P. E., N. Gould, and W. Murray (1984) "A weighted gram-schmidt method for convex quadratic programming," *Mathematical . . .*, **30**(2), pp. 176–195.

[58] Blanco-Ortega, A., F. Beltran-Carbajal, and G. Silva-Navarro (2007) "On-Line Algebraic Identification of Eccentricity in Active Vibration Control of Rotor-Bearing Systems," in *International Conference on Electrical and Electronics Engineering*, 4, Mexico City, Mexico, pp. 253–256.

[59] Fliess, M. and H. Sira-Ramierz (2003) "An algebraic framework for linear identification," *ESAIM Control, Optimisation and Calculus of Variations*, **9**(2003), pp. 151–168.

[60] Beltran-Carbajal, F., G. Silva-Navarro, H. Sira-Ramierz, and J. Quezada-Andrade (2005) "Active Vibration Control Using On-line Algebraic Identification of Harmonic Vibrations Identification of Harmonic Vi- brations," in *American Control Conference*, pp. 4820–4825.

[61] Beltran-Carbajal, F., G. Silva-Navarro, H. Sira-Ramierz, and A. Blanco-Ortega (2010) "Active Vibration Control Using On-line Algebraic Identification and Sliding Modes," *Computación y Sistemas*, **13**(3), pp. 313–330.

[62] Knospe, C. R., R. Hope, S. J. Fedigan, and R. D. Williams (1995) "Experiments in the control of unbalance response using magnetic bearings," *Mechatronics*, **5**(4), pp. 385–400.

[63] DeSmidt, H. A., K. W. Wang, and E. Smith (2004) "Multi-Harmonic Adaptive Vibration Control of Magnetic Bearing-Driveline with Auxiliary Feedback: Theory and Experiment," in *45th AIAA/ASME/ASCE/AHS/ASC Structures, Structural Dynamics & Materials Conference*, Structures, Structural Dynamics, and Materials and Co-located Conferences, American Institute of Aeronautics and Astronautics.

[64] DeSmidt, H. A. (2005) *Robust-Adaptive Active Vibration Control of Alloy and Flexible Matrix Composite Rotorcraft Drivelines via Magnetic Bearings: Theory and Experiment*, Ph.D. thesis, The Pennsylvania State University.

[65] Deckler, D. C., R. J. Veillette, M. J. Braun, and F. K. Choy (2004) "Simulation and Control of an Active Tilting-Pad Journal Bearing," *Tribology Transactions*, **47**(3), pp. 440–458.

[66] Lee, C. W. (2006) "Mechatronics in Rotating Machinery," in *7th IFToMM-Conference on Rotor Dynamics*, September, Vienna, Austria, pp. 25–28.

[67] El-Shafei, A. (1991), "Hybrid squeeze film damper for active control of rotors," .

[68] ——— (2002) "Active Control Algorithms for the Control of Rotor Vibrations Using Hybrid Squeeze Film Dampers," *Journal of Engineering for Gas Turbines and Power*, **124**(3), pp. 598–607.

[69] Burrows, C. R., M. N. Sahinkaya, and O. S. Turkay (1984) "An Adaptive Squeeze-Film Bearing," *Journal of Tribology*, **106**(1), pp. 145–151.

[70] Hathout, J. P. and A. El-Shafei (1997) "PI Control of HSFDs for Active Control of Rotor-Bearing Systems," *J. Eng. Gas Turbines Power*, **119**(July 1997), pp. 658–667.

[71] Chang-Jian, C. W., H. T. Yau, and J. L. Chen (2010) "Nonlinear dynamic analysis of a hybrid squeeze-film damper-mounted rigid rotor lubricated with couple stress fluid and active control," *Applied Mathematical Modelling*, **34**(9), pp. 2493–2507.

[72] Sun, L. and J. Krodkiewski (2000) "Experimental Investigation of Dynamic Properties of an Active Journal Bearing," *Journal of Sound and Vibration*, **230**(5), pp. 1103–1117.

[73] Guozhi, Y., Y. F. Fah, C. Guang, M. Guang, F. Tong, and Q. Yang (2000) "Electro-Rheological Multi-layer Squeeze Film Damper and Its Application to Vibration Control of Rotor System," *Journal of Vibration and Acoustics*, **122**(1), p. 7.

[74] Bishop, R. E. D. (1982) "On the possibility of balancing rotating flexible shafts," *Journal of Mechanical Engineering Science*, **24**(4), pp. 215–220.

[75] Hildebrand, S. and L. Miller (2010), "Rotating machine active balancer and method of dynamically balancing a rotating machine shaft with torsional vibrations," .

[76] Goodwin, M. J., J. E. T. Penny, and C. J. Hooke (1984) "Variable impedance bearings for turbogenerator rotors," in *3rd International Conference on Vibrations in Rotating Machinery*, Heslington, pp. 535–541.

[77] Blanco-Ortega, A., G. Silva-Navarro, and J. Gomez (2003) "Dynamic Stiffness Control and Acceleration Jeffcott-Like Rotor System," in *The International Congresse on Sound and Vibration*, 42231, Stockholm, Sweden, pp. 227–234.

[78] Nikolajsen, J. L., R. Holmes, and V. Gondhalekar (1979) "Investigation of an Electromagnetic Damper for Vibration Control of a Transmission Shaft," *Proceedings of the Institution of Mechanical Engineers*, **193**(31), pp. 331–336.

[79] Stammers, C. and T. Sireteanu (1998) "Vibration Control of Machines By Use of Semi-Active Dry Friction Damping," *Journal of Sound and Vibration*, **209**(4), pp. 671–684.

[80] Nikolajsen, J. L. and M. S. Hoque (1990) "An Electroviscous Damper for Rotor Applications," *Journal of Sound and Vibration*, **112**(4), pp. 440–443.

[81] Walsh, P. and J. Lamancusa (1992) "A variable stiffness vibration absorber for minimization of transient vibrations," *Journal of Sound and Vibration*, **158**(2), pp. 195–211.

[82] Yi, K., M. Wargelin, and K. Hedrick (1992) "Dynamic Tire Force Control by Semi-Active Suspensions," *Journal of Dynamic Systems, Measurement, and Control*, **44**, pp. 299–310.

[83] Redfield, R. C. (1990) "Low-bandwidth Semi-active Damping for Suspension Control," in *American Control Conference*, IEEE, San Diego, California, pp. 1357–1362.

[84] Kawashima, K. and S. Unjoh (1994) "Seismic response control of bridges by variable dampers," *Journal of Structural Engineering*, **120**(9), pp. 2583–2601.

[85] Symans, M. and M. Constantinou (1995) *Development and Experimental Study of Semi-Active Fluid Damping Devices for Seismic Protection of Structures*, *Tech. rep.*, National Center for Earthwuake Engineering Research.

[86] Symans, M. D. and M. C. Constantinou (1997) "Seismic testing of a building structure with a semi-active fluid damper control system," *Earthquake Engineering & Structural Dynamics*, **26**(January), pp. 759–777.

[87] Yang, J. N., J. C. Wu, and Z. Li (1996) "Control of seismic-excited buildings using active variable stiffness systems," *Engineering Structures*, **18**(8), pp. 589–596.

[88] Gavin, H. P. and N. S. Doke (1999) "Resonance suppression through variable stiffness and damping mechanisms," *Proc. SPIE 3671*, **3671**(March).

[89] Yang, G., B. F. Spencer, J. D. Carlson, and M. K. Sain (2002) "Large-scale MR fluid dampers: Modeling and dynamic performance considerations," *Engineering Structures*, **24**(3), pp. 309–323.

[90] Anusonti-Inthra, P. (2002) *Semi-Active Control of Helicopter Vibration Using Controllable Stiffness and Damping Devices*, Ph.D. thesis, The Pennsylvania State University.

[91] Torvik, P. J. (1980) *The analysis and design of contrained layer damping*, *Tech. rep.*, Air Force Intitute of Technology, Ohio.

[92] Grandhi, R. V. (1990) "Optimum Design of Space Structures with Active and Passive Damping," *Engineering with Computers*, **6**, pp. 177–183.

[93] Ader, C., J. Joseph, and D. Mangra (1995) "The application of viscoelastic damping materials to control the vibration of magnets in a synchrotron radiation facility," in *Joint American Society of Mechanical Engineers (ASME)/Japan Society of Mechanical Engineers (JSME) pressure vessels and piping conference*, Honolulu, HI.

[94] Park, S. W. (2001) "Analytical modeling of viscoelastic dampers for structural and vibration control," *International Journal of Solids and Structures*, **38**(44-45), pp. 8065–8092.

[95] Symans, M. D. and M. C. Constantinou (1998) "Passive Fluid Viscous Damping Systems for Seismic Energy Dissipation," *ISET Journal of Earthquake Technology*, **35**(4), pp. 185–206.

[96] Weinberger, M. (1977) "Drag Force of an Eddy Current Damper," *IEEE Transactions on Aerospace and Electronic Systems*, **AES-13**(2), pp. 197–200.

[97] Nagaya, K. and H. Kojima (1984) "On a Magnetic Damper Consisting of a Circular Magnetic Flux and a Conductor of Arbitrary Shape. Part I: Derivation of the Damping Coefficients," *Journal of Dynamic Systems, Measurement, and Control*, **106**(1), pp. 46–51.

[98] Kligerman, Y. and O. Gottlieb (1998) "Dynamics of a Rotating System With a Nonlinear Eddy-Current Damper," *Journal of Vibration and Acoustics*, **120**(October 1998), pp. 848–853.

[99] Teshima, H., M. Tanaka, K. Miyamoto, K. Nohguchi, and K. Hinata (1997) "Effect of eddy current dampers on the vibrational properties in superconducting levitation using melt-processed YBaCuO bulk superconductors," *Physica C*, **274**, pp. 17–23.

[100] Wiederick, H. D. (1987) "Magnetic braking: Simple theory and experiment," *American Journal of Physics*, **55**(6), pp. 500–503.

[101] Heald, M. a. (1988) "Magnetic braking: Improved theory," *American Journal of Physics*, **56**(6), pp. 521–522.

[102] Cadwell, L. H. (1996) "Magnetic damping: Analysis of an eddy current brake using an airtrack," *American Journal of Physics*, **64**(7), p. 917.

[103] Lee, K. and K. Park (1999) "Optimal robust control of a contactless brake system using an eddy current," *Mechatronics*, **9**(6), pp. 615–631.

[104] Sodano, H. a., J. Bai, D. J. Inman, and W. Keith Belvin (2005) "Concept and model of eddy current damper for vibration suppression of a beam," *Journal of Sound and Vibration*, **288**, pp. 1177–1196.

[105] Hagood, N. and A. von Flotow (1991) "Damping of structural vibrations with piezoelectric materials and passive electrical networks," *Journal of Sound and Vibration*, **146**(2), pp. 243–268.

[106] Law, H. H., P. L. Rossiter, G. P. Simon, and L. L. Koss (1996) "Characterization of Mechanical Vibration Damping By Piezoelectric Materials," *Journal of Sound and Vibration*, **197**(4), pp. 489–513.

[107] Kitagawa, Y., H. Tamai, and M. Takeshita (2004) "Characteristics of piezoelectric dampers and their application to tall buildings as a smart structural system," in *13th World Conference on Earthquake Engineering*, Vancouver, B.C.

[108] Neubauer, M., S. M. Schwarzendahl, and X. Han (2012) "Shunted piezoceramics for vibration damping: modeling, applications and new trends," in *Smart Actuation and Sensing Systems - Recent Advances and Future Challenges* (G. Berselli, R. Vertechy, and G. Vassura, eds.), chap. 27, InTech, pp. 695–716.

[109] Louroza, M. a., N. Roitman, and C. Magluta (2005) "Vibration reduction using passive absorption system with Coulomb damping," *Mechanical Systems and Signal Processing*, **19**(3), pp. 537–549.

[110] Sun, J. Q., M. R. Jolly, and M. a. Norris (1995) "Passive, Adaptive and Active Tuned Vibration Absorbers - A Survey," *Journal of Vibration and Acoustics*, **117**(B), p. 234.

[111] Hamouda, M.-N. H. (1982) *Helicopter Vibration Suppression Using Simple Pendulum Absorbers on the Rotor Blade*, Ph.D. thesis, Georgia Institute of Technology.

[112] Özgüven, H. and B. Çandir (1986) "Suppressing the first and second resonances of beams by dynamic vibration absorbers," *Journal of Sound and Vibration*, **111**(3), pp. 377–390.

[113] Jolly, M. R. and J. Q. Sun (1994) "Passive Tuned Vibration Absorbers for Sound Radiation Attenuation from Panels," *Smart Structures and Materials: Passive Damping*, **2193**(2), pp. 194–201.

[114] Kundra, T. K. (2000) "Structural dynamic modifications via models," *Sadhana*, **25**(June), pp. 261–276.

[115] Jeffcott, H. H. (1919) "The lateral vibration of loaded shafts in the neighbourhood of a whirling speed. - The effect of want of balance," *Philosophical Magazine Series 6*, **37**(219), p. 304.

[116] Bishop, R. E. D. and G. M. L. Gladwell (1959) "The vibration and balancing of an unbalanced flexible rotor," *Journal of Mechanical Engineering Science*, **1**(1), pp. 66–77.

[117] Gladwell, G. M. L. and R. E. D. Bishop (1959) "The vibration of rotating shafts supported in flexible bearings," *Journal of Mechanical Engineering Science*, **1**(3), pp. 195–206.

[118] Bishop, R. E. D. and A. G. Parkinson (1963) "On the isolation of modes in the balancing of flexible shafts," in *Institution of Mechanical Engineers*, vol. 177, pp. 407–423.

[119] Parkinson, A. G., K. L. Jackson, and R. E. D. Bishop (1963) "Some experiments on the balancing of small flexible rotors: part II - experiments," *Journal of Mechanical Engineering Science*, **5**(2), pp. 114–130.

[120] ——— (1963) "Some experiments on the balancing of small flexible rotors: part I - theory," *ournal of Mechanical Engineering Science*, **5**(1), pp. 114–130.

[121] Nicholas, J. C., E. J. Gunter, and P. E. Allaire (1976) "Effect of Residual Shaft Bow on Unbalance Response and Balancing of a Single Mass Flexible Rotor," *Journal of Engineering for Power*, **98**(2), pp. 171–189.

[122] Matsukura, Y., M. Kiso, T. Inoue, and M. Tomisawa (1979) "On the balancing convergence of flexible rotors, with special reference to asymmetric rotors," *Journal of Sound and Vibration*, **63**(3), pp. 419–428.

[123] Darlow, M. S. (1987) "Balancing Theory, of High-Speed and Machinery : Results Methods Experimental," *Mechanical Systems and Signal Processing*, **1**(1), pp. 105–134.

[124] Tan, S.-G. and X.-X. Wang (1993) "A theoretical introduction to low speed balancing of flexibile rotors: unification and development of the modal balancing and influence coefficient techniques," *Journal of Sound and Vibration*, **168**(3), pp. 385–394.

[125] Qu, L., X. Liu, G. Peyronne, and Y. Chen (1989) "The holospectrum: A new method for rotor surveillance and diagnosis," *Mechanical Systems and Signal Processing*, **3**(3), pp. 255–267.

[126] Xu, B., L. Qu, and R. Sun (2000) "The Optimization Technique-Based Balancing of Flexible Rotors Without Test Runs," *Journal of Sound and Vibration*, **238**(5), pp. 877–892.

[127] Liu, S. (2007) "A modified low-speed balancing method for flexible rotors based on holospectrum," *Mechanical Systems and Signal Processing*, **21**(1), pp. 348–364.

[128] Liu, S. and L. Qu (2008) "A new field balancing method of rotor systems based on holospectrum and genetic algorithm," *Applied Soft Computing*, **8**(1), pp. 446–455.

[129] Han, D.-J. (2007) "Generalized modal balancing for non-isotropic rotor systems," *Mechanical Systems and Signal Processing*, **21**(5), pp. 2137–2160.

[130] Kang, Y., T.-W. Lin, Y.-J. Chang, Y.-P. Chang, and C.-C. Wang (2008) "Optimal balancing of flexible rotors by minimizing the condition number of influence coefficients," *Mechanism and Machine Theory*, **43**(7), pp. 891–908.

[131] Pennacchi, P., S. Chatterton, and R. Ricci (2010) "Rotor balancing using high breakdown-point and bounded-influence estimators," *Mechanical Systems and Signal Processing*, **24**(3), pp. 860–872.

[132] Sève, F., M. Andrianoely, A. Berlioz, R. Dufour, and M. Charreyron (2003) "Balancing of Machinery with a Flexible Variable-Speed Rotor," *Journal of Sound and Vibration*, **264**(2), pp. 287–302.

[133] Danai, K. (2004) *Method for Knowledge-Based Helicopter Track and Balance*, *Tech. rep.*, University of Massachusetts.

[134] Renzi, M. J. (2004) *An assessment of modern methods for rotor track and balance*, M.s., Air Force Institute of Technology.

[135] Bechhoefer, E., A. Fang, and E. Garcia (2013) "Rotor Track and Balance Improvements," in *Annual Conference of Prognostics and Health Management Society*, pp. 1–9.

[136] Leblanc, M. (1916), "Automatic balancer for rotating bodies," .

[137] Thearle, E. L. (1932), "Dynamic balancing machine," .

[138] ——— (1950) "Automatic dynamic balancers (part 1—Leblanc balancer)," *Machine Design*, **22**, pp. 119–124.

[139] ——— (1950) "Automatic dynamic balancers (part 2—ring pendulum ball balancers)," *Machine Design*, **22**, pp. 102–106.

[140] Kubo, S., Y. Jinnouchi, Y. Araki, and J. Inoue (1986) "Automatic Balancer (Pendulum Balancer)," *The Japan Society of Mechanical Engineers*, **29**(249), pp. 924–928.

[141] Inoue, J., Y. Araki, and S. Miyaura (1967) "On the Self-Synchronization of Mechanical Vibrators," *Bulletin ofthe Japan Society of Mechanical Engineers*, **10**(41), pp. 755–762.

[142] Chung, J. and D. S. Ro (1999) "Dynamic Analysis of an Automatic Dynamic Balancer For Rotating Mechanisms," *Journal of Sound and Vibration*, **228**(5), pp. 1035–1056.

[143] Rajalingham, C., R. Bhat, and S. Rakheja (1998) "Automatic balancing of flexible vertical rotors using a guided ball," *International Journal of Mechanical Sciences*, **40**(9), pp. 825–834.

[144] Kang, J.-R., C.-P. Chao, C.-L. Huang, and C.-K. Sung (2001) "The Dynamics of a Ball-Type Balancer System Equipped with a Pair of Free-Moving Balancing Masses," *Journal of Vibration and Acoustics*, **123**(4), p. 456.

[145] Huang, W.-Y., C.-P. Chao, J.-R. Kang, and C.-K. Sung (2002) "The Application of Ball-Type Balancers for Radial Vibration Reduction of High-Speed Optic Disk Drives," *Journal of Sound and Vibration*, **250**(3), pp. 415–430.

[146] Lu, C.-J. (2006) "Stability Analysis of a Single-Ball Automatic Balancer," *Journal of Vibration and Acoustics*, **128**(1), p. 122.

[147] Lu, C.-J., M.-C. Wang, and S.-H. Huang (2009) "Analytical Study of the Stability of a Two-ball Automatic Balancer," *Mechanical Systems and Signal Processing*, **23**(3), pp. 884–896.

[148] Green, K., A. R. Champneys, and N. J. Lieven (2006) "Bifurcation Analysis of an Automatic Dynamic Balancing Mechanism for Eccentric Rotors," *Journal of Sound and Vibration*, **291**(3-5), pp. 861–881.

[149] Green, K., A. R. Champneys, and M. I. Friswell (2006) "Analysis of the Transient Response of an Automatic Dynamic Balancer for Eccentric Rotors," *International Journal of Mechanical Sciences*, **48**(3), pp. 274–293.

[150] Sohn, J.-s., J. W. Lee, E.-h. Cho, N.-C. Park, and Y.-p. Park (2007) "Dynamic Analysis of a Pendulum Dynamic Automatic Balancer," *Shock and Vibration*, **14**(2), pp. 151–167.

[151] Urbiola-Soto, L. and M. Lopez-Parra (2011) "Stability of Flexible Rotors With a LeBlanc Balancer," in *ASME Turbo Expo*, ASME, Vancouver, B.C., pp. 1–8.

[152] Bövik, P. and C. Högfors (1986) "Autobalancing of Rotors," *Journal of Sound and Vibration*, **111**(3), pp. 429–440.

[153] Chung, J. and I. Jang (2003) "Dynamic Response and Stability Analysis of an Automatic Ball Balancer for a Flexible Rotor," *Journal of Sound and Vibration*, **259**, pp. 31–43.

[154] Ehyaei, J. and M. M. Moghaddam (2009) "Dynamic Response and Stability Analysis of an Unbalanced Flexible Rotating Shaft Equipped With N Automatic Ball-Balancers," *Journal of Sound and Vibration*, **321**, pp. 554–571.

[155] Majewski, T., D. Szwedowicz, and M. a. M. Melo (2015) "Self-balancing system of the disk on an elastic shaft," *Journal of Sound and Vibration*, **359**, pp. 2–20.

[156] Lu, C.-J. and C.-H. Hung (2008) "Stability Analysis of a Three-Ball Automatic Balancer," *Journal of Vibration and Acoustics*, **130**(5), p. 051008.

[157] Green, K., A. R. Champneys, M. I. Friswell, and A. M. Muñoz (2008) "Investigation of a multi-ball, automatic dynamic balancing mechanism for eccentric rotors." *Philosophical transactions. Series A, Mathematical, physical, and engineering sciences*, **366**(1866), pp. 705–728.

[158] Tadeusz, M. (1988) "Position Error Occurrence in Self Balancers Used on Rigid Rotors of Rotating Machinery," *Mech. Mach. Theory*, **23**(1), pp. 71–78.

[159] DeSmidt, H. A. (2010) "Automatic Balancing of Bladed-Disk/Shaft System via Passive Autobalancer Devices," *AIAA Journal*, **48**(2), pp. 372–386.

[160] Caughey, T. K. (1960) "Hula-Hoop: An Example of Heteroparametric Excitation," *American Journal of Physics*, **28**(1960), p. 104.

[161] Yang, Q., E.-H. Ong, J. Sun, G. Guo, and S.-P. Lim (2005) "Study on the Influence of Friction in an Automatic Ball Balancing System," *Journal of Sound and Vibration*, **285**(1-2), pp. 73–99.

[162] Van de Wouw, N., M. N. Van den Heavel, H. Nijmeijer, and J. A. Van Rooij (2005) "Performance of an Automatic Ball Balancer With Dry Friction," *International Journal of Bifurcation and Chaos*, **15**(1), pp. 65–82.

[163] Ishida, Y., T. Matsuura, and X. Long Zhang (2012) "Efficiency Improvement of an Automatic Ball Balancer," *Journal of Vibration and Acoustics*, **134**(2), p. 021012.

[164] Ishida, Y. (2012) "Recent Development of the Passive Vibration Control Method," *Mechanical Systems and Signal Processing*, **29**, pp. 2–18.

[165] Jinnouchi, Y., Y. Araki, J. Inoue, Y. Ohtsuka, and C. Tan (1993) "Automatic balancer (static balancing and transient response of a multiball balancer)," *Trans. JSME*, **59**(557C), pp. 79–84.

[166] Urbiola-Soto, L. and M. Lopez-Parra (2011) "Dynamic Performance of the LeBlanc Balancer for Automatic Washing Machines," *Journal of Vibration and Acoustics*, **133**(4), p. 041014.

[167] Conrad, D. C. (1994) *The fundamentals of automatic washing machine design based upon dynamic constraints*, Ph.d., Purdue University.

[168] Rajalingham, C. and S. Rakheja (1998) "Whirl Suppression in Hand-Held Power Tool Rotors Using Guided Rolling Balancers," *Journal of Sound and Vibration*, **217**, pp. 453–466.

[169] Haidar, A. M. and J. Palacios (2014) "Passive Rotor Blade Balancing System for Unsymmetrical Ice Accretion," in *AIAA Region I Student Conference*, American Institue of Aeronautics and Astronautics.

[170] Hibbeler, R. C. (2010) *Engineering Mechanics: Statics and Dynamics*, 12th ed., Pearson Prentic Hall, Upper Saddle River, NJ.